INFRARED PROPERTIES OF DIELECTRIC THIN FILMS AND NEAR-FIELD RADIATION FOR ENERGY CONVERSION

A Dissertation
Presented to
The Academic Faculty

by

Trevor J. Bright

In Partial Fulfillment
of the Requirements for the Degree
Doctor of Philosophy in the
George W. Woodruff School of Mechanical Engineering

Georgia Institute of Technology
December 2013

COPYRIGHT 2013 BY TREVOR JAMES BRIGHT

INFRARED PROPERTIES OF DIELECTRIC THIN FILMS AND NEAR-FIELD RADIATION FOR ENERGY CONVERSION

Approved by:

Dr. Zhuomin Zhang, Advisor
George W. Woodruff School of
Mechanical Engineering
Georgia Institute of Technology

Dr. Yogendra Joshi
George W. Woodruff School of
Mechanical Engineering
Georgia Institute of Technology

Dr. Peter J. Hesketh
George W. Woodruff School of
Mechanical Engineering
Georgia Institute of Technology

Dr. David S. Citrin
School of Electrical and
Computer Engineering
Georgia Institute of Technology

Dr. Christopher Muratore
Department of Chemical and
Materials Engineering
University of Dayton

Date Approved: 11/13/2013

Dedicated to the memory of my high school math teacher and friend, Rex Allen Demers

ACKNOWLEDGEMENTS

I would like to express my gratitude to Dr. Zhuomin Zhang for his guidance over the past five years, without whom this work would have never become reality. I would like to especially thank him for the enlightening conversations, and the valuable tutorial he has given me. He has always been an encouraging figure in my life. I would also like to thank my Committee members: Dr. Yogendra Joshi, Dr. Peter Hesketh, Dr. David Citrin, and Dr. Christopher Muratore for their valuable feedback and advice.

I would like to thank Dr. Christopher Muratore of the University of Dayton and Dr. Andrey Voevodin of the Air Force Research Laboratory, for their valuable input on crystallography, for the fabrication of the thin film samples, and for their collaboration over the years. I am grateful to Dr. Tanner's group at the University of Florida for performing far-infrared FTIR measurements of the film samples, and especially for their valuable collaboration on the Ta_2O_5 property measurement. Also, I appreciate the valuable feedback Dr. Liping Wang of Arizona State University, who has given me on the near-field heat transfer simulations and his collaboration on near-field TPVs. I would also like to thank the DOE and AFRL for partially supporting the work in this dissertation.

In addition, I would like to show my deepest appreciation to the Nanoscale Radiation Heat Transfer Group for their help and encouragement. In particular, I would like to thank Xianglei Liu for his help with the anisotropic near-field calculation and for his collaboration on EMT, and Jesse Watjen for his help on optical constant extraction and material characterization, as well as all the other past and present group members for your friendship and support.

Finally, I would like to thank my parents, who have been there since the beginning, for their love, support, and patience. I am truly blessed to be your son.

TABLE OF CONTENTS

ACKNOWLEDGEMENTS IV

LIST OF TABLES VII

LIST OF FIGURES VIII

LIST OF SYMBOLS XIV

LIST OF ABBREVIATIONS XVIII

SUMMARY XIX

CHAPTER

1. INTRODUCTION 1

    1.1 Optical Constants of Dielectric Films in the Infrared 2

    1.2 Near-field Thermophotovoltaics 5

    1.3 Metallodielectric Photonic Crystals 7

    1.4 Outline 9

2. THEORETICAL BACKGROUND 10

    2.1 Dielectric Function Models 10

    2.2 Radiative Properties of Thin Films 15

    2.3 Hyperbolic Metamaterials 21

    2.4 Theory of Near-Field Radiative Heat Transfer 26

3. SPECTROSCOPIC TECHNIQUES 36

4. DIELECTRIC FUNCTION OF MAGNETRON SPUTTERED HFO_2 THIN FILMS 43

    4.1 Film Characterization 43

    4.2 Optical Measurements of Thin Films 48

    4.3 Dielectric Function and Optical Constants 62

5. DIELECTRIC FUNCTION OF MAGNETRON SPUTTERED TA_2O_5 THIN FILMS 65

5.1. Film Characterization 65

5.2 Film Analysis 72

5.3 Dielectric Function and Optical Constants 75

6. ANALYSIS OF A NEAR-FIELD THERMOPHOTOVOLTAIC WITH A BACKSIDE REFLECTOR 86

6.1 Current Generation and Transport 86

6.2 Results and Discussion 91

7. ENERGY STREAMLINES IN UNIAXIAL ANISOTROPIC HYPERBOLIC METAMATERIALS 105

7.1 Green's Function for an Uniaxial Anisotropic Multilayer Structure 106

7.2 Energy Streamlines in Near-Field Uniaxial Materials 111

7.3 Validity of EMA Energy Streamlines in Far-Field Uniaxial Anisotropic Materials 128

8. CONCLUSIONS AND RECOMMENDATIONS 132

APPENDIX A: XPS DATA AND ANALYSIS 136

REFERENCES 139

LIST OF TABLES

Page

Table 4.1 Sample deposition conditions and characteristic parameters obtained from different methods. HAF04a is annealed in air after the deposition for 1 hr at 800 °C, while the rest are as-deposited. Here, *A* and *B* are parameters in the Cauchy dispersion obtained from fitting the ellipsometry measurements. The average values for *A* and *B* are 1.956±0.009 and 0.0172±0.0024 μm^2, respectively. 45

Table 4.2 Far-infrared phonon parameters obtained by fitting the Lorentz model with the far-IR absorption spectrum of HAF01 using *d*= 516 nm. The fitting parameters obtained from the Cauchy formula are $A = 1.956$ and $C = 6.73\times10^{-10}$ cm^2 (based on $B = 0.0172$ μm^2). 46

Table 5.1 Sample identification (ID) and parameters. In the sample ID, the last letter "u" indicates that it was unannealed (or as-deposited) and "a" indicates that it was annealed at 800 ºC in air for one hour. The unannealed Ta_2O_5 samples TaO-1u and TaO-2u are amorphous. The annealed four samples are nanocrystalline Ta_2O_5. The RMS roughness of the film is obtained from AFM. 66

Table 5.2 Parameters for the Lorentz oscillators. Note that the parameters that determine ε_∞ from the ellipsometric measurements are (A = 2.06, B = 0.025 μm^2 for amorphous Ta_2O_5; A = 2.10, B = 0.024 μm^2 for nanocrystalline Ta_2O_5). 78

LIST OF FIGURES

Page

Figure 2.1 Ray tracing in a thin film with multiple reflection. The total transmittance or reflectance is the sum of all of the rays after multiple reflections. 16

Figure 2.2 Schematic of coherent 1D structure made of one of more layers on top and bottom of an incoherent substrate. 17

Figure 2.3 Schematic of a multilayer structure for the transfer matrix method, waves incident from a semi-infinite layer propagate through the structure. Every layer except the last has a forward and backward wave, the amplitude in layer l is related to the forward and backward amplitude at the surface by a transfer matrix. 20

Figure 2.4 Multilayer structure consisting of alternating layers of metal and dielectric which form a metallodielectric photonic crystal. 22

Figure 2.5 The iso-frequency dispersion diagram for hyperbolic materials with: (b) $\varepsilon_{\perp} > 0$ and $\varepsilon_{\|} < 0$ the circle represents the dispersion of light incident from vacuum and the hyperbolic curve inside of the anisotropic slab note that the Poynting vector is refracted negatively and (c) $\varepsilon_{\perp} < 0$ and $\varepsilon_{\|} > 0$, in this case the pointing vector is not negatively refracted. 25

Figure 2.6 Current source imbedded in layer s of a multilayer structure and the electric field it creates in layer l are related by the Green's function. 29

Figure 2.7 Two semi-infinite media labeled 0 and 2 separated by a vacuum gap by a distance of d the components of the wavevector in vacuum are shown. The media are held at temperature T_0 and T_2 respectively. 34

Figure 3.1 Measurement setup for transmittance (T), film reflectance (R_f), and substrate reflectance (R_s) of the films using FTIR. Note that the transmittance is shown near normal but is actually measured normal to the film while reflectance is taken at near normal incidence. 36

Figure 3.2 Comparison of measured and calculated transmittances for a bare Si substrate of thickness d_{Si} = 432 μm: (a) from 500 to 10000 cm^{-1}; (b) zoomed in region from 500 to 2000 cm^{-1} showing lattice and impurity absorption. 39

Figure 3.3 Schematic of a basic ellipsometry which consists of a light source, a linear polarizer that gives the incident light a known polarization, and a rotating polarizer (analyzer) with a detector that measures the elliptical shape of the polarization of reflected light. 42

Figure 4.1 Picture of inside of deposition chamber. The sample substrate sits on a rotating stage that is heated from the backside with a tungsten filament. 44

Figure 4.2 XRD patterns for samples of different thickness with the polycrystalline monoclinic phase of HfO_2 identified. 46

Figure 4.3 AFM images of two HfO_2 films deposited on Si substrates: (a) HAF01; (b) HAF04a. 47

Figure 4.4 Measured mid-infrared radiative properties of three HfO_2 film-substrate composites: (a) transmittance, T; (b) reflectance for incidence on the HfO_2 film side, R_f ; (c) reflectance for incidence on the Si substrate side, R_s . The wavenumber scales are different between the left and right regions in order to show the spectra from 500 and 1500 cm^{-1} clearly. 50

Figure 4.5 Comparison of the measured and calculated transmittance and film-side reflectance of (a) HAF01 and (b) HAF03 samples. Experimental data has an uncertainty of 0.01 in transmittance and 0.02 in reflectance. For the single-oscillator model, the dielectric function is calculated from the four-parameter model with $\varepsilon_\infty = 3.58$, $\omega_0 = 398$ cm^{-1}, $\omega_p = 1049$ cm^{-1}, and $\gamma = 147$ cm^{-1}. The parameters for the multi-oscillator model are shown in Table 3.2, using the thicknesses determined from FTIR. 54

Figure 4.6 Spectroellipsometry data and fitting results: (a) measured SE parameters and fitting results for HAF02 film at 75° incidence angle; (b) Cauchy's formula of the refractive index determined with the best fit parameters listed in Table 4.1. The dispersion based on average A and B values is also plotted. Error bars indicate the standard deviations from the mean. 56

Figure 4.7 Comparison of the measured and calculated transmittance and film-side reflectance of (a) HAF01 and (b) HAF03 samples. Experimental data has an uncertainty of 0.01 in transmittance and 0.02 in reflectance. For the single-oscillator model, the dielectric function is calculated from the four-parameter model with $\varepsilon_\infty = 3.58$, $\omega_0 = 398$ cm^{-1}, $\omega_p = 1049$ cm^{-1}, and $\gamma = 147$ cm^{-1}. The parameters for the multi-oscillator model are shown in Table 4.2, using the thicknesses determined from FTIR. 59

Figure 4.8 MIR and FIR dielectric functions of HfO_2 calculated from both the single oscillator and multiple oscillator models: (a) real part; (b) imaginary part. 63

Figure 4.9 Optical constants of HfO_2 calculated from the multiple-oscillator model, in a broad spectral region from 20 to 26000 cm^{-1}. The wavenumber is plotted in log scale. 64

Figure 5.1 X-ray diffraction profile of an annealed Ta_2O_5, sample TaO-3a, also shown are the pdf files for δ-Ta_2O_5 and β-Ta_2O_5. Other annealed samples show nearly identical XRD profiles. Note that the as-deposited samples do not show any peaks in their XRD profiles, which are therefore not shown here. 67

Figure 5.2 AFM topographies of (a) sample TaO-2u and (b) sample TaO-3a. 68

Figure 5.3 Confocal microscope images of (a) sample TaO-2u and (b) sample TaO-3a. 70

Figure 5.4 SEM cross section images of (a) sample TaO-1u and (b) sample TaO-4a. 71

Figure 5.5 Transmittance of samples TaO-1u and TaO-2u: (a) far-IR region from 10 to 1000 cm^{-1}; (b) mid-IR region from 1000 to 10,000 cm^{-1}. 77

Figure 5.6 Transmittance of samples TaO-3a and TaO-4a: (a) far-IR region from 10 to 1000 cm^{-1}; (b) mid-IR region from 1000 to 10,000 cm^{-1}. 79

Figure 5.7 Transmittance of samples TaO-5a and TaO-6a. Note that the scale is zoomed from 500 to 1500 cm^{-1} to show features in the far-IR region more clearly. 80

Figure 5.8 Reflectance of sample TaO-3a: (a) film-side; (b) substrate-side. Note that the film-side reflectance decreases toward shorter wavelengths due to scattering, while the substrate-side reflectance is unaffected. 81

Figure 5.9 Fitted dielectric function of the amorphous Ta_2O_5, in comparison with the values from Ref. [47]: (a) Real part; (b) Imaginary part. 83

Figure 5.10 Fitted dielectric function of the annealed Ta_2O_5, in comparison with the values from Ref. [48]: (a) Real part; (b) Imaginary part. 84

Figure 6.1 TPV schematic showing the p on n configuration of the TPV cell. The cell itself is divided into *N* discrete and the minority carrier diffusion model is solved with a finite difference method. 87

Figure 6.2 The efficiency of a TPV cell with a tungsten emitter at 2000 K with and without mirror on the backside to reduce sub-bandgap radiation. The mirror increases both the ideal and actual efficiency of the TPV based on the current generation calculated from the minority diffusion equation. 92

Figure 6.3 A study of the efficiency improvement of the mirror at different tungsten emitter temperatures: (a) the absolute efficiency with and without the mirror at various temperatures and (b) the relative improvement in efficiency. 94

Figure 6.4 Contour plot showing the Poynting vector as a function of depth for various wavelengths with a 1500 K emitter and a gap spacing of 10 nm: (a) without a backside reflector and (b) with a backside reflector, showing the reduction in Poynting vector beyond the bandgap 96

Figure 6.5 Poynting vector at the TPV surface at varying wavelength. Beyond the bandgap the reduction in the Poynting vector can be seen. 97

Figure 6.6 Efficiency improvement by reducing recombination at the top surface with an emitter of at 2000K: (a) with a mirror and (b) without a mirror. If a low enough recombination velocity can be achieved the trend of efficiency toward smaller gap spacing reverses. 99

Figure 6.7 For an emitter at 2000 K and backside mirror: (a) Surface minority carrier concentration and bulk recombination rate at different S_e and (b) ratio of bulk recombination rate to surface recombination rate with the transition point between the dominant mechanism shown as the critical surface recombination velocity, $S_{e,c}$. 100

Figure 6.8 Efficiency improvement for varying thicknesses of the p-region with a 2000 K emitter: (a) with mirror and (b) without mirror. Improvement is due to reduction in bulk recombination 103

Figure 7.1 A multilayer structure which is composed of layers with a uniaxial anisotropic dielectric tensor. A source embedded in layer s located at the source location $\mathbf{r}'$ will generate an electric field in layer l at location $\mathbf{r}$. 107

Figure 7.2 Geometry for two semi-infinite uniaxial anisotropic media used to represent two multilayer structures that are semi-infinite and can be represented by and effective medium with a dielectric tensor $\overset{=}{\varepsilon}$. 110

Figure 7.3 The structure under consideration consists of two infinitely repeating multilayer stacks of alternating “metal”, either D-Si or SiC, which are not metal but exhibit negative refraction due to a free electron Drude term and a Restrahlen band, respectively. The “dielectric” layer is Ge which is approximated with a constant dielectric function. 112

Figure 7.4 (a) Real part of the EMA dielectric function of doped Si and Ge with f = 0.5 (b) and for doped SiC and Ge with f = 0.3. The inset shows a schematic of the structure of interest. 113

Figure 7.5 Power transmission coefficient between (a) two semi-infinite EMA structures of doped Si and Ge with f = 0.5 and a gap spacing of 10 nm, (b) between EMA structures of SiC and Ge with f = 0.3 and a gap spacing of 10 nm. (c) Spectral heat flux between two semi-infinite EMA structures of doped Si and Ge with f = 0.5 and a gap spacing of 10 nm, (d) two semi-infinite EMA structures of SiC and Ge with f = 0.3 and a gap spacing of 10 nm. 114

Figure 7.6 (a) Heat flux per unit frequency per unit wavevector versus the normalized wavevector at four select frequencies for D-Si/Ge multilayer f = 0.5. (b) Integration of the total heat flux over the wavevector space. The horizontal line shows where 50% of the heat flux falls above and below the median wavevector for each frequency. 116

Figure 7.7 Heat flux per unit frequency per unit wavevector versus the normalized wavevector at four select frequencies for SiC/Ge multilayer f = 0.3. (b) Integration of the total heat flux over the wavevector space. The horizontal line shows where 50% of the heat flux falls above and below the median wavevector for each frequency. 118

Figure 7.8 (a) Normalized penetration depth of D-Si/Ge multilayer f = 0.5 with a gap spacing of 10 nm at select frequencies. (b) Normalized average penetration depth of Si/Ge multilayer f = 0.5 with a gap spacing of 10 nm. 120

Figure 7.9 (a) Normalized penetration depth of SiC/Ge multilayer $f = 0.3$ with a gap spacing of 10 nm at select frequencies. (b) Normalized average penetration depth of SiC/Ge multilayer $f = 0.3$ with a gap spacing of 10 nm. 122

Figure 7.10 (a) and (b) energy streamlines for median normalized wavevector at different select frequencies in D-Si/Ge multilayer structure with f=0.5 at 10 nm gap spacing 123

Figure 7.11 (a) and (b) energy streamlines for median normalized wavevector at different select frequencies in SiC/Ge multilayer structure with $f = 0.3$ at 10 nm gap spacing. 125

Figure 7.12 Average lateral gap displacement for (a) D-Si/Ge structure with $f = 0.5$ at 10 nm gap spacing and (b) for SiC/Ge with $f = 0.3$ at 10 nm gap spacing. 127

Figure 7.13 ESLs for positive refraction at an incidence angle of 60° for the uniaxial effective medium and multilayer structures with 150 and 15 layers of the same total thickness, d in (a) Negative refraction (type I) regime, (b) Epsilon near zero regime, and (c) Positive refraction regime. 129

Figure A.1 XPS curves for and unannealed sample showing the O 1s peak. The SiO_2 peak is used to correct the Ta:O ratio. 136

Figure A.2 XPS curves for an annealed Ta_2O_5 sample showing the Ta 4f peak. Note the peak location of 25.85 is consistent with the peak location from literature (26-27 ev). 137

Figure A.3 XPS curves for Ta 4f from the unannealed samples. Note the peak location of 25.85 is consistent with the peak location from literature (26-27 ev). 138

LIST OF SYMBOLS

Variables

$\mathbf{a}$	acceleration vector
A, B	amplitudes of forward and backward wave
c	speed of light in vacuum
C_1 ,C_2	Cauchy coefficients
d	layer thickness or gap separation distance
D	minority carrier diffusion coefficient
$\mathbf{D}$	displacement current or dynamical matrix
e	charge of electron, 1.6022×10^{-19} C
$\hat{\mathbf{e}}$	anisotropic extraordinary (TM) wave unit vector
$\mathbf{E}$	electric field
f	volume filling fraction
g	photocurrent generation density
$\overline{\overline{\mathbf{g}}}$	Weyl component of electric Green's function
$\overline{\overline{\mathbf{G}}}$	electric Green's function
$\hbar$	Planck's constant divided by 2π
$\overline{\overline{\mathbf{h}}}$	Weyl component of magnetic Green's function
$\mathbf{H}$	magnetic field
J	current
$\mathbf{J}$	current vector
$\mathbf{k}$	wavevector
k	index or wavevector magnitude
k_B	Boltzmann's constant, 1.3065×10^{-12} m^2 kg s^2 K^{-1}

K	spring constant
l	index
m	mass or energy streamline slope
$\mathbf{M}$	transfer matrix
n	refractive index, carrier concentration, or number density
N	carrier concentration, number of layers, or number of oscillators
$\hat{\mathbf{o}}$	isotropic TE/ordinary (TE wave) unit vector
$\hat{\mathbf{p}}$	isotropic TM wave unit vector
$\mathbf{P}$	polarization vector or propagation matrix
q	carrier charge
Q	heat flux
r	Fresnel reflection coefficient
$\mathbf{r}$	position vector
R	bulk recombination rate or reflectance
$\mathbf{S}$	Poynting vector
S	oscillator strength or surface recombination velocity
t	Fresnel transmission coefficient, layer thickness, or time
T	transmittance
$\mathbf{v}$	velocity vector
$\mathbf{x}$	displacement vector
x,y,z	Cartesian coordinates

Greek Symbols

α	absorptivity
β	radial component of wavevector

$\overline{\overline{\mathbf{\Gamma}}}$	electric Green's function
γ	damping factor or z-component of wavevector
δ	Dirac delta function or penetration depth
δ_{nj}	Kronecker delta
Δ	ellipsometry parameter or vacuum lateral displacement
ε	dielectric function
ε'	real part of dielectric function
ε''	imaginary part of dielectric function
$\overline{\overline{\varepsilon}}$	dielectric tensor
η	efficiency
Θ	mean energy of Planck oscillator
κ	extinction coefficient
λ	wavelength
μ	magnetic permeability or carrier mobility
ν	wavenumber
ξ	power transmission coefficient
ρ	radial coordinate or reflectance
ϕ	streamline propagation angle
τ	relaxation time or transmittance
ω	angular frequency
κ	extinction coefficient
σ	electrical conductivity
Ψ	ellipsometry parameter

Subscripts/Superscripts

0	0th index or free space
A	acceptor
bi	built-in
d	dielectric
D	donor
dp	depletion
e	electrons or extraordinary wave (TM wave)
E	electric
eff	effective medium
f	film
h	holes (positive carriers)
j,k,l	index
m	metal
n	n-type
o	ordinary wave (TE wave)
p	plasma or p-type
ph	photo
r	random fluctuation
R	radiative
s	substrate
t	transverse
surf	surface
w	water
x,y,z	component direction

LIST OF ABBREVIATIONS

AFM	atomic force microscopy
DC	direct current
EMA	effective medium approximation
EMT	effective medium theory
ESL	energy streamline
FIR	far-infrared
FTIR	Fourier transform infrared spectrometry
IR	infrared
MDPC	metallodielectric photonic crystal
MIR	mid-infrared
MSE	mean squared error
NIR	near-infrared
RMS	root mean squared
SE	spectroellipsometry
SEE	standard error of estimate
SEM	scanning electron microscope
TE	transverse electric
TM	transverse magnetic
TPV	thermophotovoltaic
UV	ultraviolet
VIS	visible
XPS	x-ray photon spectroscopy
XRD	x-ray diffraction

SUMMARY

Studies of the radiative properties of thin films and near-field radiation transfer in layered structures are important for applications in energy, near-field imaging, coherent thermal emission, and aerospace thermal management. A comprehensive study is performed on the optical constants of dielectric tantalum pentoxide (Ta_2O_5) and hafnium oxide (HfO_2) thin films from visible to the far infrared using spectroscopic methods. These materials have broad applications in metallo-dielectric multilayers, anti-reflection coatings, and coherent emitters based on photonic crystal structures, especially at high temperatures since both materials have melting points above 2000 K. The dielectric functions of HfO_2 and Ta_2O_5 obtained from this work may facilitate future design of devices with these materials.

A parametric study of near-field TPV performance using a backside reflecting mirror is also performed. Currently proposed near-field TPV devices have been shown to have increased power throughput compared to their far-field counterparts, but whose conversion efficiencies are lower than desired. This is due to their low quantum efficiency caused by recombination of minority carriers and the waste of sub-bandgap radiation. The efficiency may be improved by adding a gold mirror as well as by reducing the surface recombination velocity, as demonstrated in this thesis. The analysis of the near-field TPV and proposed methods may facilitate the development or high-efficiency energy harvesting devices.

Many near-field devices may eventually utilize metallo-dielectric structures which exhibit unique properties such as negative refraction due to their hyperbolic isofrequency contour. These metamaterials are also called indefinite materials because of their ability to support propagating waves with large lateral wavevectors, which can result in enhanced near-field radiative heat transfer. The energy streamlines in such structures are

studied for the first time. Energy streamlines illustrate the flow of energy through a structure when the fields are evanescent and energy propagation is not ray like. The energy streamlines through two semi-infinite uniaxially anisotropic effective medium structures, separated by a small vacuum gap, are modeled using the Green's function. The lateral shift and penetration depth are calculated from the streamlines and shown to be relatively large compared to the vacuum gap dimension. The study of energy streamlines in hyperbolic metamaterials helps understand the near-field energy propagation on a fundamental level.

CHAPTER 1

INTRODUCTION

By 2035 the worldwide demand for energy is projected to increase to 770 quadrillion BTU, according to IEO2011 [1]. Furthermore, it is currently estimated that 55.6% of energy in the US is lost as rejected energy [2]. The majority of that energy (26.6%) is from electrical power generation. While some energy loss is unavoidable because of 2nd law limitations, waste heat may still have exergy, meaning that devices for recovering waste heat could have a large potential impact in reducing energy waste. Because of the projected increase in future energy demands, it is important to seek new devices and mechanisms to harvest waste heat that are more efficient and provide higher energy throughput. Many potential devices may operate on the concept of near-field radiation, where energy throughput can be larger than in classical devices limited by the Stefan-Boltzmann law.

In order to design devices that can be used to harvest waste energy there must be suitable materials with known properties and current device limitations must be well understand in order to devise methods to improve future performance. Near-field thermophotovoltaics (TPVs) are one device that could potentially be used to recover waste energy [3]. They rely on the enhanced radiation exchange between a heated surface (emitter) and a TPV cell (receiver) that can exceed the radiation energy exchange between two black surfaces [4]. While low throughput is a drawback of traditional TPVs, near-field effects allow the energy throughput to be increased for the same temperature difference between emitter and receiver. If the efficiency were as high as the best solar cells, around 40%, such a device may be very desirable in the future. Furthermore, higher efficiency often relies on high temperature sources and structures that exhibit special modes that enhance near-field heat transfer. Hyperbolic metamaterials with alternating

layers of dielectric and metal stacked on each other in alternating layers, like books on a desk, can exhibit hyperbolic modes that enhance near-field heat transfer, as well as guided-modes with interesting energy propagation characteristics that allow the penetration depth of radiation to become larger than expected. Suitable materials used in these hyperbolic structures and TPVs in general whether dielectric, semi-conductor, or metallic will need to be chemically stable and resistant to high temperature if there is going to be any application in waste heat recovery. The purpose of this thesis is therefore to investigate materials that may have potential use in high temperature metamaterials, understand the fundamental limitations of near-field TPVs, and investigate the properties and flow energy in multilayer metamaterials that may eventually be incorporated into near-field devices. In the following section we will introduce two potential materials that have excellent properties for high temperature energy applications.

1.1 Optical Constants of Dielectric Films in the Infrared

Hafnium oxide (HfO_2 or hafnia) and Tantalum Oxide (Ta_2O_5) are important optical coating materials with high refractive indices and broadband transparency from ultraviolet (UV) wavelengths to the mid-infrared (MIR). These materials may be useful for near-field devices and have many existing applications such as visible (VIS), near-infrared (NIR) and MIR antireflection coatings [5,6], chirped mirrors and band pass filters [7], UV mirrors with a high damage threshold [8], heat mirrors for energy-efficient windows [9], thin-film capacitors [10], microelectronics [11], anti-reflection coatings [12], multilayer optical coatings [6,13], corrosion resistant protective coatings [13], and infrared (IR) emissivity modulating devices [14]. In addition, because of their high melting temperature (~ 2800 °C for HfO_2 and 1,872 °C for Ta_2O_5) and excellent thermal stability [15], these materials hold promise as thermal barrier coatings for turbine blades operating in harsh and high-temperature environments [16,17]. The importance of

detailed knowledge of the optical constants of these materials for design purposes is thus essential.

Hafnia films have been deposited by a variety of techniques, including electron-beam deposition [9,16–19], often with ion-assisted or plasma-ion-assisted deposition [8,18,20], magnetron sputtering [7,19,21,22], high-pressure reactive sputtering [23], plasma-assisted reactive pulsed-laser deposition [24], reactive ion plating [6], chemical vapor deposition [25,26], atomic layer deposition [27–30], chemical solution deposition [30], etc. A number of studies have reported the optical properties of HfO_2 films in the UV/VIS/NIR region [5–8,19,20,23,24,27,28,31]. The refractive index of crystalline hafnia films is approximately 2.0–2.1 at λ=550 nm [7,8,18,19,24] and reduces somewhat for films with low packing density [32]. The deposition and post-annealing conditions also play an important role in the optical properties [6,23,28,33]. While good transparency of HfO_2 films has been shown in the MIR up to λ=11.5 μm [5], data is not available for the optical constants of hafnia films in the MIR region, except for the tabulated values in Ref. [34] which gives a refractive index of HfO_2 around 1.9 at wavelengths from 0.6 to 12 μm. The lattice vibration frequencies or optical active phonons for crystalline HfO_2 are in the FIR region from about 100 to 800 cm^{-1} [23,30,35,36]. The Raman spectra have been obtained for both the orthorhombic and monoclinic phases of HfO_2 single crystals [36]. Some researchers have used FIR absorptance and Raman scattering spectra to demonstrate the annealing effect on the crystallinity of hafnia films [29,30,35]. The ab initio calculations using the local density approximation and the generalized gradient method have been carried out to predict the phonon contribution to the dielectric function of HfO_2 [37,38], but without quantitative comparison with the transmission and absorption spectra. At present, a practical wideband dielectric function model does not exist for HfO_2 films or crystals. For NIR/MIR applications, it is desirable to have a simple explicit dielectric function that can be used to compute the frequency-dependent optical constants of HfO_2.

Similar to HfO_2, Ta_2O_5 dielectric films can be deposited by various methods of physical vapor deposition (PVD) or chemical vapor deposition (CVD) [11]. Different deposition methods may result in films that have an amorphous phase (a-Ta_2O_5) or two distinct crystal phases depending on the annealing, that is, an orthorhombic β-Ta_2O_5 and a hexagonal δ-Ta_2O_5 [11,39]. In addition, there is also a high-temperature tetragonal α-Ta_2O_5 phase that forms at temperatures of approximately 1360 °C [40]. The majority of literature on the optical constants has concentrated on the UV, VIS, and NIR properties. [6,41–45] The optical constants for a variety of dielectric films, deposited using electron-beam evaporation, have been determined and tabulated from 0.6 to 12 μm in Ref. [34]. It was shown that Ta_2O_5 has a refractive index around 2.0 with negligible absorption from 0.6 up to 10 μm [34]. Chandrasekharan et al. [46] reported the MIR properties of Ta_2O_5 films and studied the development of a SiO_2 layer at the interface between the film and the Si substrate due to heat treatment. Franke et al. [47,48] investigated the optical properties of amorphous and crystalline Ta_2O_5 films from the deep-UV to FIR using SE. The dielectric function was modeled based on the line-shape analysis up to a wavelength of 40 μm. However, strong phonon modes exist in Ta_2O_5 at wavenumbers between 200 and 300 cm^{-1} (or wavelengths from 50 to 33 μm) [49]. In order to fully describe the FIR dielectric function of Ta_2O_5 films, it is imperative to consider these phonon modes in the dielectric function model. The study of the FIR properties of materials may be useful in designing absorption-based filters as well as in understanding the atomic bonding structures [49].

This thesis describes an investigation of HfO_2 and Ta_2O_5 optical properties from the VIS to FIR with a focus on the NIR and MIR region, where phonon absorption is insignificant, for applications as a non-absorbing optical coating. Films were deposited on double-side polished Si substrates using DC magnetron sputtering and the films were characterized with X-ray diffractometry (XRD) and atomic force microscopy (AFM). A Fourier-transform infrared (FTIR) spectrometer measured the near-normal transmittance

and reflectance for incidence on both the film side and the substrate side from 1 to 20 μm wavelengths. The thickness and optical constants of the films are obtained by modeling with various physical models of the dielectric function in different regions of the NIR/MIR/FIR spectrum. Both of these materials are good candidates for use on the high temperature side of TPV systems because of their stability and high melting point. After introducing some candidate materials the next topic of study in the present work are the limitations of near-field TPV efficiency.

1.2 Near-field Thermophotovoltaics

Thermophotovoltaic (TPV) cells are semiconductor junctions that use infrared (IR) radiation from a thermal source (~1000-2000 K) to generate photocurrents. These devices have many desirable features such as silent operation and portability. TPV cells have been shown to achieve power densities orders of magnitude higher than commercial batteries [50]. However, traditional TPV devices suffer from low power throughput because of the limitation imposed by the blackbody limit of thermal radiation. Basu et al. [51] provided a thorough review of the applications of near-field TPV devices to energy conversion, including their advantages over current technologies [5].

The blackbody limit can be overcome by near-field radiation enhancement where photons can tunnel across a gap that is on the order of the characteristic scale of the radiation. This allows near-field TPV systems to achieve power throughputs that exceed the blackbody limit because of evanescent modes that couple between the two surfaces. This additional energy flux also gives more room for potential efficiency enhancement with filters, while still maintaining higher heat transfer rates than traditional TPV devices. Despite their advantages over traditional TPV systems, the low predicted efficiency of near-field TPV cells is something that still needs to be addressed.

The performance of near-field TPV systems has already been investigated theoretically first by Pan et al. [52], between two identical dielectric materials, and subsequently assuming 100% quantum efficiency by Laroche et al. [3]. Narayanaswamy and Chen [53] studied enhancing near-field TPV performance with the presence of surface modes. Whale and Cravalho [54] modeled the performance of a cell constructed of the ternary alloy of InGaAs and considering the recombination losses by assuming a uniform photon flux with an effective active area determined by the carrier lifetimes, Park et al. [55] modeled the minority carrier diffusion to account for the recombination effect. Francouer et al. [56] expanded this to include the effect of temperature on the efficiency and determined the amount of cooling needed to maintain near-field TPV performance. In addition, there have been several experiments measuring heat flux and current generation; Ottens et al.[57] measure the heat transfer coefficient between two sapphire plates near room temperature separated by a 2-100 μm gap, Hu et al. [4] showed measured heat fluxes exceeded the blackbody limit using two glass plates separated by spherical polystyrene spacers with 1 μm diameter between two plates, Hanamura, et al. [58] demonstrated an increase in the current density as the separation gap spacing between an tungsten emitter and Si-TPV cell was decreased using a piezoactuator, and DiMatteo et al. [59] demonstrated an increase in the short circuit current generation at submicron spacings using a InAs TPV cell with micron sized spacers, and a piezo actuator to alter the gap spacing periodically.

Initial studies of the performance of near-field TPV systems either overlooked limitations in quantum efficiency [3] or, when considering recombination, reported efficiency values as a function of gap spacing that are around 20% or lower at smaller gap spacings [55,56,60]. A realistic performance limit for the efficiency of near-field TPV devices may be around 40% based on the current state of the art for solar cells [61], which would be a significant improvement over current estimates for near-field TPV devices. The values reported in previous studies do not consider any modern techniques

for optimizing cell efficiencies such as heterojunctions, windows, back-side reflectors, filters, etc. This study will use the fluctuation dissipation theorem to determine the spatial photocurrent generation inside of a near-field TPV cell and model the current generation and efficiency of the cell using the minority carrier diffusion equations. This will expand previous studies by showing the effect of reducing unusable radiation using a Au mirror on the backside of the cell and show a reversal in some of the trends observed in the efficiency for an imperfect cell with changing gap spacing, if the surface can be prepared to a suitable level so as to reduce surface recombination. Furthermore, the efficiency as a function of gap spacing will be shown to be much closer to the 100% quantum efficiency than previously shown after the structure is optimized, which may be accomplished using techniques that are similar to those applied to modern high efficiency solar cells. Finally, having looked at the limitations of current devices we move on to the study of energy flow in metallodielectric structures that may improve device performance even further.

1.3 Metallodielectric Photonic Crystals

Another interesting near-field structure is the hyperbolic meta-materials, which may consist of multilayers of metallic and dielectric material or nano-rods with metallic properties [62–64]. These structures can often be treated as an effective medium which has anisotropic properties [62,65,66]. Furthermore, hyperbolic materials, which due to their anisotropic properties deviate from the usual elliptical dispersion, have the potential to image or guide evanescent waves [67,68] and offer unique possibilities for applications in near-field devices. This unique dispersion results in hyperbolic modes, which can enhance the heat transfer rate beyond the blackbody limit. In addition to the hyperbolic modes, if the metal filling fraction is large hyperbolic materials may also exhibit surface modes as well.

The energy exchange in the near-field between two semi-infinite isotropic and anisotropic media has been investigated [69–72]. The concept of energy streamlines,

which had previously been used in acoustics [73], was introduced to near-field radiation to show the direction of propagation of evanescent waves [74,75], which cannot be determined simply by ray optics. The energy streamlines trace the net direction of heat flux inside of the structure, and since there can be a large lateral shift in the energy streamlines associated with the large transverse component of wavevectors that are able tunnel through the vacuum gap, the energy streamlines through bulk isotropic media was studied in order to characterize the typical dimension of this lateral shift [74,76]. Furthermore, there is extra enhancement associated with surface modes, which can have an extremely large transverse component of the wavevector. This mechanism of energy transfer enhancement was studied in Ref. [53] and can result in large lateral shifts of energy.

In an investigation of energy transfer in the near-field the typically the parameters of interest are the total heat flux, penetration depth, and lateral displacement, as calculated from the energy streamlines. The heat flux has been studied for uniaxial anisotropic media and a simple expression for the heat flux across the vacuum gap has been introduced [69–72]. However, previous studies on lateral displacement focused on isotropic bulk or multilayer media, but did not consider bulk anisotropic media. Therefore, the lateral displacement and streamlines in such structures has not been investigated and the Green's function method must be applied to determine both the perpendicular and lateral components of the Poynting vector inside of the uniaxial anisotropic media and vacuum gap.

This work will investigate the pertinent characteristic dimensions of such structures with a gap spacing between two metallodielectric photonic crystals of 10 nm, by solving for the energy streamlines using the Green's function method. The characteristic dimensions are based on the overall lateral displacement of energy and the penetration depth of energy into the medium which are calculated at characteristic frequencies within the materials hyperbolic modes and elsewhere. A structure must have

dimensions which are much larger than the characteristic lateral displacement in order to remain one dimensional. If the lateral dimensions are too small near-field heat transfer may be limited because the presence of larger lateral wavevectors may be limited or altered by the dimensions of the structure.

1.4 Outline

This thesis is divided into 8 chapters. Chapter 2 is an introduction to the theory of dielectric function models and the equations that model the transmittance and reflectance of thin films and multilayer structures. This chapter also covers the fundamentals of near-field radiation between two bulk materials and multilayer structures. Chapter 3 covers the apparatus used to fabricate and measure the optical constants of the HfO_2 and Ta_2O_5 thin films. chapters 4 and 5 present the characterization of the films of HfO_2 and Ta_2O_5 respectively. Chapter 6 looks is a parametric study of limiting factors in near-field TPV performance. Chapter 7 is a study of the energy propagation through multilayer metallodielectric photonic crystals. Finally, chapter 8 presents the overall conclusion of this work and potential for future continuation of this work.

CHAPTER 2

THEORETICAL BACKGROUND

This Chapter covers the basic models for the dielectric function used in the IR region, the equations for modeling transmission and reflection of film structures, provides and introduction to hyperbolic materials, and covers the fundamentals of isotropic near-field radiation in 1D structures. In section 2.1, the dielectric function models of free electrons and phonons, as well as the dielectric function due to bandgap transitions at sub-bandgap frequencies, where the bandgap absorption has become negligibly small, are discussed. In section 2.2 the radiative properties of 1D structures, such as the transmittance and reflectance formula for free standing thin films and thin films on thick substrates are presented, as well as the transfer matrix method for multilayer structures are introduced. Following in section 2.3 is a presentation of hyperbolic materials and the effective medium approximation of dielectric constants, which treats a non-homogenous material as a homogenous media. Finally, in section 2.4 the chapter is concluded with a presentation of the theory of near-field radiation, the Green's function, and equations for multilayer and semi-infinite structures in the near-field.

2.1 Dielectric Function Models

2.1.1 The Dielectric Constant

For a homogenous, isotropic material the relationship between the electric field and the displacement current is given by [77]

$$\mathbf{D} = \varepsilon \mathbf{E} \tag{2.1}$$

where the factor ε is the dielectric function, which is a property of the material that depends on the frequency of the exciting electric field, where the electric field is of the form

$$\mathbf{E} = \mathbf{E}_0 e^{-i(\omega t - \mathbf{k}\cdot\mathbf{r})} \tag{2.2}$$

In general the dielectric function will be a complex number. For non-magnetic materials the dielectric function is related to the refractive index of the material, *n*, and the extinction coefficient, κ, with following equation.

$$\varepsilon = (n + i\kappa)^2 \tag{2.3}$$

The frequency dependence of the dielectric function is often modeled phenomenologically, by treating the interaction of vibrating atoms with the electric field as a mass spring damper system, or for free electrons as a damped system driven by the oscillating electrical field.

2.1.2 The Lorentz Model of Atomic Vibrations

When the driving electric field is time harmonic as in Eq. (2.2) the equations of motion of an atom modeled as a mass spring damper system can be written for a single oscillator mode *j* as

$$m_j\mathbf{a} + m_j\gamma_j\mathbf{v} + K_j\mathbf{x} = e\mathbf{E} \tag{2.4}$$

where m_j is the mass, $\mathbf{a}$ is the acceleration vector, γ_j is the damping factor, K_j is the spring constant $\mathbf{v}$ is the velocity vector, *e* is charge of the oscillator, and $\mathbf{x}$ is the displacement from the equilibrium position. Assuming a time harmonic solution, the displacement of the particle can be found by solving the force balance equation to give

$$\mathbf{x} = \frac{e/m_j}{\omega_j^2 - i\gamma_j\omega - \omega^2}\mathbf{E} \tag{2.5}$$

where ω_j is the resonance frequency of the jth mode. The resonance of the spring is related to the spring constant and mass by $\omega_j = \sqrt{K_j / m_j}$. The dipole moment per unit volume (polarization) depends on the number density, n_j, of the oscillator mode and is given as

$$\mathbf{P} = n_j e \mathbf{x} \tag{2.6}$$

Using the constitutive relations between the electric field and the materials polarization one can derive the Lorentz model for a single oscillator

$$\varepsilon(\omega) = \varepsilon_\infty + \frac{\omega_{\mathrm{p}j}^2}{\omega_j^2 - i\gamma\omega - \omega^2} \tag{2.7}$$

$\omega_{\mathrm{p}j}$ is called the plasma frequency because of the similarity in form the variable has in the Lorentz model to the plasma frequency of the Drude model, to be discussed next. It is not related to a plasma phenomenon, but rather has to do with the strength of the oscillator mode. In terms of the parameters of our mass spring damper model the plasma frequency is $\omega_{\mathrm{p}j} = n_j e^2 / (\varepsilon_0 m_j)$, where ε_0 is the permittivity of free space. The term ε_∞ is due to any contribution to the dielectric function from higher energy resonance terms, and is a real valued number. The Lorentz model obeys the Kramers-Kronig dispersion relation [78] between the real and imaginary parts of the dielectric function, which are constrained through causality. The Lorentz model is an effective and simple model for phonon modes in the IR region of the spectrum and is widely used to report the dielectric function of materials with phonon bands.

2.1.3 The Drude Model of Free Electrons

The Drude model is a dynamic analog to the Lorentz model but describes the contribution of free electrons to the dielectric function of a material. Essentially, free electrons are damped by scattering, but are not confined to a lattice position by a spring

constant, as in the case of the lattice vibration modes. Thus, very similar to Eq. (2.4) the system has the dynamical equation

$$m_e\mathbf{a} + m_e\gamma_e\mathbf{v} = e\mathbf{E} \tag{2.8}$$

The terms are again the same definitions as in the Lorentz model, but pertaining to electrons rather than atoms. Again, assuming a time harmonic electric field, such as in Eq. (2.2), the solution for the velocity vector can be written as

$$\mathbf{v} = \frac{e/m_e}{\gamma - i\omega}\mathbf{E} \tag{2.9}$$

Since the current is related to the electron drift velocity by $\mathbf{J} = -n_e e\mathbf{v}$, the conductivity is related by complex Ohm's law to the current by $\mathbf{J} = \sigma\mathbf{E}$, and the complex conductivity is related to the dielectric function of the material by [78]

$$\sigma = \sigma' - i\omega\varepsilon \tag{2.10}$$

It can be shown that this systems dielectric function is given by

$$\varepsilon(\omega) = \varepsilon_\infty - \frac{\omega_{\mathrm{p}}^2}{\omega(\omega + i\gamma)} \tag{2.11}$$

where ω_{p} is the plasma frequency, which for most metal falls somewhere in the UV range of the spectrum. The plasma frequency is related to the conductivity of the metal according to $\omega_{pj} = \sqrt{\sigma_0\gamma/\varepsilon_0}$, where σ_0 is the DC electrical conductivity of the material and ε_0 is again the permittivity of free space. The plasma frequency is called such because of the similarity between free electrons in a crystal and an ionized gas. The plasma frequency gives the frequency scale at which electrons are able to relocate quickly enough in response to the oscillations of the driving electric field, and thus effectively cancel out the electric field inside of the medium. Around the plasma frequency metals will be highly reflecting, at lower frequencies the metal is highly

absorbing, and at higher frequencies the electrons cannot respond rapidly enough to the oscillations and the waves are relatively unaffected.

In this work we are concerned with modeling the dielectric properties of films that poses defects that lead to a small free electron concentration, as well as modeling the radiative properties of doped semiconductors and metals, which both have free electron Drude terms.

2.1.4 The Cauchy Equation

In the VIS and NIR region of the spectrum there can still remain some dispersion of the dielectric function due to bandgap transitions. In the spectrum from 370 to 1000 nm, bandgap and lattice absorption in the dielectric materials of interest can be neglected. Therefore, the imaginary part of the dielectric function in this region is very small. It is typical to model the frequency (or wavelength) dependence of the dielectric function in this region with the Cauchy model. The Cauchy dispersion is one of the simplest optical constant formulas with only two adjustable parameters, and it gives the refractive index as a constant with a correction term that is inversely proportional the wavelength squared[79]

$$n(\lambda) = \sqrt{\varepsilon_\infty} = C_1 + \frac{C_2}{\lambda^2} \tag{2.12}$$

Sometimes and additional term of λ^{-4} [7,18,19] is introduced to achieve a better agreement with experimental data. The effect of this higher-order term will negligible at wavelengths greater than 370 nm for the materials considered in this thesis. While the physical basis for the Cauchy dispersion is incorrect, e.g. it is based on an outdated model and it does not meet the Kramers-Kronig relations, the Cauchy equation remains common in optical constant modeling because of its accuracy and simplicity.

2.2 Radiative Properties of Thin Films

2.2.1 Transmittance and Reflectance of Thin Films

If the dielectric function is known, the transmittance and reflectance of film structures can be calculated from ray tracing models. If the coherence length of the film is comparable to the wavelength of light, phase information will be preserved by electromagnetic waves upon multiple reflections within the film. For a free standing film, such as shown in Fig. 2.1, the transmittance and reflectance are given by the Airy formula which has a complex reflection and transmission coefficients given by [78]

$$r = r_{12} + \frac{t_{12}t_{21}r_{23}e^{2ik_{z,2}d}}{1 - r_{21}r_{23}e^{2ik_{z,2}d}} \tag{2.13}$$

$$t = \frac{t_{12}t_{21}e^{ik_{z,2}d}}{1 - r_{21}r_{23}e^{2ik_{z,2}d}} \tag{2.14}$$

The definition of the t_{ij} and r_{ij} are the ratio of the magnitude of the incident electric field to the transmitted or reflected electric field for TE waves, and correspondingly the magnetic field for TM waves, at an interface between two semi-infinite media, *i* and *j*, and are known as the Fresnel coefficients. The Fresnel coefficients between non-magnetic materials *i* and *j* can be determine using

$$r_{ij,\mathrm{TE}} = \frac{k_{iz} - k_{jz}}{k_{iz} + k_{jz}} \tag{2.15}$$

$$t_{ij,\mathrm{TE}} = \frac{2k_{iz}}{k_{iz} + k_{jz}} \tag{2.16}$$

$$r_{ij,\mathrm{TM}} = \frac{k_{iz}/\varepsilon_i - k_{jz}/\varepsilon_j}{k_{iz}/\varepsilon_i + k_{jz}/\varepsilon_j} \tag{2.17}$$

$$t_{ij,\mathrm{TE}} = \frac{2k_{iz}/\varepsilon_i}{k_{iz}/\varepsilon_i + k_{jz}/\varepsilon_j} \tag{2.18}$$

where the k_{lz} is the *z*-component of the wavevector in media *l* when the electric field is decomposed into the form of Eq. (2.2), the ε_l is the relative dielectric constant in this media, and the magnetic permeability is absent from the equations since it is taken to be that of free space (or relative permeability of 1). From Fig. 2.1 it can be recognized that Eqs. (2.13) and (2.14) follow from the sum of the geometric series that results by adding all of the transmitted or reflected components.

The coherence length of a film can be quite complicated to calculate because it depends on the light source, film, and the detector. Since we are dealing with IR radiation anything on the order of microns or thinner may display interference fringes in the transmittance and reflectance because of the exponential terms in Eqs. (2.13) and (2.14). The transmittance and reflectance of the free standing film structure (assuming that medium 1 is lossless) are

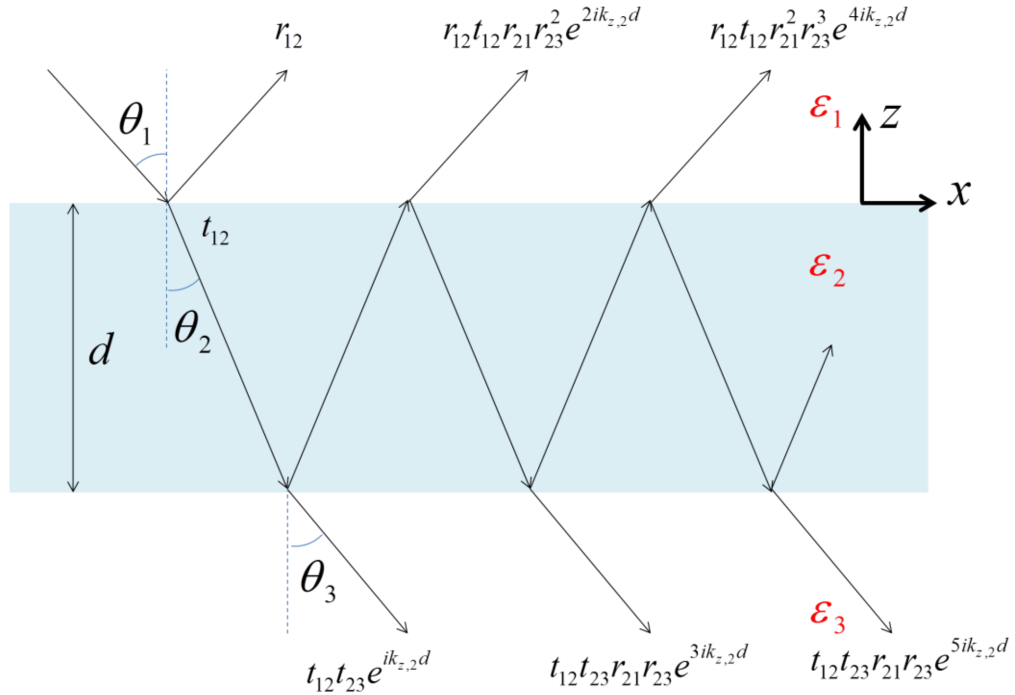

Figure 2.1 Ray tracing in a thin film with multiple reflection. The total transmittance or reflectance is the sum of all of the rays after multiple reflections.

$$R = rr^* \tag{2.19}$$

$$T = \frac{\mathrm{Re}\left(k_{3z}^* / \mu_3^*\right)}{\mathrm{Re}\left(k_{1z}^* / \mu_1^*\right)} tt^* \text{ for TE waves} \tag{2.20}$$

$$T = \frac{\mathrm{Re}\left(k_{3z} / \varepsilon_1\right)}{\mathrm{Re}\left(k_{1z} / \varepsilon_3\right)} tt^* \text{ for TM waves} \tag{2.21}$$

where k_{3z} and k_{1z} are the *z*-component (perpendicular to the film surface) of the wavevector from Eq. (2.2) in medium 3 and 1 respectively and ε_1 and ε_3 are the dielectric function. Note that star denotes the complex conjugate.

2.2.2 Thin Films on Thick Substrates

In the case where there is a thin (coherent) film or multilayer stack of films on a substrate, and the substrate has a coherence length that is shorter than the wavelength of light, the phase information will be lost upon multiple reflections of light in the substrate

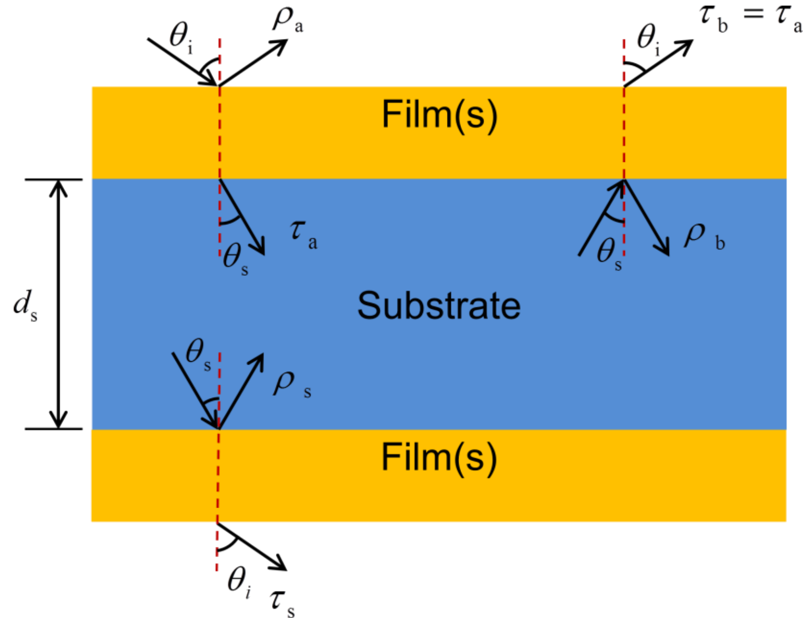

Figure 2.2 Schematic of coherent 1D structure made of one of more layer on top and bottom of an incoherent substrate.

layer. A thin film, or stack of thin films, deposited on this substrate will still have interference effects due to the multiple reflections inside. Figure 2.2 shows a schematic with a generic stack of thin films on the top and bottom of a thick (incoherent) substrate.

Following is an explanation of the definitions of all the variables shown in the figure. The effective reflectance coefficient for incident rays from the ambient top side through the film stack to a semi-infinite substrate is ρ_{a}, and τ_{a} is the corresponding transmittance of this structure. The reflectance coefficient between the substrate and film interface, ρ_{b}, is the reflectance calculated when the incidence is from inside a semi-infinite substrate layer to a semi-infinite ambient through the film stack, and τ_{b} is the transmittance of this structure. The transmittance through the film is independent of the direction and thus τ_{b} is equal to τ_{a}. On the bottom side of the reflectance, ρ_{s}, is the reflectance of a film stack with incidence from semi-infinite substrate to a semi-infinite air and the transmission, τ_{s}, is the transmittance of the same structure. Finally, the internal transmittance of the film is $\tau = \exp\left(-2k_{z,s}''d\right)$, where $k_{z,s}''$ is the imaginary component of the *z*-component (perpendicular to the interface in Fig. 2.2) of the wavevector in the substrate. Notice that this is squared, and hence it is already based on the power decay so that no phase information of the real component of the wavevector is carried. In the case of a single film on top or bottom all of the transmittance and reflectance values can be calculated with the Airy formulas of Eqs. (2.13) and (2.14). In the alternative case that there is no film(s) on the top or bottom of the substrate at all, the transmittance and reflectance are just those of an interface, which is simply based on the Fresnel coefficients from earlier in the chapter. Once the individual components are calculate the overall reflectance and transmittance of the film can be calculated from the following formula for a thin film on thick substrate.

$$R = \rho_a + \frac{\rho_s \tau_a^2 \tau^2}{1 - \rho_s \rho_b \tau^2} \tag{2.22}$$

$$T = \frac{\tau_b \tau_s \tau}{1 - \rho_s \rho_b \tau^2} \tag{2.23}$$

The transmittance is independent of the incident direction because of the symmetry in Eq. (2.23) that occurs when the b and s subscripts are flipped. The reflectance, however, depends on which side the light is incident, and can be found for the backside by applying Eqs. (2.22) and (2.23) to the reverse structure in Fig. 2.2. Energy conservation also implies that the absorptivity of the film(s) on substrate structure will also change depending on the side that light is incident from.

2.2.3 The Transfer Matrix Method

The transfer matrix method is a convenient method to calculate the transmittance and reflectance of multilayer films. It separates the electric field in each layer into a forward and backward propagating component, as shown in Fig 2.3. The amplitude of the forward component in layer *i* is A_i and the amplitude of the backward component is B_i. For TE waves is it more convenient to use the electric field in each layer thus the electric field is given by for TE waves

$$E_i(z) = A_i e^{ik_{iz}(z_i - z_{i-1})} + B_i e^{-ik_{iz}(z_i - z_{i-1})} \tag{2.24}$$

For TM waves the same relation can be obtained by replacing for the electric field with the magnetic field and the magnetic permeability with the dielectric function. Because of the continuity of the tangential component of the electric and magnetic field in each layer the amplitude in layer *i* can be related to the amplitude in layer *i*+1 by a transfer matrix $\mathbf{M}_{i,i+1}$.

$$\begin{bmatrix} A_i \\ B_i \end{bmatrix} = \mathbf{P}_i \mathbf{D}_i^{-1} \mathbf{D}_{i+1} \begin{bmatrix} A_{i+1} \\ B_{i+1} \end{bmatrix} = \mathbf{M}_{i,i+1}^{-1} \begin{bmatrix} A_{i+1} \\ B_{i+1} \end{bmatrix} \tag{2.25}$$

where the propagating matrix is given by

$$\mathbf{P}_i = \begin{bmatrix} e^{-ik_{iz}d_z} & 0 \\ 0 & e^{ik_{iz}d_z} \end{bmatrix} \tag{2.26}$$

in any of the layers except for the semi-infinite first layer where the propagation matrix is simply the identity matrix. The propagating matrix captures the change in phase that wave undergoes traversing the *i*th layer. The dynamical matrix for TE waves, on the other hand, captures the properties of the layer and is given by

$$\mathbf{D}_i = \begin{bmatrix} 1 & 1 \\ k_{iz}/\mu_i & -k_{iz}/\mu_i \end{bmatrix} \tag{2.27}$$

Essentially, combining the dynamical matrix from layer i+1 and the dynamical matrix i

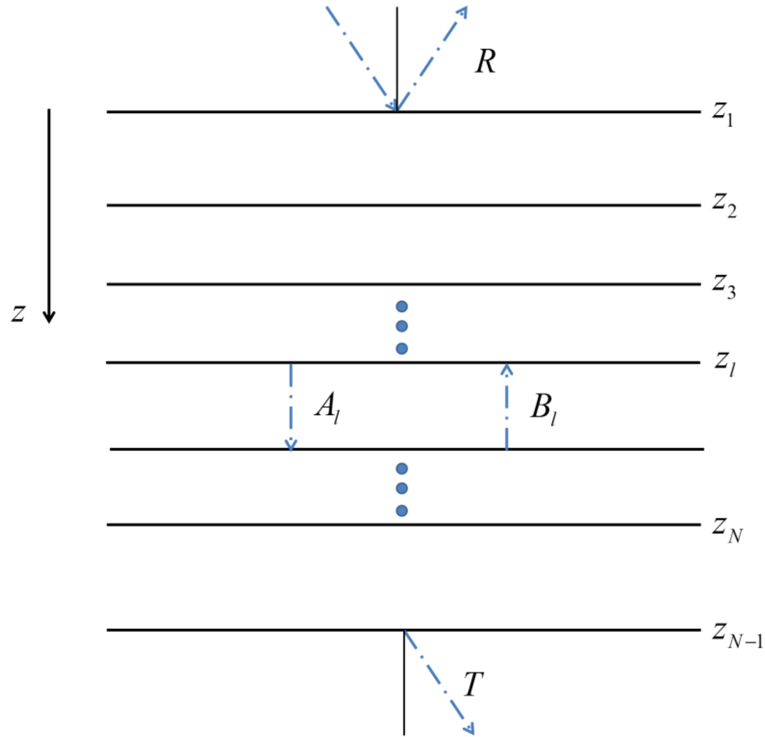

Figure 2.3 Schematic of a multilayer structure for the transfer matrix method, waves incident from a semi-infinite layer propagate through the structure. Every layer except the last has a forward and backward wave, the amplitude in layer l is related to the forward and backward amplitude at the surface by a transfer matrix.

captures the scattering of the electric field due to the abrupt change in layer properties at the interface. For any arbitrary number of layers the total transfer matrix can be calculated as well, and the following equation can be applied to find the field amplitude in relative to the incident amplitude layer.

$$\begin{bmatrix} A_1 \\ B_1 \end{bmatrix} = \prod_{i=1}^{N-1} \mathbf{P}_i \mathbf{D}_i^{-1} \mathbf{D}_{i+1} \begin{bmatrix} A_N \\ 0 \end{bmatrix} = \mathbf{M}_{1,N}^{-1} \begin{bmatrix} A_N \\ 0 \end{bmatrix} \tag{2.28}$$

The field amplitude in any layer can of course be found by

$$\begin{bmatrix} A_1 \\ B_1 \end{bmatrix} = \prod_{i=1}^{l-1} \mathbf{P}_i \mathbf{D}_i^{-1} \mathbf{D}_{i+1} \begin{bmatrix} A_l \\ B_l \end{bmatrix} = \mathbf{M}_{1,l}^{-1} \begin{bmatrix} A_l \\ B_l \end{bmatrix} \tag{2.29}$$

For TM waves, the reciprocity between electric field and magnetic field can be used to find to find the corresponding transfer matrix. The magnetic field in each layer will take the form

$$H_i(z) = A_i' e^{ik_{iz}(z_i - z_{i-1})} + B_i' e^{-ik_{iz}(z_i - z_{i-1})} \tag{2.30}$$

where A_i' and B_i' are the forward and backward amplitude of the magnetic field, which can be evaluated from the TMM if the dynamical matrix for TM waves is modified to be

$$\mathbf{D}_i = \begin{bmatrix} 1 & 1 \\ k_{iz}/\varepsilon_i & -k_{iz}/\varepsilon_i \end{bmatrix} \tag{2.31}$$

The TMM can also apply to a uniaxial anisotropic media, as discussed later in chapter 7.

2.3 Hyperbolic Metamaterials

For multilayered structures with alternating layers of dielectric material with a positive refractive index, and negligible absorption, and a dispersive layer, where the real part of the dielectric function is less than zero, can exhibit unique properties. Typically in the IR these dispersive materials will be doped semi-conductor or metal, which have a Drude term that can lead to a negative refractive index, see Fig. 2.4. The properties of

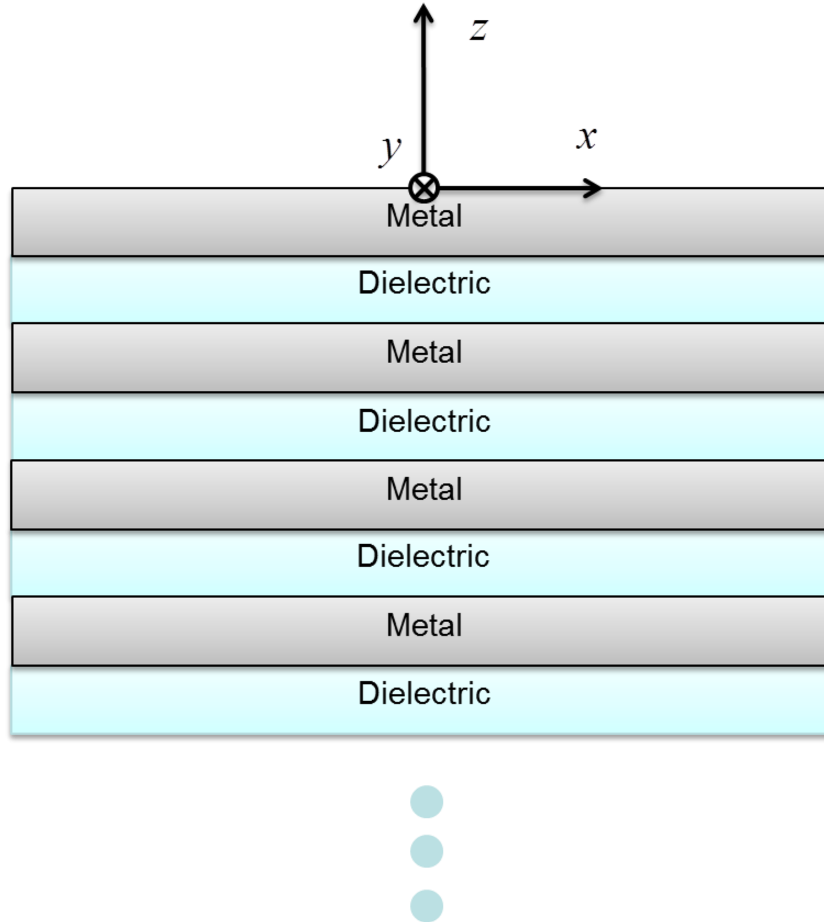

Figure 2.4 Multilayer structure consisting of alternating layers of metal and dielectric which form a metallodielectric photonic crystal.

these multilayer structures can be determined from TMM or they can be treated as a uniaxial homogenized medium with anisotropic properties, with the optical axis in the vertical *z*-direction. Under the effective medium approximation the dielectric function becomes a tensor and has the form.

$$\overline{\overline{\varepsilon}} = \begin{bmatrix} \varepsilon_t & 0 & 0 \\ 0 & \varepsilon_t & 0 \\ 0 & 0 & \varepsilon_z \end{bmatrix} \tag{2.32}$$

where $\varepsilon_x = \varepsilon_y = \varepsilon_t$. For a multilayer laminar structure based on the Wiener formula [80] the dielectric functions are given by

$$\varepsilon_t = f\varepsilon_{\mathrm{m}} + (1 - f)\varepsilon_{\mathrm{d}} \tag{2.33}$$

$$\varepsilon_z = \frac{\varepsilon_\mathrm{d}\varepsilon_\mathrm{m}}{f\varepsilon_\mathrm{d} + (1-f)\varepsilon_\mathrm{m}} \tag{2.34}$$

here the subscripts m and d refer to "metal" and "dielectric", but this is a rather loose term since metal can refer to any dispersive material with the properties that make the real part of one of the equations above exclusively negative. An effect known as screening occurs in a perfect conductor where charges reposition on the surface to cancel the electric field inside. Essentially, these effective formula result from the case where the electric fiend is parallel to the layers and there is no screening (uniform electric field) of the field, Eq. (2.33), and perpendicular to the layer where there is maximal screening (uniform electric displacement), Eq. (2.34) [80]. The coefficient f is the volume filling fraction of the "metal" component.

The dispersion relation for a uniaxial isotropic media is given by the following equations [62]

$$k_\mathrm{oz}^2 + k_t^2 = \varepsilon_t k_0^2 \tag{2.35}$$

$$\frac{k_\mathrm{ez}^2}{\varepsilon_t} + \frac{k_t^2}{\varepsilon_z} = k_0^2 \tag{2.36}$$

where $k_t^2 = k_x^2 + k_y^2$, $k_0 = \omega / c_0$ is the magnitude of the wavevector in vacuum (c_0 is the speed of light in vacuum), k_oz is the *z*-component of the ordinary wavevector, and k_ez is the *z*-component of the extraordinary wavevector. The first equation is for ordinary waves (TE) and is like an effective isotropic media because only one dielectric function is present. The second equation for extraordinary waves (TM) is for an ellipse if both the dielectric functions have the same sign. If the dielectric functions have the opposite signs, then the dispersion becomes a hyperbola. An illustration of the a hyperbolic dispersion is shown in Fig. 2.5. These types of materials are of interest in near-field heat transfer because they have allowed modes with infinite lateral component of the wavevector. It is

these modes, which are normally evanescent in the far-field, that contribute to the enhanced heat flux associated with near-field radiation.

The first type of hyperbolic mode (hyperbolic I) has $\varepsilon_t > 0$ and $\varepsilon_z < 0$ and results in the dispersion shown in Fig 2.5 (a). In a non-absorbing media the group velocity and Poynting vector are perpendicular to the dispersion curve

$$\hat{S} = \frac{1}{|\nabla_{\mathbf{k}}\omega|}\nabla_{\mathbf{k}}\omega \tag{2.37}$$

The Poynting vector **S** shown in (a) exhibits an interesting phenomenon known as negative refraction that has potential applications in near-field imaging where evanescent modes can be imaged allowing the resolution limit of traditional lenses to be exceeded and results in the formation of an image from a flat lens, rather than requiring a curved lens. In negative refraction the vacuum Poynting vector, which is coincident with k_0, is initially pointing to the right in the figure, but is bent backwards to the left when it enters the medium.

The second type of hyperbolic mode (hyperbolic II) has $\varepsilon_t < 0$ and $\varepsilon_z > 0$, and also is a so called indefinite material that can support very large lateral components of the wavevector. However, for small lateral components there will be a forbidden since k_x must be continuous inside of the medium (and there is a region that is disconnected between the hyperbola in the dispersion curve). This material will not exhibit negative refraction but has another interesting property, in that wavevector inside of the medium will have a flipped z-component, since the Poynting vector must point downward as shown in the figure.

Metallic films can exhibit negative refraction since single negative materials (e.g. the magnetic permeability is still positive unlike a double negative material) only require a negative real part of the dielectric function [81]. However, real materials must obey the Kramers-Kronig relations mentioned earlier and will only have a negative real part of the

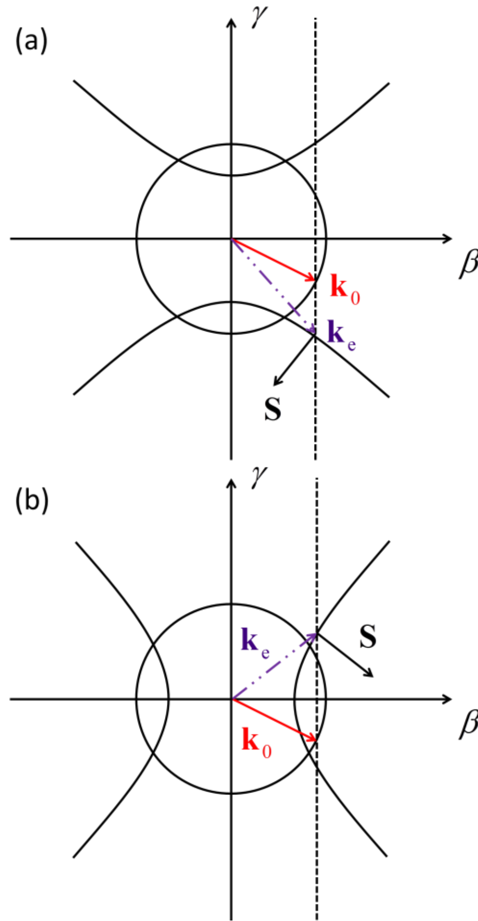

Figure 2.5 The iso-frequency dispersion diagram for hyperbolic materials with: (b) $\varepsilon_{\perp} > 0$ and $\varepsilon_{\parallel} < 0$ the circle represents the dispersion of light incident from vacuum and the hyperbolic curve inside of the anisotropic slab note that the Poynting vector is refracted negatively and (c) $\varepsilon_{\perp} < 0$ and $\varepsilon_{\parallel} > 0$, in this case the pointing vector is not negatively refracted.

refractive index if there is some non-zero imaginary component. This means that single negative materials will be naturally lossy in the region of the spectrum where they exhibit hyperbolic behavior. This shortcoming can be overcome by using multilayer metallo-dielectric photonic crystals or semi-conductor dielectric photonic crystals, which can have a total thickness of the single negative material component that would exceed the bulk skin depth of that material alone.

Finally, noting that the effective medium approximation only applies for certain conditions [82,83] such as the projected wavelength being much larger than the period of

the structure. The hyperbolic dispersion is not the only interesting phenomenon of such structures. There is also another phenomenon in these structures, which is Fabry-Perot like resonance if the dielectric layer thickness is a multiple of the projected wavelength. This work is concerned only with the effective medium and dispersive phenomenon of MDPCs.

2.4 Theory of Near-Field Radiative Heat Transfer

2.4.1 Green's Function and Fluctuation Dissipation Theorem

For radiative transfer in the near field, the time-harmonic Ampere's law needs to be modified to account for random thermal current fluctuations in a dispersive medium [84]

$$\nabla\times\mathbf{H}(\mathbf{r},\omega)=-i\omega\varepsilon\mathbf{E}(\mathbf{r},\omega)+\mathbf{J}_{\mathrm{r}}(\mathbf{r},\omega) \tag{2.38}$$

where $\mathbf{J}_{\mathrm{r}}$ represents random current density fluctuations caused by thermal excitation inside of the media. The other Maxwell's equations retain their usual form [77]. This new set of equations is known as the stochastic Maxwell's equations. The random current sources emit radiation that is distributed across the frequency spectrum according to Rytov [85], who used the fluctuation dissipation theorem to derive the spectral density of current fluctuations, for an isotropic media:

$$\left\langle J_{\mathrm{r},n}(\mathbf{r},\omega)J_{\mathrm{r},j}^{*}(\mathbf{r}'',\omega)\right\rangle=\frac{\omega\varepsilon_0}{\pi}\varepsilon''(\omega,\mathbf{r})\Theta(\omega,T)\delta_{nj}\delta(\mathbf{r}-\mathbf{r}'') \tag{2.39}$$

where $\Theta(\omega,T)$ is the mean energy of the plank oscillator at temperature T, ε_0 is the permittivity of free space, ε'' is the imaginary component of the dielectric function at spatial coordinate $\mathbf{r}$, δ_{nj} is the Kronecker delta, and $\delta(\mathbf{r}-\mathbf{r}'')$ is the Dirac delta function [84]. The mean energy of a Plank oscillator is of course

$$\Theta(\omega,T)=\frac{\hbar\omega}{\exp(\hbar\omega/k_{\mathrm{B}}T)-1} \tag{2.40}$$

where $\hbar$ is Plank's constant divided by 2π and k_B is the Boltzmann constant. Since these fluctuations represent random perturbations that occur even in the absence of temperature gradients, there is no net time-averaged current. Once the spectral density of the fluctuating current is known, the stochastic Maxwell's equations can be solved by considering a random current source in the form of Eq. (2.39).

For planar multilayered 1D structures the Green's function solution to the stochastic Maxwell's equations is found by considering the forward and backward scattered waves generated at interfaces by a current source, as well as direct waves from the source if it is inside of the medium of the receiver [86]. For convenience, the effect of scattering at interfaces is expressed in terms of the coefficients of the traditional transfer matrix for multilayer thin-film optics using the optics formalism introduced by Sipe [86]. In cylindrical coordinates we can expresses the Green's function in terms of the wave vectors β and γ, which are the radial component and *z*-component respectively. These are related to the Cartesian wave vectors used previously according to $\beta^2 = k_x^2 + k_y^2$ and $\gamma = k_z$. Following the work of Francouer et al. [87], the dyadic Green's function for the electric field, $\overline{\overline{\mathbf{G}}}$, and magnetic field, $\overline{\overline{\mathbf{\Gamma}}}$, can be decomposed into an integration over the radial wavevector as

$$\overline{\overline{\mathbf{G}}} = \int_{-\infty}^{\infty} d\boldsymbol{\beta} \overline{\overline{\mathbf{g}}}(\boldsymbol{\beta}, z, z_\mathrm{s}, \omega) \tag{2.41}$$

$$\overline{\overline{\mathbf{\Gamma}}} = \int_{-\infty}^{\infty} d\boldsymbol{\beta} \overline{\overline{\mathbf{h}}}(\boldsymbol{\beta}, z, z_\mathrm{s}, \omega) \tag{2.42}$$

where $\boldsymbol{\beta}$ is the radial component of the wave vector in cylindrical coordinates, which lies in the plane of the interfaces, z_s is the current source location, z is the receiver location, and $\overline{\overline{\mathbf{g}}}$ and $\overline{\overline{\mathbf{h}}}$ are the Weyl representation of the Dyadic Green's functions. Here for the 1D media, *z* is defined into the depth of the cell as shown in Fig. 2.6, and the radial or *x*

and y components would be parallel to the surface of the cell. The electric and magnetic fields are related to the Green's function solution and fluctuating current by

$$\mathbf{E}(\mathbf{r},\omega) = i\omega\mu\int_{V_s} \overline{\overline{\mathbf{G}}}(\mathbf{r},\mathbf{r}_s,\omega)\cdot\mathbf{J}_r(\mathbf{r}_s,\omega)\,d^3\mathbf{r}_s \tag{2.43}$$

$$\mathbf{H}(\mathbf{r},\omega) = \int_{V_s} \overline{\overline{\mathbf{\Gamma}}}(\mathbf{r},\mathbf{r}_s,\omega)\cdot\mathbf{J}_r(\mathbf{r}_s,\omega)\,d^3\mathbf{r}_s \tag{2.44}$$

where the integration is over all of the volume containing fluctuating current sources. These equations of course give the magnetic and electric field at an observation point located at $\mathbf{r}$, due to a random current source, $\mathbf{J}_r$, at $\mathbf{r}_s$. The integration is over the entire volume where the current sources are located, V_s. The Green's function for the electric and magnetic field are related by Maxwell's equations and thus $\overline{\overline{\mathbf{\Gamma}}} = \nabla\times\overline{\overline{\mathbf{G}}}$, the full expressions of the dyadic Green's function are given in the following section, and can be found in ref. [87] , where it is evaluated in terms of the solutions of the transfer matrix method (TMM) [78] for a layered media.

2.4.2 Multilayer Green's Function

Consider an arbitrary multilayer structure shown in Fig 2.6, the random current sources of the fluctuation dissipation theory may be embedded in any arbitrary layer, *s*. The electric and magnetic field in any other layer, *l*, of the structure can then be found from the Green's function for a current source embedded in stratified earth. This problem has been solved previously, but one of the most convenient solution is that of Sipe [86] who applied surface optics to solve the problem. The electric field behaves very much like classical plane wave radiation which emanates from the current source location $\mathbf{r}'$ and the boundary conditions determined by the Fresnel coefficients and phase change under multiple reflections are all similar to classical optics. However, in the case of Near-field radiation the electric field propagation and energy propagation are not necessarily

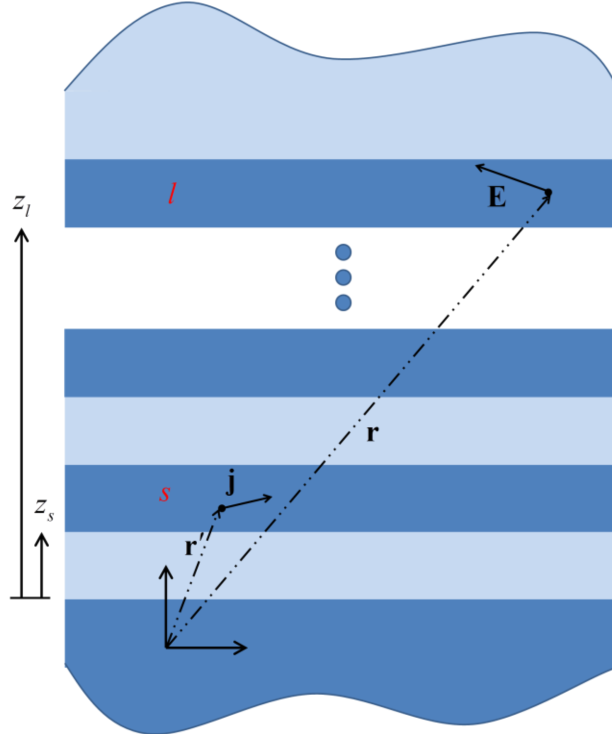

Figure 2.6 Current source imbedded in layer s of a multilayer structure and the electric field it creates in layer l are related by the Green's function.

coincident, which will be a subject of chapter 7. Inside of the layer there will be a portion of the electric field that emanated from the source current that has not been influenced by the boundaries. This is termed the primary component of the Green's function and the Weyl component of Eq. (2.41) is given by [87]

$$\overset{=}{\mathbf{g}}_{\mathrm{P},s}^{\succ\atop\prec}\left(\beta, z, z', \omega\right) = \frac{i}{2\gamma_s}\left[\hat{\mathbf{o}}\hat{\mathbf{o}}e^{\pm i\gamma_s(z-z')} + \hat{\mathbf{p}}_s^{\pm}\hat{\mathbf{p}}_s^{\pm}e^{\pm i\gamma_s(z-z')}\right] \tag{2.45}$$

where γ_l is the z-component of the wavevector in layer l and β is the radial component of the wavevector in layer l. The superscripts $\succ$ indicates that the wave is traveling forward (source located below the receiver) from the source point and $\prec$ indicates that it is traveling backward (source located above the receiver) from the source point. The + or – superscript indicate whether to use the forward or backward TM component of the electric field. The appropriate term must be selected when performing the integration of Eq. (2.41), since if $z > z'$ the forward primary term must be used, and if $z < z'$ the

backward primary wave term must be used. For an isotropic medium the TM vector is given in cylindrical coordinates by

$$\hat{\mathbf{p}}_l^{\pm} = \frac{\mp\gamma_l\hat{\mathbf{r}} + \beta_l\hat{\mathbf{z}}}{\sqrt{\gamma_l{}^2 + \beta_l{}^2}} \tag{2.46}$$

and the TE vector is

$$\hat{\mathbf{o}} = -\hat{\boldsymbol{\theta}} \tag{2.47}$$

This electric field undergoes reflection and refraction as in classic optics. This reflection and refraction results in the following expression in any layer l

$$\begin{aligned}&\overline{\overline{\mathbf{g}}}_{\mathrm{S},l}\left(\beta, z, z', \omega\right)\\ &= \frac{i}{2\gamma_s}\left[\begin{array}{l}\left(A^{+}_{l,\mathrm{TE}} + A^{-}_{l,\mathrm{TE}} + B^{+}_{l,\mathrm{TE}} + B^{-}_{l,\mathrm{TE}}\right)\hat{\mathbf{o}}\hat{\mathbf{o}}\\ \quad + \left(\begin{array}{l}A^{+}_{l,\mathrm{TM}}\hat{\mathbf{s}}^{+}_l\hat{\mathbf{s}}^{+}_s + A^{-}_{l,\mathrm{TM}}\hat{\mathbf{s}}^{+}_l\hat{\mathbf{s}}^{-}_s\\ \quad + B^{+}_{l,\mathrm{TM}}\hat{\mathbf{s}}^{-}_l\hat{\mathbf{s}}^{+}_s + B^{+}_{l,\mathrm{TM}}\hat{\mathbf{s}}^{+}_l\hat{\mathbf{s}}^{+}_s\end{array}\right)\end{array}\right]\end{aligned} \tag{2.48}$$

Where the + or – superscript on the coefficients A_l and B_l indicate whether the term is due to a forward or backward emitting current source as explained in more detail in Ref. [87]. The coefficients A_l and B_l correspond to the wave amplitudes of the forward and backward waves respectively, as can be found by TMM, but the exponential (phase) terms have been absorbed into them to keep Eq. (2.48) compact. The coefficients are defined by first solving the following two matrix equations

$$\begin{bmatrix} A^{+}_{N,\mathrm{TE}} \\ 0 \end{bmatrix} = \mathbf{M}_{s+1,N}\left\{\mathbf{M}_{0,s}\begin{bmatrix} 0 \\ B^{+}_{0,\mathrm{TE}} \end{bmatrix} + \begin{bmatrix} e^{i\gamma_s\left(z_{s+1}-z'\right)} \\ 0 \end{bmatrix}\right\} \tag{2.49}$$

$$\begin{bmatrix} A^{-}_{N,\mathrm{TE}} \\ 0 \end{bmatrix} = \mathbf{M}_{s+1,N}\left\{\mathbf{M}_{0,s}\begin{bmatrix} 0 \\ B^{-}_{0,\mathrm{TE}} \end{bmatrix} + \begin{bmatrix} 0 \\ e^{i\gamma_s\left(z'-z_s\right)} \end{bmatrix}\right\} \tag{2.50}$$

this gives the value of A_N and B_0 in terms of the transfer matrices given in section 2.1.7. Finally, in any layer l

$$\begin{bmatrix} A_{l,\text{TE}}^{+} e^{-i\gamma_l(z-z_{l-1})} \\ B_{l,\text{TE}}^{+} e^{i\gamma_l(z-z_{l-1})} \end{bmatrix} = \begin{cases} \mathbf{M}_{s+1,l}\left(\mathbf{M}_{0,s}\begin{bmatrix} 0 \\ B_{0,\text{TE}}^{+} \end{bmatrix} + \begin{bmatrix} e^{i\gamma(z_{s+1}-z')} \\ 0 \end{bmatrix}\right), & z_l > z_s \\ \mathbf{M}_{0,l}\begin{bmatrix} 0 \\ B_{0,\text{TE}}^{+} \end{bmatrix}, & z_l < z_s \end{cases} \tag{2.51}$$

$$\begin{bmatrix} A_{l,\text{TE}}^{-} e^{-i\gamma_l(z-z_{l-1})} \\ B_{l,\text{TE}}^{-} e^{i\gamma_l(z-z_{l-1})} \end{bmatrix} = \begin{cases} \mathbf{M}_{s+1,l}\left(\mathbf{M}_{0,s}\begin{bmatrix} 0 \\ B_{0,\text{TE}}^{+} \end{bmatrix} + \begin{bmatrix} 0 \\ e^{i\gamma(z'-z_{s+1})} \end{bmatrix}\right), & z_l > z_s \\ \mathbf{M}_{0,l}\begin{bmatrix} 0 \\ B_{0,\text{TE}}^{-} \end{bmatrix}, & z_l < z_s \end{cases} \tag{2.52}$$

Similarly for TM waves you can use the above formalism but the transfer matrix will give you the amplitudes of the forward and backward magnetic field, which does not change direction in each layer. In order to find the amplitude in terms of the electric field you must scale the coefficients by $\sqrt{\varepsilon_l}/\sqrt{\varepsilon_s}$ to account for the different directions of $\hat{\mathbf{p}}_l$ and $\hat{\mathbf{p}}_s$ between layers, for example if the electric field in layer l due to a forward or backward source is given by

$$H_l^{\pm} = A_l'^{\pm} e^{i\gamma(z-z_l)} + B_l'^{\pm} e^{-i\gamma(z-z_l)} \tag{2.53}$$

Has coefficients A_l' and B_l' that are found using the TMM for TM waves, but the coefficients $A_{l,\text{TM}}$ in Eq. (2.48) would be for example

$$A_{l,\text{TM}}^{\pm} = \frac{\sqrt{\varepsilon_l}}{\sqrt{\varepsilon_s}} A_l'^{\pm} \tag{2.54}$$

to find the electric field magnitude from the magnetic field. The total Weyl Green's function in a non-source layer is given by (2.48) but for a source layer the total Weyl Green's function is found by adding Eqs. (2.45) and (2.48). The magnetic green's function can be found by taking the curl of Eqs. (2.45) and (2.48) to give.

$$\overset{=\succ}{\underset{\prec}{\mathbf{h}}}_{\text{P},s}(\beta, z, z', \omega) = \frac{k_s}{2\gamma_s}\left[\hat{\mathbf{p}}_s^{\mp}\hat{\mathbf{o}} e^{\pm i\gamma_s(z-z')} - \hat{\mathbf{o}}\hat{\mathbf{p}}_s^{\pm} e^{\pm i\gamma_s(z-z')}\right] \tag{2.55}$$

$$\overline{\overline{\mathbf{h}}}_{S,l}\left(\beta, z, z', \omega\right) = \frac{k_l}{2\gamma_{sz}}\begin{bmatrix} \left(A_{l,\mathrm{TE}}^{+}\hat{\mathbf{p}}_l^{+} + A_{l,\mathrm{TE}}^{-}\hat{\mathbf{p}}_l^{+} + B_{l,\mathrm{TE}}^{+}\hat{\mathbf{p}}_l^{-} + B_{l,\mathrm{TE}}^{-}\hat{\mathbf{p}}_l^{-}\right)\hat{\mathbf{o}} \\ -\hat{\mathbf{o}}\left(A_{l,\mathrm{TM}}^{+}\hat{\mathbf{p}}_s^{+} + A_{l,\mathrm{TM}}^{-}\hat{\mathbf{p}}_s^{-} + B_{l,\mathrm{TM}}^{+}\hat{\mathbf{p}}_s^{+} + B_{l,\mathrm{TM}}^{+}\hat{\mathbf{p}}_s^{+}\right) \end{bmatrix} \tag{2.56}$$

where the coefficients are the exact same as previously mentioned in the electric Green's function. Once the Green's function components are known the electric field and magnetic field can be found from Eqs. (2.43)and (2.44).

The heat flux can be evaluated from the Green's function solutions by finding the time-averaged Poynting vector from the cross product of the electric and magnetic fields in the usual way.

$$\left\langle \mathbf{S}_{\omega}\left(\mathbf{r}, \omega\right)\right\rangle = \frac{1}{4}\mathrm{Re}\left[\mathbf{E}\left(\mathbf{r}, \omega\right) \times \mathbf{H}^{*}\left(\mathbf{r}, \omega\right)\right] \tag{2.57}$$

Once the z-component of the Poynting vector as a function of depth is determined, the distribution of absorption and penetration depth can be determined from the Poynting vector. Expressing the Poynting vector in the $i \times j$ direction in terms of the Green's functions gives

$$S_{i\times j}\left(\omega, \mathbf{r}\right) = \frac{k_0^2 \Theta\left(\omega, T\right)}{2\pi^2}\mathrm{Re}\left[i\varepsilon''\left(\omega\right)\int_0^{\infty}\beta\int_{z_s}^{z_{s+1}}\left(g_{il}h_{lj}^{*} - g_{jl}h_{li}^{*}\right)dz'd\beta\right] \tag{2.58}$$

thus in an arbitrary laminar structure the heat flux in the z or radial direction comes from Eq. (2.58) by choosing i to be r and j to be θ or i to be z and j to be θ, respectively.

2.4.3 Heat Transfer between Two Semi-Infinite Layers in the Near-Field

For two semi-infinite media, as shown in Fig. 2.7, which are separated by a vacuum gap d the z-component of the heat flux (Poynting vector) can be expressed as a function of the vacuum Fresnel coefficients and mean energy of a Planck oscillator only [69,87].

$$q_\omega = \frac{\Theta(\omega,T_0)-\Theta(\omega,T_2)}{\pi}\left\{\begin{array}{l}\int_0^{k_0}\frac{\beta}{4}\left[\frac{\left(1-|r_{10}|^2\right)\left(1-|r_{12}|^2\right)}{\left|1-r_{10}r_{12}e^{2i\gamma_1' d}\right|^2}\right]d\beta \\ \qquad +\int_{k_0}^{\infty}\beta\left[\frac{\mathrm{Im}(r_{10})\mathrm{Im}(r_{12})}{\left|1-r_{10}r_{12}e^{2i\gamma_1' d}\right|^2}\right]d\beta\end{array}\right\} \quad (2.59)$$

where the first term in the brackets is the propagating component in the vacuum ($\beta < k_0$) and the second is purely evanescent in vacuum ($\beta > k_0$). To solve the above term for either polarization of light the appropriate Fresnel equation r_{ij} between medium i and j should be used. The expression will also apply for uniaxial anisotropic media so long as the reflection coefficients are replaced with their anisotropic counterparts, and the appropriate wave vector z-component for ordinary or extraordinary waves. For reference the Fresnel coefficients for a uniaxial medium with vertical optical axis are given by

$$r_{ij,\mathrm{TE}} = \frac{k_{iz}-k_{jz}}{k_{iz}+k_{jz}} \quad (2.60)$$

$$t_{ij,\mathrm{TE}} = \frac{2k_{iz}}{k_{iz}+k_{jz}} \quad (2.61)$$

$$r_{ij,\mathrm{TM}} = \frac{k_{iz}/\varepsilon_{it}-k_{jz}/\varepsilon_{jt}}{k_{iz}/\varepsilon_{it}+k_{jz}/\varepsilon_{jt}} \quad (2.62)$$

$$t_{ij,\mathrm{TE}} = \frac{2\,k_{iz}/\varepsilon_{it}}{k_{iz}/\varepsilon_{it}+k_{jz}/\varepsilon_{jt}} \quad (2.63)$$

where ε_{lt} is the transverse dielectric function in the lth layer, see Eq. (2.32) for the dielectric tensor of a uniaxial anisotropic media. At small gap spacings the magnitude of the TM contribution to the heat flux will become much larger than the TE wave contribution, so that it may be neglected at very small gap spacings.

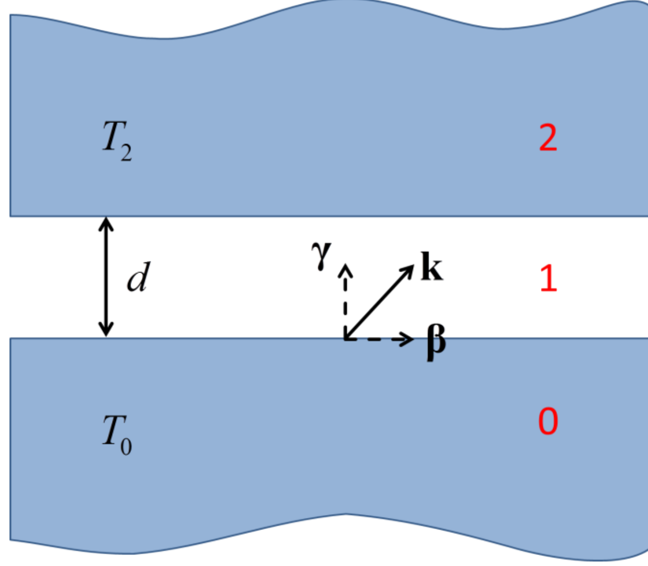

Figure 2.7 Two semi-infinite media labeled 0 and 2 separated by a vacuum gap by a distance of d the components of the wavevector in vacuum are shown. The media are held at temperature T_0 and T_2 respectively.

2.4.4 Energy Streamlines in Near-Field Radiation

Energy streamlines are a convenient method for visualizing energy propagation inside of a media. In the far-field, the energy streamlines (ESLs) can be calculated from the electromagnetic field calculated based on the TMM [78]. The electric field or magnetic field in each layer of a 1D multilayer structure is expressed in terms of a forward and backward propagating component as described previously

$$E_l(z) = A_l e^{ik_{nz}(z-z_{n-1})} + B_l e^{-ik_{nz}(z-z_{n-1})} \quad \text{or} \quad H_l(z) = A_l e^{ik_{nz}(z-z_{n-1})} + B_l e^{-ik_{nz}(z-z_{n-1})} \tag{2.64}$$

where l is the index of the lth layer and k_{lz} is the z-component of the wavevector in the lth layer and A_l and B_l are the amplitudes of the forward and backward propagating waves. The ESLs are calculated from the electric and magnetic field of a solution of the Maxwell's equations found using the TMM. The ESLs for TM waves in a 1D structure

can be calculated by determining the components of the Poynting vector in x and z direction using the following equations [78].

$$\begin{aligned}\langle S_z \rangle = \frac{1}{2\omega\varepsilon_0}\mathrm{Re}\left(\frac{k_z}{\varepsilon}\right)\left[|A|^2 e^{-2k_z'' z} - |B|^2 e^{-k_z'' z}\right] \\ -\frac{1}{\omega\varepsilon_0}\mathrm{Im}\left(\frac{k_z}{\varepsilon}\right)\mathrm{Im}\left(AB^* e^{2ik_z' z}\right)\end{aligned} \quad (2.65)$$

$$\begin{aligned}\langle S_x \rangle = \frac{k_x}{2\omega\varepsilon_0}\mathrm{Re}\left(\frac{1}{\varepsilon}\right)\left[|A|^2 e^{-2k_x'' x} - |B|^2 e^{-k_x'' x}\right] \\ -\frac{k_x}{\omega\varepsilon_0}\mathrm{Re}\left(\frac{1}{\varepsilon}\right)\mathrm{Im}\left(AB^* e^{2ik_x' x}\right)\end{aligned} \quad (2.66)$$

the ESLs are formed by tracing the streamlines with slope or propagation angle

$$m = \frac{\langle S_x \rangle}{\langle S_z \rangle}, \qquad \phi = \arctan\left(\frac{\langle S_x \rangle}{\langle S_z \rangle}\right) \quad (2.67)$$

respectively. The ESLs are then generated by tracing curves in the direction of the slope, similar to ESLs in fluid mechanics.

In near field heat transfer the Poynting vector in an arbitrary multilayer structure can be found using Eq. (2.58) and the energy streamlines can be determined from (2.67). In most cases, the fields can be expressed in the near-field as in Eqs. (2.65) and (2.66) since the solutions of the electromagnetic field can still be treated as forward and backward waves. However, in an emitting layer there will be a source term in the Green's function equation leading to an additional field term that is not due to multiple reflections that needs to be considered in the calculation of the energy streamlines in a source layer [75]. Note that Eq. (2.67) is general and will apply for an anisotropic or isotropic media once the Poynting vector is known. More details about the calculation of energy streamlines in isotropic media in the near-field can be found in Refs. [74–76]. The ESLs for a uniaxial anisotropic MDPC are the topic of chapter 7 where the calculation will be discussed in more detail.

CHAPTER 3

SPECTROSCOPIC TECHNIQUES

Chapter 3 describes the basic characterization equipment used to measure the transmittance and reflectance of the films in order to determine the optical constants of HfO_2 and Ta_2O_5 films on Si substrates presented in both chapters 4 and 5, respectively.

3.1 Fourier Transform Infrared Spectrometry

The NIR/MIR transmission and reflectance of each sample were measured with an ABB FTLA 2000 FTIR from 500-10000 cm^{-1} (wavelengths from 1 to 20 μm). The FTIR chamber was purged with nitrogen gas to minimize the absorption by carbon dioxide and water vapor. A resolution of 4 cm^{-1} was used to remove the interference fringes in the Si substrate. A 10º incidence reflectance accessory was used along with the FTIR to measure the near-normal reflectance. The reflectance measurements were made for radiation incident on either the film side (R_f) or the substrate side (R_s) as illustrated in

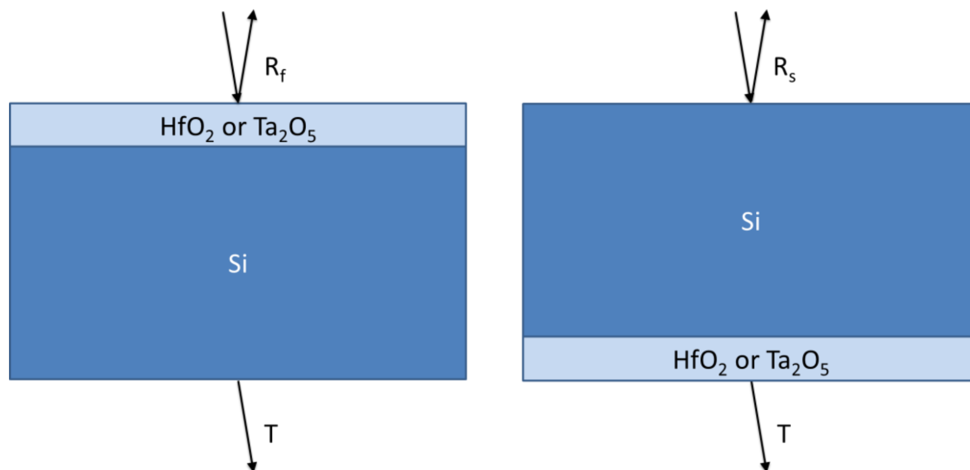

Figure 3.1 Measurement setup for transmittance (T), film reflectance (R_f), and substrate reflectance (R_s) of the films using FTIR. Note that the transmittance is shown near normal but is actually measured normal to the film while reflectance is taken at near normal incidence.

Fig. 3.1. The equations for the case of a thin film on thick substrate are presented here for convenience. The transmittance and reflectance for a thin film on a thick substrate can be expressed as follows [88]:

$$T = \frac{\tau_a \tau_s \tau_i}{1 - \rho_s \rho_b \tau_i^2} \tag{3.1}$$

$$R_f = \rho_a + \frac{\rho_s \tau_a^2 \tau_i^2}{1 - \rho_s \rho_b \tau_i^2} \tag{3.2}$$

$$R_s = \rho_s + \frac{\rho_b \tau_s^2 \tau_i^2}{1 - \rho_s \rho_b \tau_i^2} \tag{3.3}$$

where the subscript f or s in the reflectance R signifies the film-side or substrate-side incidence. In Eqs. (3.1) – (3.3), τ_i is the internal transmissivity of the substrate, τ_a and ρ_a are the transmittance and reflectance at the air-film interface when the substrate is semi-infinite, ρ_b is the reflectance for incidence from the substrate at the interface between the substrate-air interface assuming that the substrate is non-absorbing and semi-infinite, and τ_s and ρ_s are the transmittance and reflectance at the air-substrate interface when both media are semi-infinite [78,88,89]. Most of the fitting in the subsequent chapters is based on the transmittance only and the reflectance model is compared with the reflectance data to confirm the fitting results. The reason for using transmittance only is because the reflectance measurements are subject to a larger relative uncertainty of around 5%.

A gold mirror was used as the reference for the reflectivity measurements, the reflectivity of the mirror can be obtained from the handbook values [90] with an assumption that the reflectivity remains the same beyond 10 μm. The procedures of measurement and data reduction can be found from previous studies [91,92]. The estimated measurement uncertainties are 0.01 in transmittance and 0.02 in reflectance, are based on Ref. [93].

A higher resolution of 1 cm^{-1} was also used to measure the transmittance of a bare Si substrate cut from the same batch of 432 μm thick wafers. The interference effects are revealed by the oscillations in the spectrum, which allow the determination of the substrate thickness using the optical constants of Si tabulated in the handbook [90]. Note that the Si substrate is lightly boron-doped with an electric resistivity close to 10 Ω·cm with a crystalline orientation (100). The transmittance was used to determine the substrate thickness d_{Si}, based on the equation $\Delta\nu = (2n_{Si}d_{Si})^{-1}$ [78], where $\Delta\nu$ is the free spectral range (i.e., spacing between adjacent interference maxima) and n_{Si} is the refractive index of Si. This results in $d_{Si} = 432\pm5$ μm, which is needed for the calculation of radiative properties of the film-substrate composites. The calculated transmittance and reflectance of the Si substrate based on the incoherent formula [78] agrees well with the lower-resolution (4 cm^{-1}) measurements from the FTIR, except in the region from 1000-1400 cm^{-1}, where absorption of interstitial oxygen becomes important. To account for the interstitial oxygen absorption in the Si wafer, the extinction coefficient is increased (without changing the refractive index) until the calculated transmittance spectrum matches the FTIR measurements. This procedure is adopted from the previous work by Basu et al. [91]. Note that the 750 μm thick wafers were manufactured by the same Czochralski growth process and by the same manufacturer (Virginia Semiconductor), so that the same optical constants determined from the 432 μm wafers may also be applied to these wafers with good agreement.

Figure 3.2(a) shows the measured and calculated transmittance of a bare Si substrate from 500 to 10000 cm^{-1}, with a detailed view of spectra from 500 to 2000 cm^{-1} in Fig. 3.2(b). The cutoff in transmittance near 10000 cm^{-1} is due to bandgap absorption [78]. Absorption due to lattice vibrations and impurities lies in the region from 500 and 1500 cm^{-1} as shown on Fig. 3.2(b), where the calculation using optical constants from Palik [90] over predicts the transmittance around 1100 cm^{-1}. By modifying the extinction

coefficient κ from 1000 to 1400 cm^{-1}, good agreement is achieved between the measured and calculated transmittance. Figure 3.2 also demonstrates the accuracy of the FTIR measurements, which correlate well to the calculated values. It should be noted that the effect of 2-4 nm thick native oxide, SiO_2, on the surfaces of the wafer has a negligible effect on the transmittance and reflectance. This statement remains true even in chapters 4 and 5, where some of the samples studied are annealed, because the time and

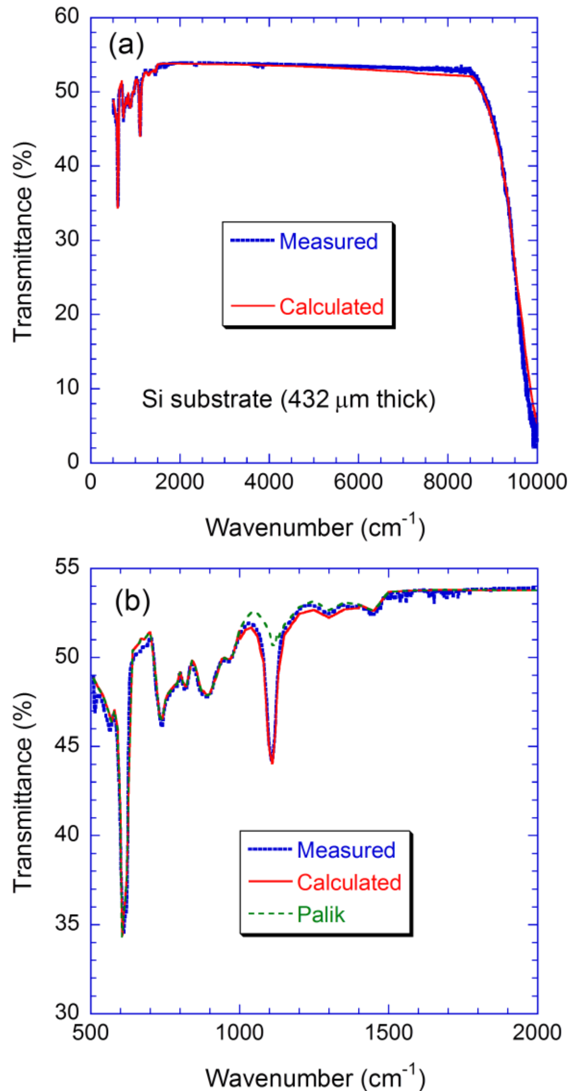

Figure 3.2 Comparison of measured and calculated transmittances for a bare Si substrate of thickness $d_{Si} = 432$ μm: (a) from 500 to 10000 cm^{-1}; (b) zoomed in region from 500 to 2000 cm^{-1} showing lattice and impurity absorption.

temperatures are low enough for the increase in oxide thickness to remain negligible.

The transmittance was measured in the far-infrared range using a Bruker 113v FTIR spectrometer with a beam divergence of 8.3° (half cone angle) and a resolution of 2 cm^{-1}. The interference effect in the Si substrate is inevitable in the measured far-IR spectrum. To reduce the interference effect, the transmittance of each sample was normalized to that of a bare Si substrate (T_{Si}). For the FIR setup the whole system must be vacuum sealed and evacuated to eliminate vapor absorption. The sample holder contains a rotatable wheel that allows multiple samples to be measured in succession without having to re-pump the system. Four of the samples were deposited on 432±5 μm thick Si substrates with a resistivity of 20 Ω·cm (measured by fitting the FIR transmittance spectrum), and the remaining two were deposited on 750±25 μm thick Si substrates with a resistivity between 10 and 100 Ω·cm as specified by the manufacturer. The resistance of the thinner Si substrate was determined by fitting the well-known Drude model for boron-doped Si to the transmittance of the Si in the far-IR spectrum according to Fu and Zhang [94] and references therein. The doping level was thus estimated to be 6.67×10^{14} cm^{-3}. The transmittance spectrum of Si calculated from the incoherent formula based on the Drude model was used to deduce the transmittance data of the samples in the far-IR region from the relative measurements. The Drude model is also used to calculate the radiative properties of the film-substrate composite in the far-IR region ($\lambda > 20$ μm) in the line-shape analysis. The effect of the Drude term is negligible at wavelengths shorter than 20 μm. It is shown by comparison with the transmittance of a bare Si substrate that the optical constants from Ref. [90,95] are suitable for modeling the near- and mid-IR radiative properties with the thicker substrate, whose resistivity does not need to be precisely determined.

3.2 Ellipsometry

Ellipsometry is a reflectance measurement of a ray with known polarization, and differs from a normal reflectance measurement in that it measures not only the amplitude of the reflected light from a structure, but the change polarization upon reflection as well. The fundamental equation of ellipsometry is [47,48]:

$$\rho = \frac{r_{\mathrm{p}}}{r_{\mathrm{s}}} = \tan(\Psi) e^{i\Delta} \tag{3.4}$$

where r_{p} and r_{s} are the complex reflection coefficients for *p* polarization (TM wave) and *s* polarization (TE wave), respectively. For this work we are only concerned with films on an opaque substrate of Si only. The coefficients in Eq. (3.4) can be found from Eq. (2.13) for each of the polarizations respectively. From the ellispometry measurement, the quantities Ψ and Δ are typically obtained and then used to determine the optical constants as well as the film thickness. Note that the first variable $\tan(\Psi)$ contains information about the relative amplitude and the term $e^{i\Delta}$ contains phase information. Because phase information is retained in ellipsometry measurements it helps eliminates potential redundancy when determining the optical constants of a film. The following quantities are usually introduced, by definition, to facilitate the fitting of ellipsometry data:

$$N = \cos 2\Psi,\ S = \sin 2\Psi \sin\Delta, \text{ and } C = \sin 2\Psi \cos\Delta \tag{3.5}$$

The magnitude of $\sqrt{N^2 + S^2 + C^2} \le 1$ implies that the quantities *N*, *S*, and *C* scale similar to the transmittance and reflectance. In an ideal case for which $\sqrt{N^2 + S^2 + C^2} = 1$, only two quantities are necessary in the fitting.

A simple schematic of an ellipsometry system is shown in Fig. 3.3. A J.A. Woollam M2000 spectroellipsometer (SE) was used to study the optical properties at wavelengths from 370 to 1000 nm at four incidence angles (60°, 65°, 70°, and 75°). The

M2000 is more complicated than the basic setup in Fig. 3.3, because it has some additional components such as a rotating compensator added into the beam path, which allow more accurate measurement of the ellipsometry parameters. However, the basic operating principle is still the same, the polarizer before the detector (called the analyzer) is rotated to determine the polarization of the reflected light. The additional rotating compensator component allows the handedness of the reflected light to be deduced as well, which cannot be determine in the traditional setup. The M2000 also uses a CCD array detector and can do a broad range of wavelengths simultaneously; it is capable of being configured to measure from 190 nm to 1.7 μm. Once obtained, the experimentally obtained parameters (Ψ and Δ) were then fit with the software package CompleteEASE associated with the Woollam SE. The SE data can also provide the thickness values and the surface roughness information as discussed in the following chapters.

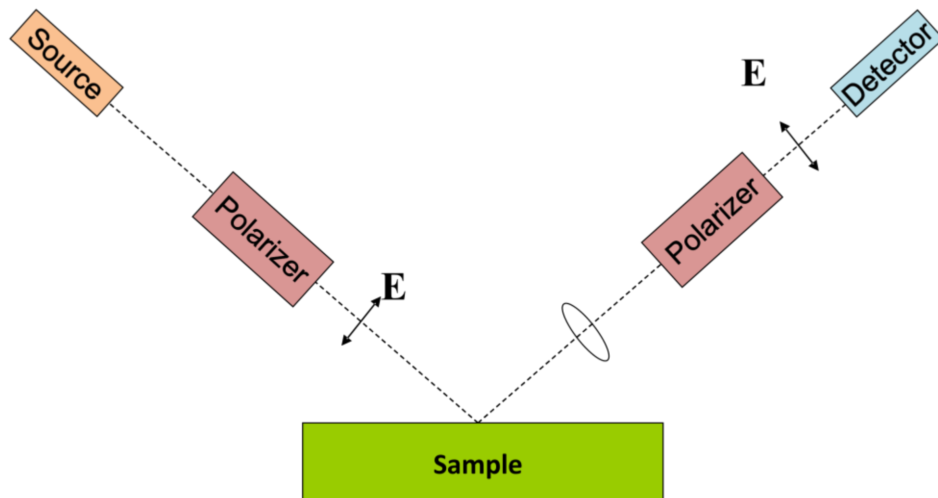

Figure 3.3 Schematic of a basic ellipsometry which consists of a light source, a linear polarizer that gives the incident light a known polarization, and a rotating polarizer (analyzer) with a detector that measures the elliptical shape of the polarization of reflected light.

CHAPTER 4

DIELECTRIC FUNCTION OF MAGNETRON SPUTTERED HFO_2 THIN FILMS

This chapter describes an investigation of HfO_2 optical properties from the VIS to FIR with a focus on the NIR and MIR region, where phonon absorption is insignificant, for applications as a non-absorbing optical coating. HfO_2 films were deposited on double-side polished Si substrates using DC magnetron sputtering and the films were characterized with X-ray diffractometry (XRD) and atomic force microscopy (AFM). A Fourier-transform infrared (FTIR) spectrometer measured the near-normal transmittance and reflectance for incidence on both the film side and the substrate side from 1 to 20 μm wavelengths. By comparison of the experimental results with those calculated from a Lorentz oscillator model, the thicknesses and oscillator parameters in the Lorentz model were obtained. The optical constants from 370 to 1000 nm wavelengths were obtained from spectroellipsometry (SE) and fitted to a Cauchy formula. Furthermore, the ratio of the FIR transmittance with film and without film was measured with another FTIR at frequencies from 20 to 650 cm^{-1} to reveal phonon vibration bands. A hafnia dielectric function, which combines the Cauchy formula and the multiple-oscillator model, is proposed for use in the wavelength region from 370 nm to about 500 μm.

4.1 Film Characterization

HfO_2 films of different thicknesses were prepared on silicon (Si) substrates using DC magnetron sputtering. A 100 mm diameter Si wafer, polished on both sides, was diced with a diamond stylus to square pieces with approximately 18 mm × 18 mm. The wafer's thickness is approximately 430 μm. Prior to insertion into the processing chamber, which had a base pressure less than 1.3×10^{-6} Pa, the Si wafers were cleaned in

solvent. They were then cleaned by Ar^+ ion bombardment for removal of adsorbed hydrocarbons and the native oxide layer of 1-2 nm thickness. After cleaning, a 2.5 cm diameter, 99.9% pure Hf target was sputtered in an Ar-O_2 background. Input power was held at a constant 30 W with an Ar flow rate of 22 sccm and O_2 flow rate of 2.5 sccm and total pressure of 1.3 Pa. All process gases used in the deposition were > 99.999% pure. The substrates were maintained at 300 ºC during deposition. A picture of the deposition chamber, located at the Air Force research lab in Dayton, OH, is included in Fig. 4.1. The substrate is on a rotating stage at the bottom of the figure. Underneath the stage (not shown) is a tungsten filament that heat the sample up to the desired temperature, the

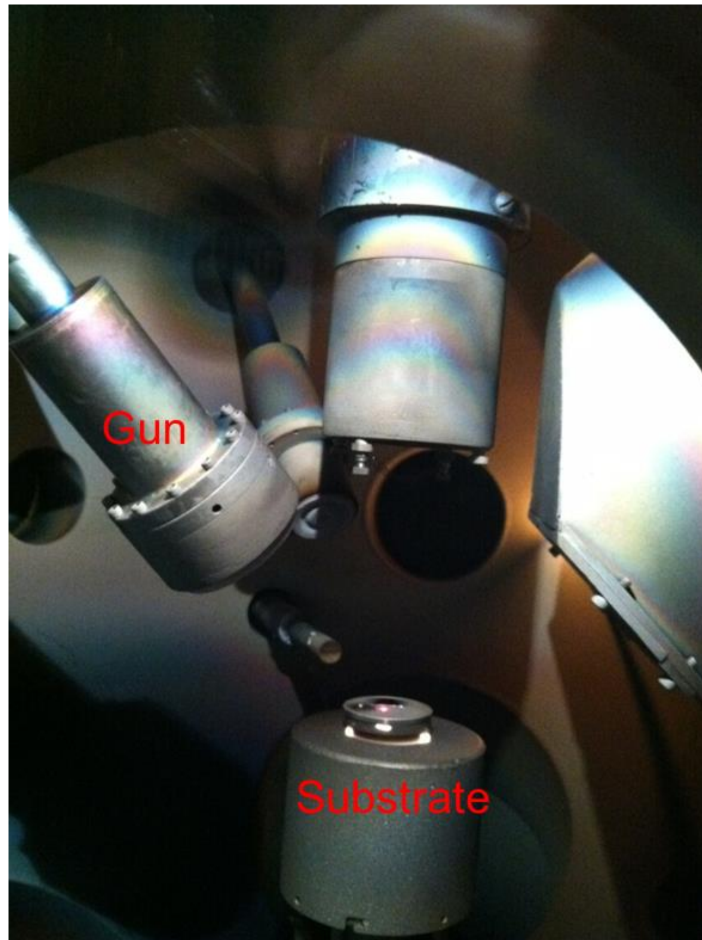

Figure 4.1 Picture of inside of deposition chamber. The sample substrate sits on a rotating stage that is heated from the backside with a tungsten filament.

sample temperature is measured with a radiometer to ensure constant substrate temperature during the deposition. The sputtering gun and a target can be seen in the image as well.

In order to determine crystal structure and phase, X-ray diffraction (XRD) measurements of annealed and unannealed samples were performed using Rigaku D-Max diffractometer in a Bragg-Brentano configuration. Due to the small thickness of the films, grazing incidence XRD was also measured at an inclination angle of 8°, using a PANalytical X'Pert PRO Alpha-1 X-ray diffractometer (XRD) with Cu K_a radiation (0.154 nm). Surface topography was measured using a Veeco Dimension 3100 AFM in tapping mode over a 2 μm × 2 μm scan area. The AFM probe was an uncoated *n*-type Si probe of 10 nm in radius.

Throughout this chapter, the analyzed films are labeled HAF01, HAF02, HAF03, and HAF04a, in the order of decreasing deposition time. Films HAF03 and HAF04a had the same deposition time, with the difference between the two being HAF04a was

Table 4.1 Sample deposition conditions and characteristic parameters obtained from different methods. HAF04a is annealed in air after the deposition for 1 hr at 800 °C, while the rest are as-deposited. Here, *A* and *B* are parameters in the Cauchy dispersion obtained from fitting the ellipsometry measurements. The average values for *A* and *B* are 1.956±0.009 and 0.0172±0.0024 μm^2, respectively.

Sample label	HAF01	HAF02	HAF03	HAF04a
Deposition time (min)	554	375	188	188
Post-processing	No	No	No	Annealed
Roughness, σ (AFM) (nm)	7.2	6.4	4.8	4.8
Thickness, *d* (FTIR) (nm)	516	354	184	197
Thickness, *d* (Ellipsometry) (nm)	498	347	168	176
Roughness, σ (Ellipsometry) (nm)	15.5	11.8	9.6	9.5
Dispersion constant, *A*	1.963	1.959	1.955	1.948
Dispersion constant, *B* (μm^2)	0.0153	0.0189	0.0162	0.0183

annealed in air at 800 ℃ for 1 hr, and HAF03 and the other samples remained in the as-deposited state for all characterizations. Some characteristic parameters of the prepared films are listed in Table 4.1 together with the processing parameters, which are described in detail in subsequent sections. As can be seen from Table 4.1, the deposition rate is approximately 1.0 nm/min for all samples. The nominal HfO_2 thicknesses are 500 nm, 350 nm, and 180 nm for HAF01, HAF02, and HAF03, respectively, although the tabulated thickness exhibits some dependence on the method used for measurement.

The grazing angle XRD profiles are stacked in Fig. 4.2 for the three thinner samples. The intensity peaks are matched using the powder diffraction file for monoclinic HfO_2 from the International Centre for Diffraction Data (ICDD PDF: 04-004-9021) [96] to identify various crystalline orientations. The broad intensity peaks suggest a polycrystalline monoclinic hafnium oxide in all three films. There is no detectible

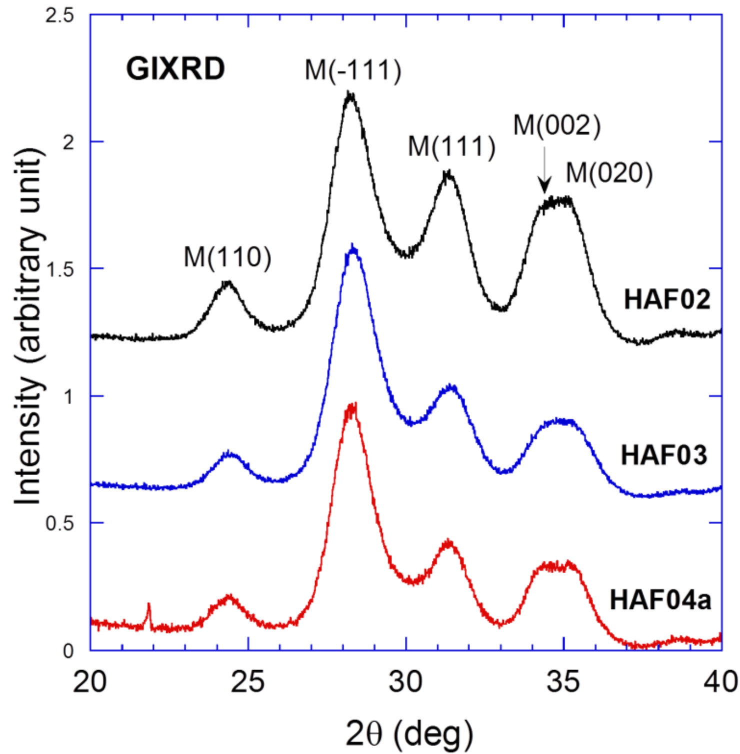

Figure 4.2 XRD patterns for samples of different thickness with the polycrystalline monoclinic phase of HfO_2 identified.

difference in the crystallinity of the annealed and unannealed films with comparable thicknesses (HAF04a and HAF03). From Fig. 4.2, there is a slight change in the preferred crystallite orientation as the sample thickness increases. All films were nanocrystalline and the average grain size was estimated to be around 12 nm based on the Scherrer formula [37] using the Rigaku XRD data because the grazing angle XRD causes additional broadening.

AFM scans with 512 ± 512 array of data were performed in two locations on each sample and the difference was negligible. The average value of the root-mean-square (RMS) roughness σ is listed in Table 4.1 for all samples. Film HAF01 was thicker and had a relatively larger RMS roughness than that of film HAF04a. For a bare Si substrate, the RMS roughness measured by the AFM gives a value less than 2 nm. Typical surface

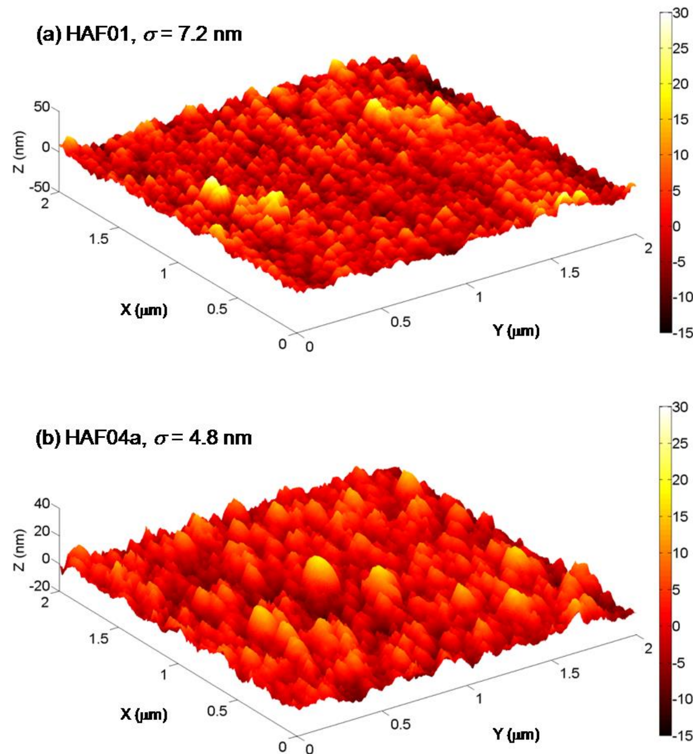

Figure 4.3 AFM images of two HfO_2 films deposited on Si substrates: (a) HAF01; (b) HAF04a.

images are shown in Fig. 4.3 for HAF01 and HAF04a films. Overall, the films are very smooth with an RMS roughness of 5-7 nm based on the AFM measurements. It should be noted that films with slightly different thicknesses would appear in different colors. Observation of the color uniformity with naked eyes suggests that the film thickness is very uniform on each sample.

4.2 Optical Measurements of Thin Films

The spectrometric results in the NIR/MIR region are presented in Sec. 4.2.1, followed by a detailed analysis in Sec. 4.2.2. The SE results and dispersion in the VIS/NIR region are described in Sec. 4.2.3. The FIR data are presented in Sec. 4.2.4 with the multiple-oscillator model, which also incorporate the dispersion in the VIS/NIR region.

4.2.1 NIR/MIR Results

The radiative properties (T, R_f, and R_s) in the NIR/MIR are plotted in Fig. 4.4. The spectra of the annealed HAF04a film are very similar to those of HAF03 film, and are therefore not shown. The reflectance is measured for incidence from either the film side or the substrate side. In order to clearly display the effect of absorption, the spectrum is divided according to the wavenumber (ν) regions from 500 to 1500 cm^{-1} (left) and from 1500 to 8500 cm^{-1} (right). The large noise in the reflectance spectra at $\nu > 6500$ cm^{-1} is due to a low signal-to-noise ratio. The purge with nitrogen gas did not completely remove the water vapor and CO_2 absorption in the sample compartment, causing some artifacts around 1500, 2350, and 3800 cm^{-1} [78,91]. There are two transmittance maxima and one minimum for HAF01 film; one maximum and one minimum for HAF02 film; and one maximum for HAF03 film. It can be inferred that the zero frequency is a transmittance minimum or reflectance maximum if absorption did not occur. In the non-absorbing region, the reflectance should be independent of which side the radiation is incident from.

The disagreement between R_f and R_s is mainly caused by measurement uncertainty, especially for HAF02 film for which R_s is obviously too high. When the transmittance and reflectance are added, the results are close to 100% within 2-3% deviation. However, an additional absorption feature appears in the T and R_f spectra between 2800 and 3700 cm^{-1}, but not in the R_s spectrum. This can be explained by moisture adsorbed in the hafnia film due to O-H stretching vibrations [30,47].

At longer wavelengths, absorption bands in Si can be distinguished by comparison with Fig. 3.2(b). Although HfO_2 possesses lattice vibration bands between 500 and 800 cm^{-1} [30,35], their effect on the radiative properties is largely screened by the substrate absorption. Note that measurements close to the cutoff frequency of 500 cm^{-1} are also subject to large uncertainties. In general, the absorption in HfO_2 increases toward longer wavelengths. This is evident since the transmittance of the samples is lower and decreases quicker (toward smaller wavenumbers) than that of a bare Si substrate. Furthermore, the transmittance at $\nu < 850$ cm^{-1} is lower for thicker samples. Moreover, the absorption by HfO_2 films gives rise to an increased R_f. Interestingly, if the absorptance of film and substrate is calculated according to $\alpha_f = 1 - T - R_f$ and $\alpha_s = 1 - T - R_s$, then $\alpha_s > \alpha_f$ when $\nu < 650$ cm^{-1}. The larger absorptance for substrate-side incidence than for film-side incidence has been also reported before for absorbing films such as superconducting thin films [97].

4.2.2. Single-oscillator Model

Interference effects in the Si substrate do not appear in the spectra of Fig. 4.4, due to the relatively low resolution. The RMS roughness measured from AFM suggests that the surfaces (Table 4.1) can be treated as perfectly smooth in the NIR/MIR region. Therefore, the hafnia film can be modeled as coherent while the substrate can be assumed as incoherent without considering interference effects. The model for thin film(s) on a thick substrate can be applied to predict the spectral transmittance and reflectance

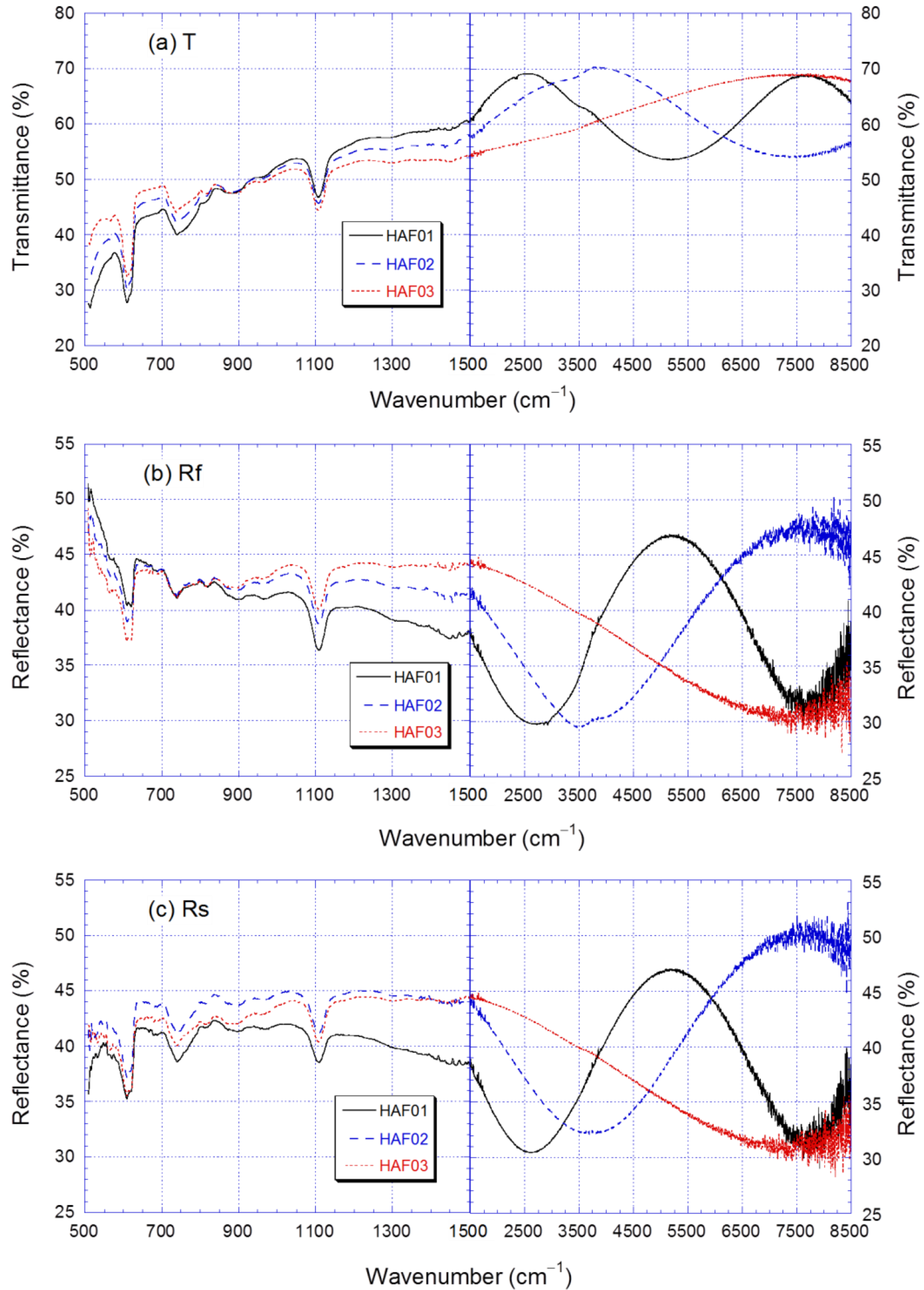

Figure 4.4 Measured mid-infrared radiative properties of three HfO_2 film-substrate composites: (a) transmittance, T; (b) reflectance for incidence on the HfO_2 film side, R_f ; (c) reflectance for incidence on the Si substrate side, R_s . The wavenumber scales are different between the left and right regions in order to show the spectra from 500 and 1500 cm^{-1} clearly.

[78,89,91], giving T, R_f and R_s as functions of the optical constants and thicknesses of the film(s) and substrate. Detailed expressions and algorithms can be found from Zhang [78] and was discussed previously in chapter 3.

In the region where absorption in both the film and substrate is negligible, corresponding to wavenumbers greater than 2000 cm^{-1} in the present study, the interference fringes in the transmittance spectrum provide quantitative information of both film thickness (d) and refractive index (n) for known refractive index of substrate (n_{Si}). Note that the refractive index of Si changes by merely 1% from 2000 to 8000 cm^{-1}. Since the refractive index of HfO_2 is less than that of Si, the film acts as an antireflective coating [78,89]. Assuming n does not change, then the fringe spacing (free spectral range) $\Delta\nu = (2nd)^{-1}$ can be used to estimate the product of n and d, if there exist sufficient number of fringes. Thus a thicker film is preferred and this method is not suitable for very thin films. On the other hand, the envelope method [98] can be used based on the maxima or minima in T. It can be shown that without absorption, the maxima in T can be expressed as

$$T_{\max} = \frac{4n^2 n_{Si}}{n^4 + n^2\left(n_{Si}^2 + 1\right) + n_{Si}^2}, \quad \text{for } n < n_{Si} \tag{4.1}$$

while the minima in T only depend only on the refractive index of Si given by

$$T_{\min} = \frac{2n_{Si}}{n_{Si}^2 + 1}, \quad \text{for } n < n_{Si} \tag{4.2}$$

If the refractive index of the film is greater than that of the substrate, Eqs. (4.1) and (4.2) gives the transmittance minima and maxima, respectively [98]. Eq. (4.1) has two reasonable solutions with $n < n_{Si}$. For $0.690 < T_{\max} < 0.695$, it can be shown that n should be about 1.9 with 10% relative variation. Considering the measurement

uncertainty, the envelope method can give a rough estimate of the refractive index and thus the film thickness.

When $\nu < 1000\ \mathrm{cm}^{-1}$, absorption by HfO_2 film increases toward longer wavelengths due to absorption by IR phonons. One can use the known optical constants and thickness of Si to extract n and the extinction coefficient, κ, of the film at each measured wavenumber. Multiple solutions exist but a careful selection can be made to obtain reasonable values of the optical constants of HfO_2 using the sample HAF01 with the thickest film. However, the optical constants obtained from such point-by-point solution fluctuate due to measurement uncertainty and noise, as well as other artifacts such as the residual CO_2 gas, water vapor in the sample compartment and water adsorbed on the film surface. Nevertheless, the guidance gained from the envelope method approximation and point-by-point solution helps to understand the behavior of the optical properties of HfO_2 for more accurate modeling described below.

Due to the low-frequency cutoff of the FTIR at about 500 cm^{-1}, the exact phonon vibration frequencies cannot be determined. However, a lumped oscillator model is developed for the prediction of the optical constants. In the IR region, the dielectric function of an insulator is often described by the Lorentz oscillator model [78,99]:

$$\varepsilon(\nu) = \varepsilon' + i\varepsilon'' = \varepsilon_\infty + \frac{\nu_\mathrm{p}^2}{\nu_0^2 - \nu^2 - i\gamma\nu} \qquad (4.3)$$

where ε_∞ describes the high-frequency contributions, ν_p is the plasma frequency, ν_0 is the resonance frequency, and γ is the damping coefficient, all of them are in terms of wavenumber ν. It should be noted that the dielectric function is related to the complex refractive index by $\varepsilon = \tilde{n}^2 = (n + ik)^2$, where the refractive index (n) and extinction coefficient (k) are called optical constants although they are frequency interdependent.

A regression analysis is performed to match the predicted and measured radiative properties (T, R_f, and R_s). The standard error of estimate (*SEE*) defined below is used as the figure of merit in the estimation of the parameters described in Eq. (4.3):

$$SEE = \sqrt{\sum_i \frac{\left(y_{\text{cal},i} - y_{\text{mea},i}\right)^2}{N}} \tag{4.4}$$

where the subscripts "mea" and "cal" refer correspondingly to the measured data and the calculated values from the formulation for a coherent film on an incoherent substrate, using the dielectric function model given in Eq. (4.3). The simplex algorithm [100] is employed to find the best fit parameters in Eq. (4.3) that minimize *SEE* for a given set of experimental data. In the present study, the transmittance and reflectance (for incidence from both sides) spectra of HAF01 film are used in the range from 510 to 8000 cm^{-1} (the data points below 510 cm^{-1} and above 8000 cm^{-1} are removed due to low signal-to-noise ratio) to determine the parameters in the single-oscillator model as well as the film thickness. The results are $\varepsilon_\infty = 3.58$, $\nu_0 = 398\ \text{cm}^{-1}$, $\nu_\text{p} = 1049\ \text{cm}^{-1}$, and $\gamma = 147\ \text{cm}^{-1}$. Note that the oscillator parameter does not actually correspond to a vibrational band and additional oscillators are needed to capture the actual phonon spectra, which will be discussed in Sec. 4.2.4. After the oscillator parameters are determined based on HAF01 film spectra fitting, the simplex algorithm is applied to other films to find their thicknesses and results are listed in Table 4.1. The assumption is that the optical constants are independent of the film thickness, which was verified through ellipsometry and FIR studies to be discussed later. The resulting *SEE* in the radiative properties is generally less than 0.01, except for HAF04a films with a *SEE* value of 0.015. It is estimated that the (relative) uncertainty is 5 % in thickness and refractive index, and 10 % in ε_∞, ν_0, ν_p, and γ.

To illustrate the fitting agreement with experiments, the measured transmittance and film-side reflectance for HAF01 and HAF03 films are plotted in Fig. 4.5, where the wavenumber is shown in log scale. The error bars are for 0.01 in T and 0.02 in R_f. It

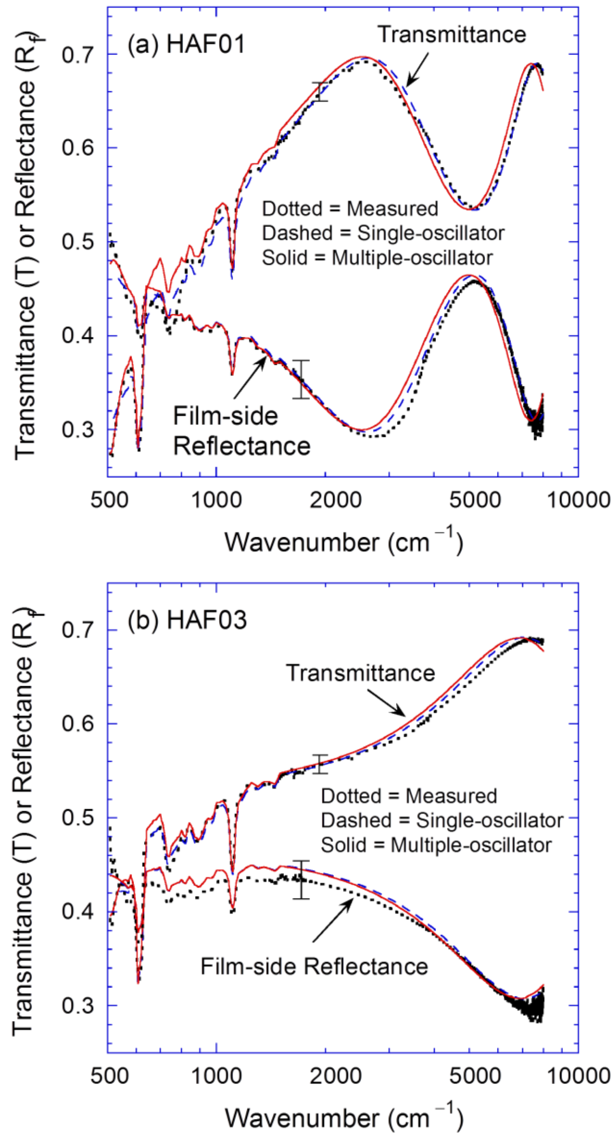

Figure 4.5 Comparison of the measured and calculated transmittance and film-side reflectance of (a) HAF01 and (b) HAF03 samples. Experimental data has an uncertainty of 0.01 in transmittance and 0.02 in reflectance. For the single-oscillator model, the dielectric function is calculated from the four-parameter model with $\varepsilon_\infty = 3.58$, $\omega_0 = 398\ \mathrm{cm}^{-1}$, $\omega_\mathrm{p} = 1049\ \mathrm{cm}^{-1}$, and $\gamma = 147\ \mathrm{cm}^{-1}$. The parameters for the multi-oscillator model are shown in Table 3.2, using the thicknesses determined from FTIR.

should be noted that the results for a multiple-oscillator model, to be elaborated in Sec. 4.2.4, are also plotted for comparison. In Fig. 4.5, the single-oscillator model refers to the dielectric function calculated from Eq. (4.3) with the fitting parameters and film thickness obtained solely based on the radiative properties of HAF01 film in this region. The agreement is very good except in the region where Si absorption is strong and in the region where absorption by moisture becomes significant.

As mentioned previously, in the region from 2800 cm^{-1} to 3700 cm^{-1}, there is an absorption feature that is not due to HfO_2 but rather the moisture or O-H bonds present in the film voids and on the film surface. This absorption feature results in a dip in the transmittance as well as film-side reflectance, especially for HAF01 film. To model moisture inside the film, the Bruggeman effective medium approximation (EMA) can be used by assuming a certain volume fraction of each material [47,101], which can be expressed as follows:

$$f_{\mathrm{A}} \frac{\varepsilon_{\mathrm{A}} - \varepsilon_{\mathrm{eff}}}{\varepsilon_{\mathrm{A}} + 2\varepsilon} + f_{\mathrm{B}} \frac{\varepsilon_{\mathrm{B}} - \varepsilon_{\mathrm{eff}}}{\varepsilon_{\mathrm{B}} + 2\varepsilon} = 0 \tag{4.5}$$

where f and ε are the volume fraction and the dielectric function, respectively, for each material, the subscripts A and B refers to component A and B (here, A is for HfO_2 and B is for H_2O, and the subscript "eff" denote the properties of the effective homogeneous medium. The optical properties of liquid water can be obtained from Refs. [102,103]. An additional regression analysis was performed with fixed film thickness as well as the dielectric functions of HfO_2 and water; however, the film's optical constants are based on $\varepsilon_{\mathrm{eff}}$ calculated from Eq. (4.5). By adjusting f_{A} and noting that $f_{\mathrm{B}} = 1 - f_{\mathrm{A}}$, a better agreement can be obtained that matches well for the radiative properties in the O-H absorption region (graphs are not shown). It is found that f_{A} ranges from 0.94 to 0.96, suggesting that the film may contain approximately 5% of moisture. Similar amount were found for Ta_2O_5 films in a previous study [47] and the O-H absorption has been discussed in detail in Ref. [30].

4.3.3 Spectroellipsometry Results

Spectroscopic ellipsometry (SE) data in Fig. 4.6 were fit using the ellipsometry equation from chapter 2. At short wavelengths, such as in the SE spectrum between 370 and 1000 nm, the surface roughness may affect the measurement. The typical method used in analysis of SE data is to assume an ultrathin layer that consists of a homogeneous

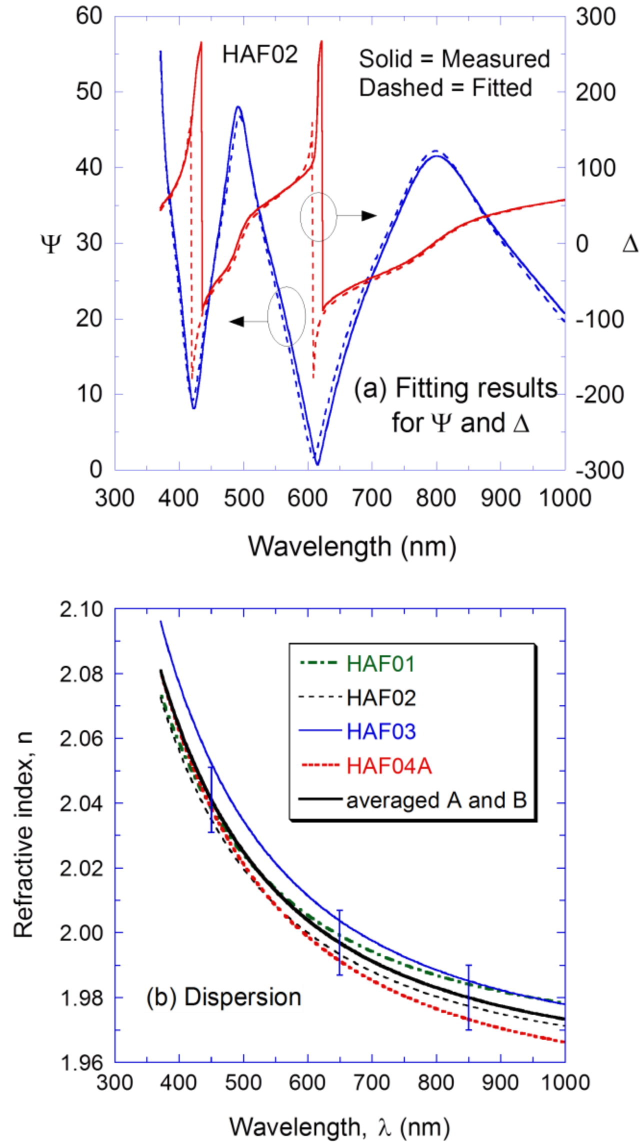

Figure 4.6 Spectroellipsometry data and fitting results: (a) measured SE parameters and fitting results for HAF02 film at 75° incidence angle; (b) Cauchy's formula of the refractive index determined with the best fit parameters listed in Table 4.1. The dispersion based on average *A* and *B* values is also plotted. Error bars indicate the standard deviations from the mean.

medium made of air and the film material. The EMA given in Eq. (4.5) can be used to model the optical constants of this layer [38,47,49]. Usually, the volume fraction is assumed to be 50% and the refractive index of air can be assumed to be $n_{air} = 1$. The thickness of this layer is called roughness σ, which is different from the RMS roughness. Hence, in the formulation of the reflection coefficient for incident on the film side, one needs to consider two layers of thin films with a roughness parameter σ and a film thickness d_f. Fortunately in this region, the Si substrate is opaque and can be treated as a semi-infinite medium. The standard matrix formulation for multilayered thin films can be applied to calculate the reflection coefficients for each polarization [35,47]. An attempt to include SiO_2 thin layer in the analysis of the SE data were made but did not result in improved agreement, suggesting that the effect native oxide layer is negligibly small.

The four-layer model (air, roughness, film, and substrate) is used in the CompleteEASE software accompanied with the SE. The software uses a figure of merit according to the mean square error based on chi-square test [104,105]. It is an unbiased estimator that gives data points with larger standard deviation lower weight. In order to obtain reliable fitting, the SE measurements were taken at four incidence angles with 60º, 65º, 70º, and 75º. The typical fitting result for quantities Ψ and Δ is illustrated in Fig. 4.6(a). The obtained parameters A and B, roughness, and thickness for all samples are listed in Table 4.1. Figure 4.6(b) plots the refractive index as a function of wavelength in the VIS/NIR region. The average values of A and B from all four samples are computed and the resulting dispersion is also shown in Fig. 4.6(b). It can be seen that within experimental uncertainty, the optical constants are the same for all four samples. The agreement in these values gives a reliable dispersion at short wavelength. When the refractive index is calculated at $\lambda = 1$ μm using Eq. (4.3) using the fitting parameters in NIR/MIR, it gives $n = 1.89$, which is 4% less than the value of 1.97 obtained from SE.

As shown in Table 4.1, the agreement in film thickness from FTIR and SE is 3.6% for HAF01 film, 2.0% for HAF02 film, and increases to around 10% for HAF03

and HAF04a films. The thinnest films may result in a relatively large uncertainty in both methods. Furthermore, if (σ + d_f) is taken as the film thickness from SE, then the agreement with FTIR thickness will be around 1% for HAF01 and HAF02 films, and better than 6% for the two thinnest samples. The good agreement between two independent method suggest that either one can be used with confidence. The high refractive index and low absorption in the VIS/NIR region, along with the small grain size, suggest that the quality of the HfO_2 film is high.

Interestingly, the roughness σ obtained from SE also increases with the film thickness, similar to the trend shown with AFM measurements. However, the σ value from SE is about two times that from AFM for all samples. Koh et al. [106] studied the correlation of the RMS roughness from AFM and the roughness from SE and found a factor of about 1.5 for amorphous semiconductors. On the other hand, the SE roughness obtained by Franke et al. [47] is 3-4 times that from AFM for Ta_2O_5 films. It can be inferred that the roughness values obtained from this study are reliable and consistent with the method used.

4.2.4 Far-infrared Spectroscopy and Multiple-oscillator Model

The ratio of transmittance of the sample to that of the Si substrate measured with the vacuum spectrometer is plotted in Fig. 4.7(a) from 20 to 650 cm^{-1}. Several lattice absorption bands show up and the transmittance decreases as the film thickness increases. Again, the transmittance is almost the same for HAF03 and HAF04a films, suggesting that annealing has essentially no effect on the phonon modes. Interference effects inside Si substrate are noticeable below 100 cm^{-1} as well as above 550 cm^{-1} where absorption is weak. The wavenumber corresponding to the minima of transmittance agree with the phonon absorption spectra of HfO_2 in previous studies [30,35]. The transmittance minima are located at 260, 340, 405, 510, and 600 cm^{-1}. Some weak phonon modes may exist between 380 and 400 cm^{-1} but is not considered in the modeling. Another oscillator may

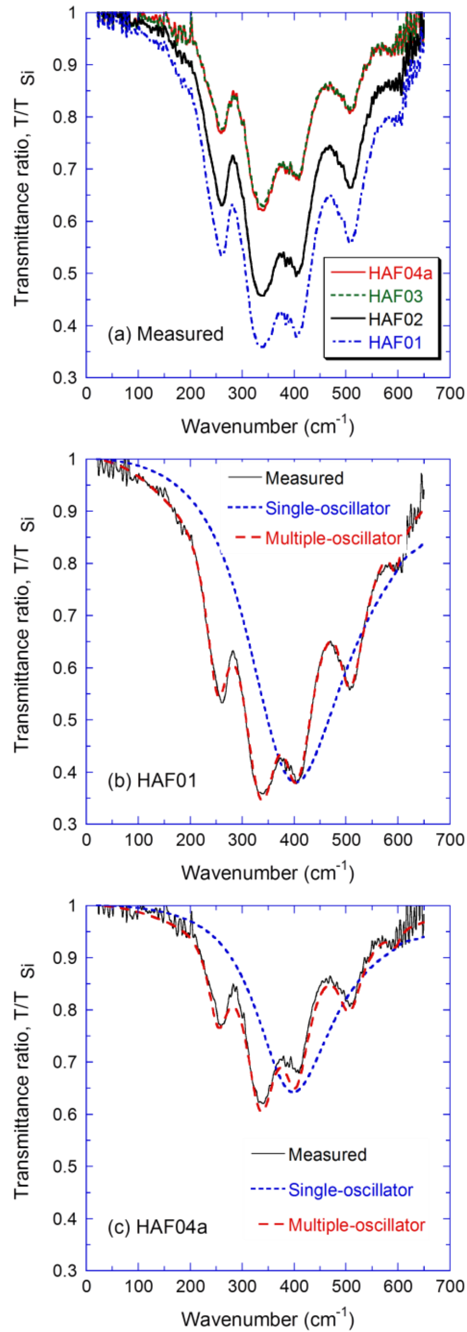

Figure 4.7 Comparison of the measured and calculated transmittance and film-side reflectance of (a) HAF01 and (b) HAF03 samples. Experimental data has an uncertainty of 0.01 in transmittance and 0.02 in reflectance. For the single-oscillator model, the dielectric function is calculated from the four-parameter model with $\varepsilon_\infty = 3.58$, $\omega_0 = 398\ \text{cm}^{-1}$, $\omega_p = 1049\ \text{cm}^{-1}$, and $\gamma = 147\ \text{cm}^{-1}$. The parameters for the multi-oscillator model are shown in Table 4.2, using the thicknesses determined from FTIR.

be assigned on the shoulder near 190 cm^{-1} in order to fit the FIR spectrum. Hence six oscillators are needed to fit the FIR spectrum, in addition to a high-frequency constant.

In order to develop a broadband dielectric function model to cover from the visible all the way to the FIR spectral region, the Cauchy formula is incorporated to the multiple Lorentz oscillator model with

$$\varepsilon(\nu) = A^2 + C\nu^2 + \sum_j \frac{\nu_{\text{p},j}^2}{\nu_j^2 - \nu^2 - i\gamma_j \nu} \tag{4.6}$$

where the first two terms are calculated from the Cauchy formula after omitting the fourth-power term, which makes negligible contribution. Therefore, A = 1.956 is fixed according to the average of the fitted values from the ellipsometry data, and $C = 0.5, B = 6.73\times10^{-10}$ cm^2 (since ν is in cm^{-1}). Note that ν_j, $\nu_{\text{p},j}$, and γ_j are the resonance frequency, plasma frequency, and damping coefficient of the *j*th phonon oscillator. The simplex algorithm is used to minimize the *SEE* for HAF01 film in the region from 20 to 650 cm^{-1} based on the transmittance ratio measured with the FIR spectrometer.

Table 4.2 lists the fitted phonon oscillator parameters and the resonance frequencies are close to the transmittance minimum. The *SEE* with the best fitting parameters is 0.013, which is comparable to the measurement uncertainty in the FIR spectrometer. The fitted results are compared with the measured in Figs. 4.7(b) for HAF01 and 4.7(c) for HAF04a using the thickness obtained from NIR/MIR spectrometer. The calculated transmittance ratio from the single-oscillator model is also plotted for comparison. It can be seen that the simplified model cannot capture the phonon frequencies but does give a broad absorption band that is slightly shifted toward large wavenumbers. It is expected that the parameters in the multiple-oscillator model have a smaller uncertainty that those for the single-parameter model, because the fit directly

against the phonon resonances. The uncertainties are therefore estimated to be about 2% in ν_j and 5% in $\nu_{p,j}$ and γ.

Furthermore, as shown in Fig. 4.5, the multiple-oscillator model can be used to predict the radiative properties in the NIR/MIR regions as well. Due to the fixed value of A from the ellipsometry and fixed thickness from FTIR, the agreement of experiments with the multiple-oscillator model is not as good as that with the single-oscillator model. A better agreement can be obtained by reducing the film thickness by 4%. Another feature is that the multiple-oscillator model seems to over predict the transmittance between 650 and 800 cm^{-1}; this is probably due to limited spectral region of the FIR data. Because of the incorporation of the Cauchy dispersion in the Lorentz oscillator model and the negligible contributions of the oscillators in the VIS/NIR spectrum, Eq. (4.6) gives the refractive index from 370 to 1000 nm essentially the same as Eq. (2.12). In the region up to λ = 1500 nm, this dispersion is still valid. Therefore, the expression given in Eq. (4.6), with parameters specified in Table 4.2, gives a broadband dielectric function model of HfO_2 films for 370 nm $\le \lambda \le$ 500 μm,

Table 4.2 Far-infrared phonon parameters obtained by fitting the Lorentz model with the far-IR absorption spectrum of HAF01 using d= 516 nm. The fitting parameters obtained from the Cauchy formula are $A = 1.956$ and $C = 6.73\times10^{-10}$ cm^2 (based on $B = 0.0172$ μm^2).

Phonon number	ω_j (cm^{-1})	ω_{pj} (cm^{-1})	γ_j (cm^{-1})
1	187.3	247.1	215.9
2	254.9	373.1	45.1
3	336.9	683.3	62.4
4	402.9	537.8	56.6
5	506.0	371.1	54.1
6	594.8	118.4	26.2

4.3 Dielectric Function and Optical Constants

The real part (ε') and imaginary part (ε'') of the dielectric function are plotted in Figs. 4.8(a) and (b), respectively, using the single-oscillator and multiple-oscillator models described previously. The FIR phonon contributions are shown as five peaks in ε'' in addition to the rapid change of the slope near 200 cm^{-1}. This is because of the large damping coefficient for this phonon. As expected, the single oscillator model gives a broad absorption band as evidenced by the broad peak in ε'' centered around 400 cm^{-1} with a large damping coefficient, which corresponds to the width of the peak in ε'' [99]. Note that ε'' is somewhat smaller with the multiple-oscillator model than with the single-oscillator model between 600 and 800 cm^{-1}, which may be the reason for the over prediction of the transmittance by the multiple-oscillator model. Beyond 1200 cm^{-1}, absorption becomes very weak and ε' is very similar between the two models, except the different constant and the additional dispersion resulting from the second term in the multiple-oscillator model.

The optical constants are calculated from Eq. (4.6) and plotted in Fig. 4.9 for the wavenumber range from 20 to 26000 cm^{-1}, i.e., over three orders of magnitude. It can be seen along with the Fig. 4.8(a) that the dielectric constant in the low frequency region approaches 14, which is somewhat smaller than the measured value of 22-25 at 1 MHz [25,107]. The reason for this disagreement needs further investigation. In the NIR/VIS region, n is near 2 and increase slightly with ν, in agreement with Fig. 4.6(b) which is plotted in terms of wavelength.

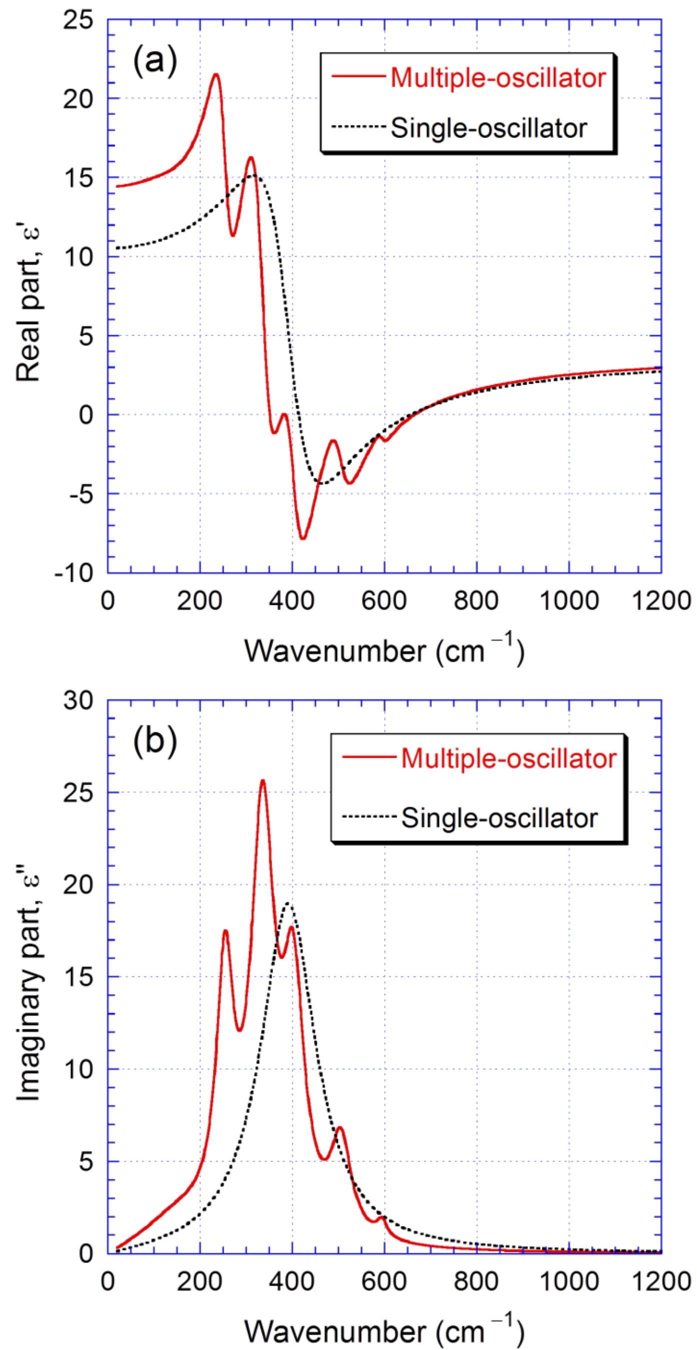

Figure 4.8 MIR and FIR dielectric functions of HfO_2 calculated from both the single oscillator and multiple oscillator models: (a) real part; (b) imaginary part.

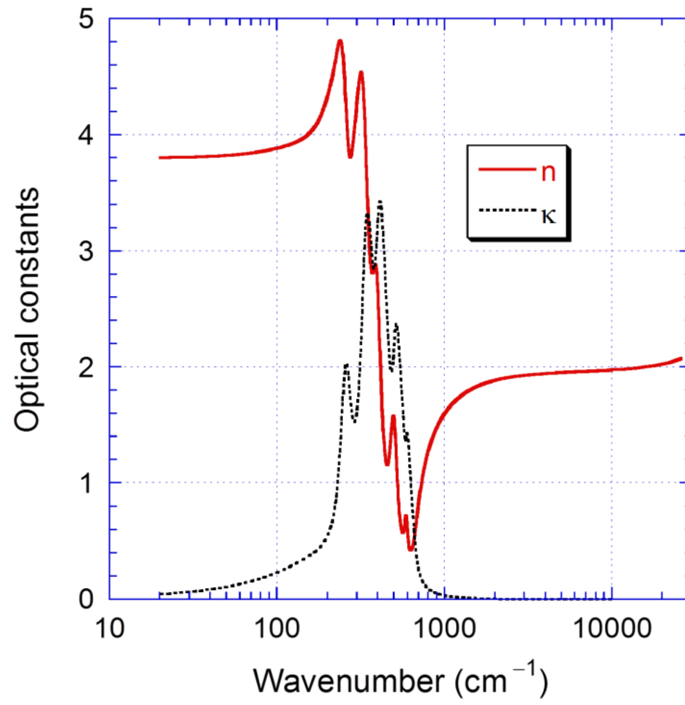

Figure 4.9 Optical constants of HfO_2 calculated from the multiple-oscillator model, in a broad spectral region from 20 to 26000 cm^{-1}. The wavenumber is plotted in log scale.

CHAPTER 5

DIELECTRIC FUNCTION OF MAGNETRON SPUTTERED TA_2O_5 THIN FILMS

In this chapter, the dielectric functions of amorphous and nanocrystalline Ta_2O_5 films are determined, at wavenumbers from 10 to 20,000 cm^{-1}, by analyzing ellipsometric measurements in the visible and near-IR regions and by fitting the transmittance and reflectance measured with Fourier-transform infrared (FTIR) spectrometers from the near- to far-IR regions. Thin Ta_2O_5 films are deposited on Si substrates using reactive magnetron sputtering. The phase and structure of the as-deposited and annealed samples are also characterized. The location and strength of individual phonon bands are determined in the mid- and far-infrared regions. The effect of cracking in the annealed films is considered using a volume-scattering model. The effects of free carriers and adsorbed water moisture in the amorphous films are also considered in the development of the dielectric function model.

5.1. Film Characterization

A magnetron sputtering system described in chapter 4 and in Ref. [95] was used to deposit thin Ta_2O_5 films on Si substrates. The deposition conditions were the same with the exception of the substrate temperature, which was 100 °C. Detailed parameters of the six samples used for the present study are listed in Table 5.1. Two of them were left as-deposited and the rest were annealed in air at 800 °C for one hour. The deposition parameters such as gas flow rates and substrate temperature were chosen according to the literature [108–113] in order to obtain high-quality Ta_2O_5 films. It should be noted that

Table 5.1 Sample identification (ID) and parameters. In the sample ID, the last letter "u" indicates that it was unannealed (or as-deposited) and "a" indicates that it was annealed at 800 ºC in air for one hour. The unannealed Ta_2O_5 samples TaO-1u and TaO-2u are amorphous. The annealed four samples are nanocrystalline Ta_2O_5. The RMS roughness of the film is obtained from AFM.

Sample ID	Substrate thickness (μm)	RMS roughness (nm)	Film thickness (Ellipsometry) (nm)	Film thickness (FTIR) (nm)
TaO-1u	432	4.1	1588	1589
TaO-2u	432	2.6	492	506
TaO-3a	432	14.5	1017	1035
TaO-4a	432	20.4	462	478
TaO-5a	750	3.6	347	353
TaO-6a	750	3.3	174	179

the far-IR measurements were not performed for the last two samples listed in Table 5.1, which had the thicker Si substrates. The same XRD and AFM described in the previous chapter were also used to characterize the film structures.

A test film was annealed at various temperatures in air. Annealing in air at 800 °C for one hour yielded well-defined XRD patterns; therefore, all the annealed samples were treated under the same annealing condition. Figure 5.1 shows the XRD profile for TaO-3a that matches well with the orthorhombic β-phase (JCPDS: 25-0922), although some closely spaced peaks appear to be merged due to broadening [39,114,115]. The prominent peak in the (001) plane suggests anisotropic crystalline orientation due to the stress effect. Similar results were obtained for other annealed samples, but are not shown. It should be noted that there exists a hexagonal δ-phase of Ta_2O_5 (JCPDS: 19-1299) that has a diffraction pattern nearly overlapping that of the β-phase Ta_2O_5 [39,40]. Both of these crystal phases are reported to occur in the literature at annealing temperatures close

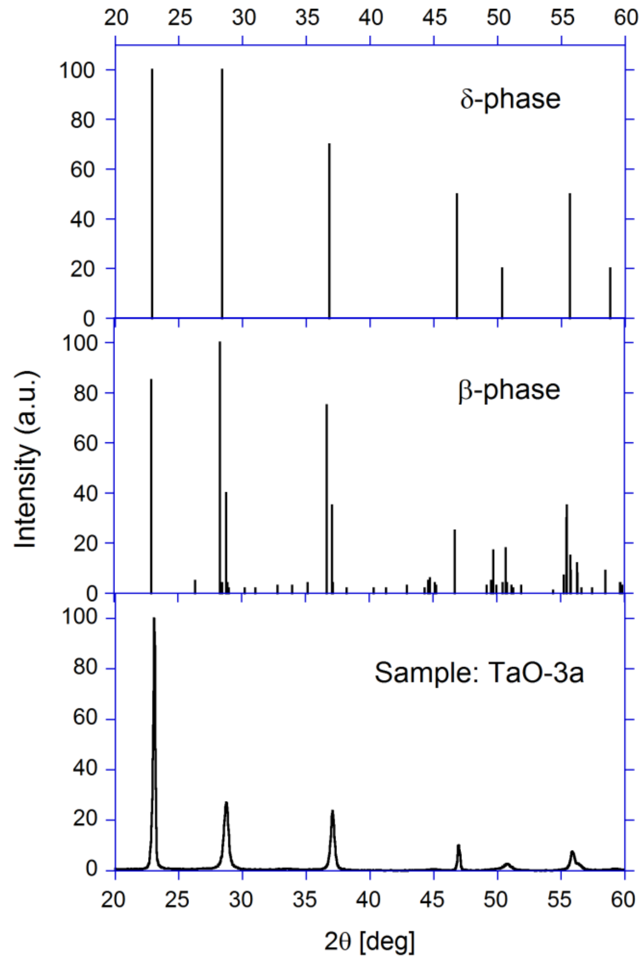

Figure 5.1 X-ray diffraction profile of an annealed Ta_2O_5, sample TaO-3a, also shown are the pdf files for δ-Ta_2O_5 and β-Ta_2O_5. Other annealed samples show nearly identical XRD profiles. Note that the as-deposited samples do not show any peaks in their XRD profiles, which are therefore not shown here.

to that used in the present study [11,39,40,114,115]. Hence, it is possible that both phases exist in the annealed films. The identification of the β-phase is confirmed by the broadness of the peaks and the existence of several minor peaks in the XRD pattern. Therefore, it is presumed that the annealed samples are primarily orthorhombic β-phase. The XRD peak associated with (001) plane in Fig. 5.1 is used to estimate the crystalline size, which is about 40 nm, according to Scherrer's formula [116]. Hence the annealed films are identified as containing nanocrystalline Ta_2O_5. Note that the peaks at $2\theta = 29°$

and 37° are broadened due to the merging of multiple diffraction orders. The unannealed or as-deposited samples are amorphous as there are no distinct peaks in the XRD profiles, which are not shown here. To verify the composition of the fabricated films, X-ray photoelectron spectroscopy (XPS) was performed for an annealed and an unannealed sample after all the spectroscopic measurements. The samples were heated to 200 °C in ultrahigh vacuum to remove surface water. The analysis of the XPS of the Ta 4f peak reveals close to stoichiometric Ta_2O_5 in both the annealed and unannealed samples.

The AFM topography of two samples is shown in Fig. 5.2. The unannealed sample TaO-2u, shown in Fig. 5.2(a), does not contain any cracks. The presence of

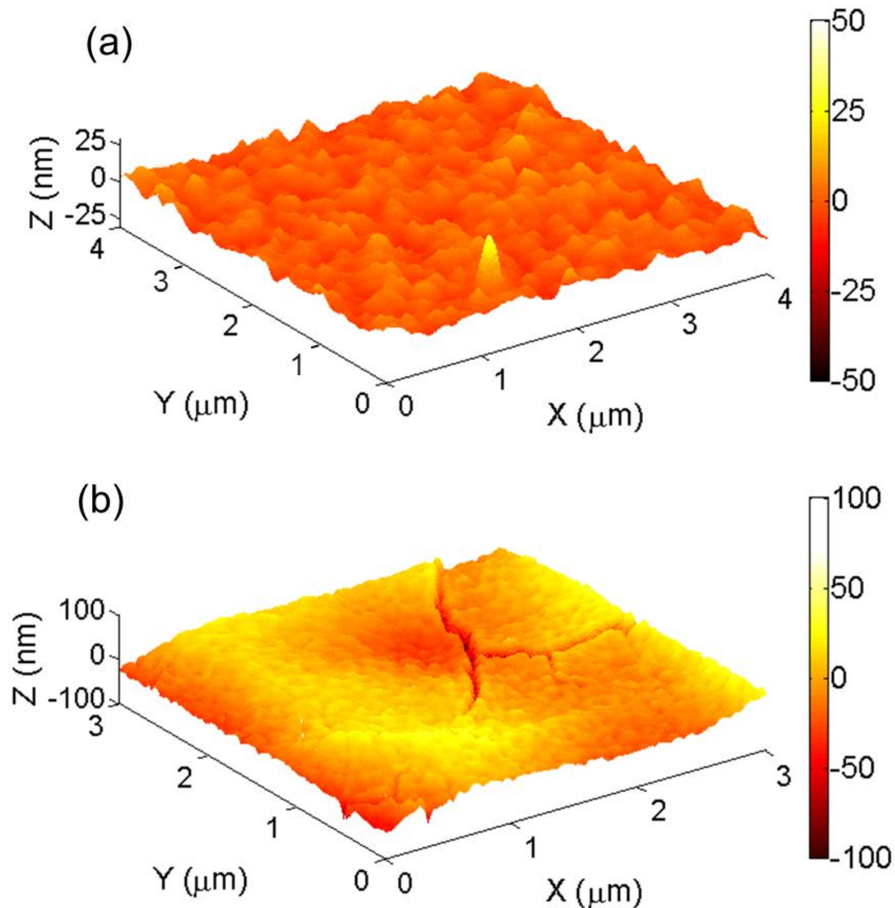

Figure 5.2 AFM topographies of (a) sample TaO-2u and (b) sample TaO-3a.

cracks can clearly be seen in Fig. 5.2(b) for the annealed sample TaO-3a. As can be seen from the AFM images and Table 5.1, the cracks have increased the root-mean-square (RMS) roughness that significantly exceeds the actual local surface roughness. Similar cracks in annealed Ta_2O_5 films have been reported by other researchers [40]. The crack development is mainly due to the considerable mismatch between the thermal expansion coefficients of Ta_2O_5 (4.68×10^{-6} K^{-1}) and the Si substrate (1.10×10^{-6} K^{-1}). The mismatch was reported in the literature as the main contributor to both stress and refractive index variation for the Ta_2O_5 films [117]. The compressive stress develops as the sample is heated to the annealing temperature, while the tensile stress develops during the sample cooling. For the two thinnest films, samples TaO-5a and TaO-6a, the stress may not be significant enough and hence the RMS roughness is on the same order of that of the amorphous films.

In addition, images of the surfaces were taken with an Olympus LEXT 3D Material Confocal Microscope over a larger surface area of 43×43 μm^2. Two microscope images are displayed in Fig. 5.3. Figure 5.3(a) shows the unannealed sample, TaO-2u, which has a much smoother surface and no cracking. Figure 5.3(b) shows the surface of an annealed sample TaO-3a. The scaly appearance is due to cracking that occurs during annealing. Cross-sectional images of two films were also taken using scanning electron microscopy (SEM) at an inclined angle of approximately 45° to study their microstructure, as shown in Fig. 5.4. The unannealed sample TaO-1u, shown in Fig. 5.4(a), does not display significant cracking or roughness. It can be seen in Fig. 5.4(b) that the annealed sample TaO-4a contains cracks that penetrate through the film. These cracks contribute to volumetric scattering and optical losses in the sample and need to be included in the modeling of the radiative properties that will be discussed in the following section.

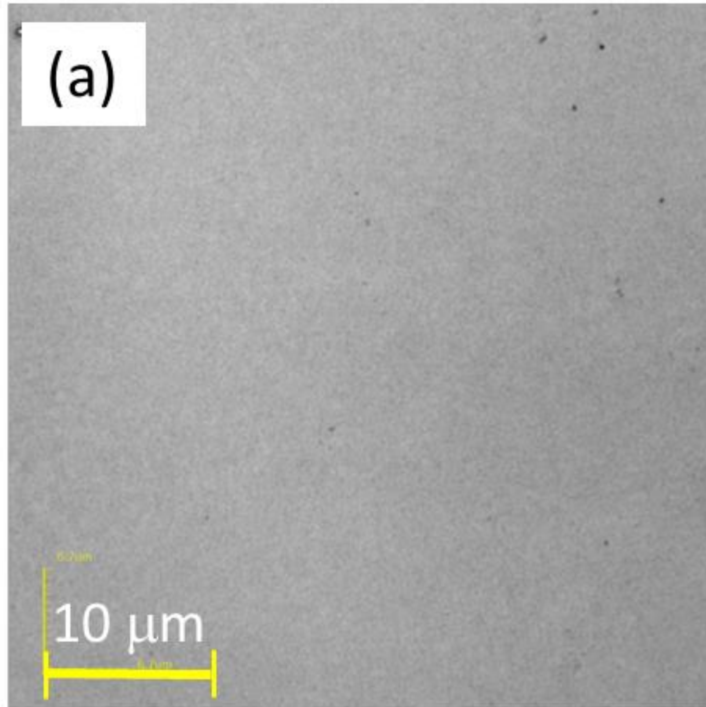

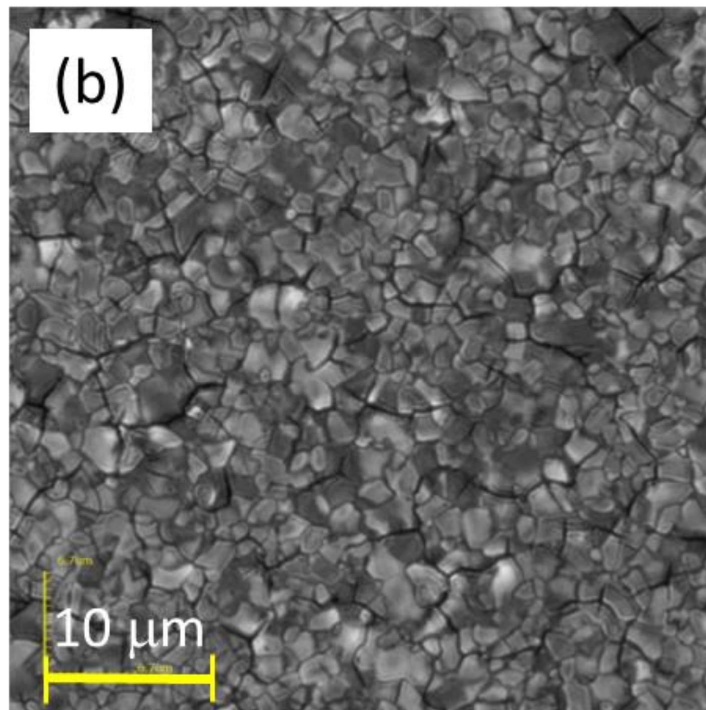

Figure 5.3 Confocal microscope images of (a) sample TaO-2u and (b) sample TaO-3a.

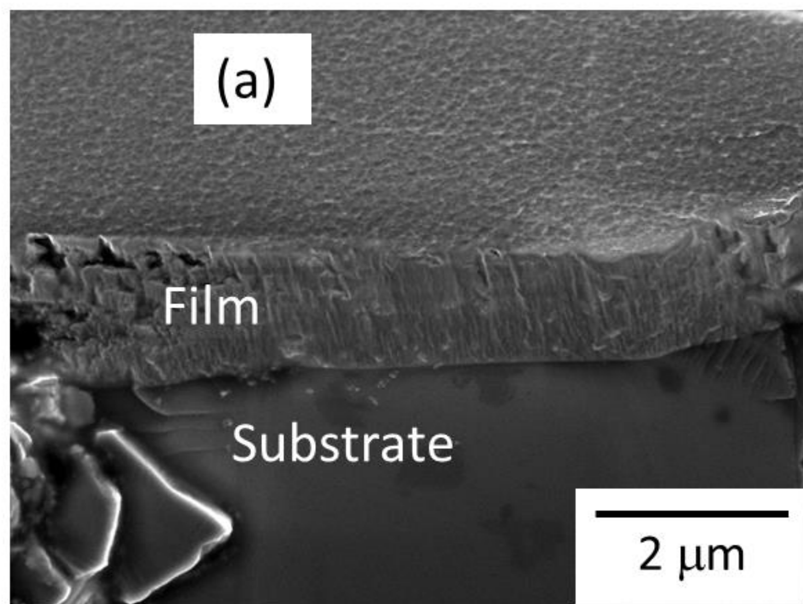

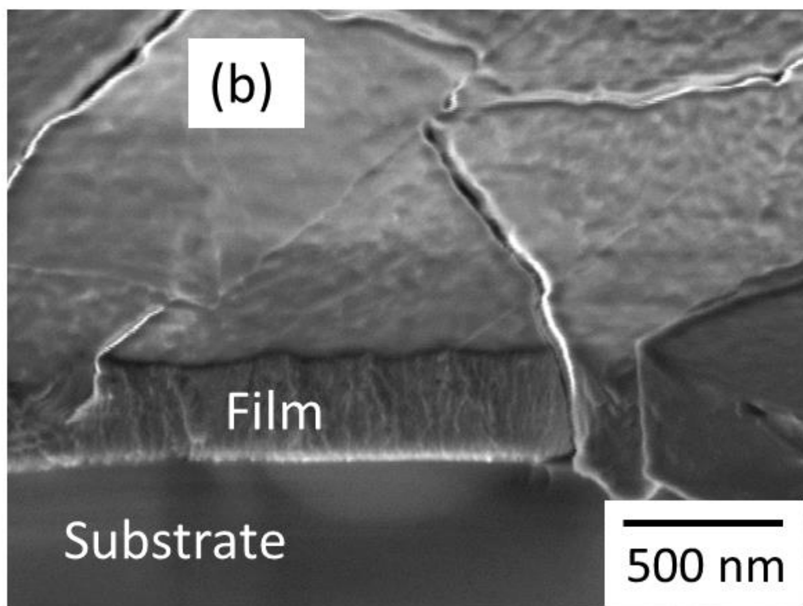

Figure 5.4 SEM cross section images of (a) sample TaO-1u and (b) sample TaO-4a.

5.2 Film Analysis

5.2.1 Dielectric Function Model

The optical constants of the Ta_2O_5 films are determined by the line-shape analysis using the description of the dielectric function given as [78]

$$\varepsilon(\nu) = A^2 + C\nu^2 + \sum_j \frac{\nu_{\mathrm{p},j}^2}{\nu_j^2 - \nu^2 - i\gamma_j \nu} \tag{5.1}$$

Usually, the first term on the right hand side of Eq. (1) is taken as a constant to reflect high-frequency contributions. In the present study, ε_∞ is calculated from the refractive index following the Cauchy dispersion:

$$n(\lambda) = \sqrt{\varepsilon_\infty} = A + \frac{B}{\lambda^2} \tag{5.2}$$

where λ is the wavelength in vacuum and constants A and B can be obtained from ellipsometry data [95]. Note that band gap absorption is not considered since the band gaps of Ta_2O_5 are greater than 4 eV [41,48]. This treatment allows Eq. (5.1) to represent the dielectric function from $\lambda = 500\ \mathrm{nm}$ all the way to the far-IR. The second term is a Drude free-electron term, which is included only for the unannealed samples due to the residual broadband absorption. The Drude term contains two adjustable parameters, namely, the plasma frequency $\omega_{\mathrm{p},0}$ and scattering rate γ_0. The third term in Eq. (5.1) is the sum of *N* Lorentz oscillators, which correspond to the phonon absorption bands in the far-IR region. Each individual oscillator *j* has a center frequency ω_j, a plasma frequency $\omega_{\mathrm{p},j}$, and a damping coefficient γ_j. Due to the practical limitations caused by the uncertainty in the data, the oscillators in the model may not correspond to all of the infrared-active phonon modes present in the material, especially if modes are very close in frequency or very weak. Stronger and broader phonon bands may mask some weaker phonon modes. The phonon modes can be predicted by *ab initio* simulation according to

the crystalline structure for similar materials [118]; however, not all of the modes may manifest in experimental measurements [49]. In addition, defect modes may arise from impurities present in the films [47,48]. Note that impurity modes are not distinguished from the actual phonon modes of Ta_2O_5 in the experimentally determined dielectric function. Thus, the oscillators obtained by fitting the IR spectra should be considered as effective phonon modes and represent the overall lattice vibration contributions. The dielectric function model does however provide an accurate description of the optical properties of the material in a broad spectral region and captures well the behavior of major phonon resonances.

The unannealed samples also have absorption band around the wavenumber of 3400 cm^{-1}, which is characteristic of moisture absorption [47]. In order to account for the existence of moisture in the unannealed samples, the Bruggeman effective medium approximation (EMA), described in Eq. (4.5) in the previous chapter, is used to determine the effective dielectric function of the film, ε_{eff}, assuming that a small amount of water is randomly dispersed in Ta_2O_5 [47,119]. The dielectric function of material A in Eq. (4.5) is of course that of Ta_2O_5 rather than HfO_2. The value of ε_{eff} is taken as the dielectric function of the moist Ta_2O_5 film, and is used to calculate the radiative properties of the film-substrate composite.

5.2.1 Scattering Model

For the annealed samples with cracks, the transmittance and the film-side reflectance of the FTIR data exhibit some attenuation towards the near-IR end of the spectra. Attempts were initially made to include a surface roughness term according to the scalar scattering theory [78,93]. The predicted results also showed an attenuation in the substrate-side reflectance that contradicts with the experimental observation. In addition, when the ellipsometry data were analyzed, accounting for roughness did not improve the fitting. Therefore, the cracking effect cannot be well described by surface

scattering. A careful examination of Eqs. (3.1) – (3.3) reveals that τ_{a} is the only term that appears in T and R_{f} but not R_{s}. A volumetric scattering model is considered in the final analysis to better model the observed trends due to cracking of the thick annealed samples, i.e., TaO-3a and TaO-4a. It is assumed that scattering results in a reduction only in the transmission through the film, and the attenuation is wavelength dependent according to

$$\tau_{\mathrm{a}}' = \tau_{\mathrm{a}} \left(1 - \frac{S_{\mathrm{f}}^4}{\lambda^4} \right) \tag{5.3}$$

Here, S_{f} is a fitting parameter that is related to the scattering cross-sectional area and the defect density, assuming independent scattering by small particles that follow Rayleigh scattering [93,120]. When τ_{a} in Eqs. (3.1) and (3.2) are substituted by τ_{a}' from Eq. (5.3), both the transmittance and reflectance of the film side of the sample are reduced, while the substrate-side reflectance given in Eq. (3.3) is unaffected. This gives a reasonable interpretation of the experimental results to be discussed in the next section. It should be noted that volume scattering may also arise due to relatively large grains in the film. Hence, S_{f} may be considered as an effective lump sum of the volume scattering contribution.

The predicted radiative properties are fitted to the measured FTIR transmittance spectra using a simplex optimization algorithm that minimizes the standard error of estimate (SEE) [100,121]. It is assumed that ε_{∞} is the same as the average value obtained for either the unannealed or annealed samples from the ellipsometry data according to Eq. (5.2). The film thickness is related to the interference fringes and determined by fitting the FTIR data in the near- to mid-IR region. The obtained thickness is then used to fit the parameters in Eqs. (5.1) and (5.3) using far-IR transmittance.

The transmittance data agree well in the overlapping region between the purged FTIR and the vacuum far-IR spectrometer results. The reflectance measurement by the

far-IR spectrometer is more reliable and allows the identification of some offset in the mid-IR measurements in some samples. The measured reflectance spectra are used to check the reasonableness of the model predictions. the classical Lorentz oscillator model discussed in the next section.

5.3 Dielectric Function and Optical Constants

5.3.1 Ellipsometric Results

The optical constants at wavelengths from 500 to 1000 nm are determined from the ellipsometry data. Each sample was fit individually to obtain the parameters *A* and *B* in the Cauchy dispersion, Eq. (5.2), and the film thickness. The absorption is neglected because the interband transitions occur at photon energies greater than 4 eV [41,47,48]. The resulting *A* and *B* values change little from sample to sample; therefore, only the averages of all *A* and *B* values for the two unannealed samples and those for the annealed samples are reported here. For the unannealed samples the average *A* and *B* are 2.06 and 0.025 μm^2, respectively. For the annealed samples the average values of *A* and *B* are 2.10 and 0.024 μm^2, respectively. All of the uncertainties in *A* and *B* are less than 0.02 and 0.001 μm^2, respectively. Table 5.1 shows the thickness obtained from fitting the ellipsometry data with the Cauchy model. The agreement between the ellipsometry data and the model is very good for the unannealed samples as well as for the thinnest annealed samples. The average mean squared error (MSE) for the two annealed samples TaO-3a and TaO-4a with cracks is about five times larger than the rest. However, the coefficients *A* and *B* are all very close. The resulting refractive indices of n = 2.16 and 2.20 for unannealed and annealed Ta_2O_5 films, respectively, agree with the typical values reported in the literature at $\lambda = 500$ nm [6,43–45,47].

5.3.2 Comparison of the Measured and Calculated Radiative Properties

While ε_∞ in Eq. (5.1) can be fitted using the FTIR data, for consistency, it is taken instead from the Cauchy dispersion from Eq. (5.2) based on ellipsometry measurements. The film thickness is also fitted using near- and mid-IR transmittances, which are sensitive to the film thickness due to the interference effect. Despite the existence of cracking, the film thicknesses obtained from the ellipsometry are quite consistent with those from the FTIR measurements as shown in Table 5.1. The far-IR transmittance is used to fit the phonon oscillator parameters and the results are listed in Table 5.2. For the unannealed samples, the transmittance measured by FTIR is compared to the best fit curves as shown in Fig. 5.5. The agreement is generally satisfactory throughout the concerned spectral region. The dips in the far-IR transmission shown in Fig. 5.5(a) are due to interaction of light with phonon vibration modes in Ta_2O_5. Each of these dips is represented by an oscillator in the dielectric model. Some of the dips may also be caused by the Si substrate especially around 610 cm^{-1}, where there is a dip due to Si absorption. Due to the uncertainty of the data very weak phonon features are difficult to resolve.

The Drude term results in broad absorption and the plasma frequency and scattering rate are found to be $\omega_{p,0} = 6490\ cm^{-1}$ and $\gamma_0 = 6.5\times10^5\ cm^{-1}$ from the fitting. This extreme broadness can be attributed to the fact that the samples are amorphous and thus have a very large electron scattering rate. Based on the Drude parameters, the resistivity of the sample can be estimated to be 0.9 Ω·cm, which would be typical of a lightly doped material. The existence of free electrons in the unannealed samples is presumably due to a slight oxygen deficiency or sub-stoichiometry during the growth process, although other possibilities also exist [11,14,46]. According to Kulisch et al. [122], suboxides of Ta can contribute to a broadband absorption around $900\ cm^{-1}$, which is evident from Fig. 5.5(a). However, the XPS analysis does not show any apparent

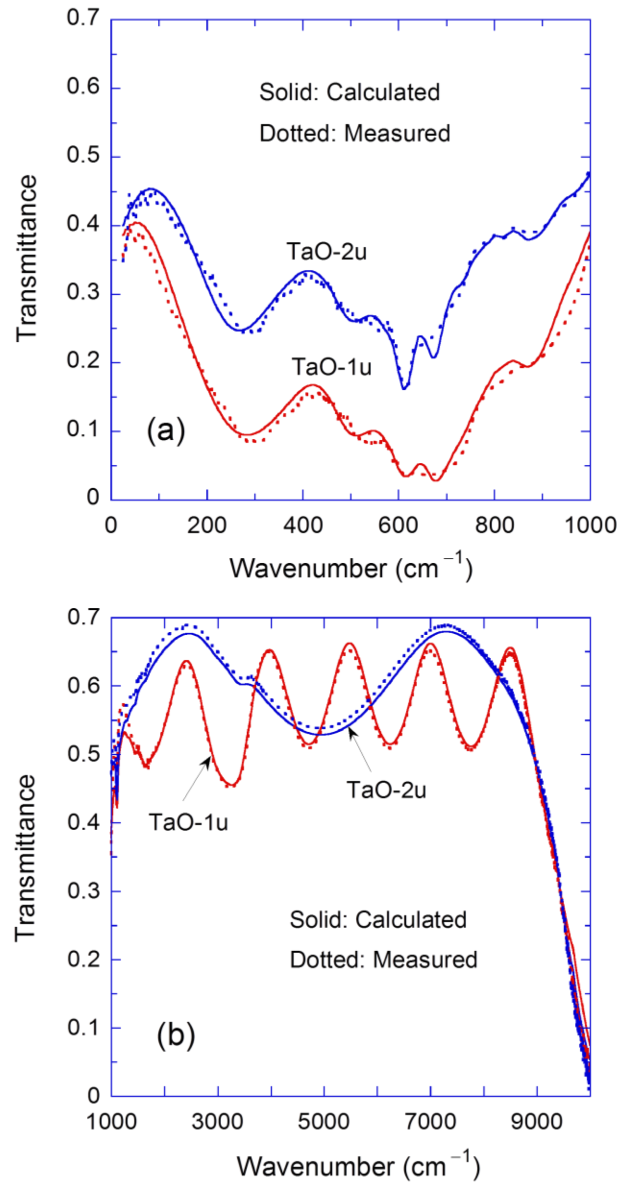

Figure 5.5 Transmittance of samples TaO-1u and TaO-2u: (a) far-IR region from 10 to 1000 cm^{-1}; (b) mid-IR region from 1000 to 10,000 cm^{-1}.

suboxides of Ta in both the annealed and unannealed samples, suggesting that the oxygen deficiency is insignificant (see Appendix A for details).

The presence of moisture in the film is apparent from the dip in the transmittance around 3400 cm^{-1}. It is found using the EMA analysis from Eq. (4.5) that a volume fraction of water of 5% works best to model the moisture contribution to the dielectric

function. The addition of water matches the dip well at 3400 cm^{-1}, but is not broad enough to match the valley in transmittance. Therefore, another weak oscillator is added around 3000 cm^{-1} to the dielectric function model (j = 6 in Table 5.2). This results in satisfactory agreement between the model prediction and the transmittance in the mid-IR region as shown in Fig. 5.5(b).

The thicker film sample, TaO-1u, exhibits more interference fringes than the thinner film sample, TaO-2u. The free spectral range or wavenumber interval between the interference maxima can be approximated by $1/(2nd)$, where d is the film thickness. Due to absorption around 3000 cm^{-1}, the transmission of the thicker sample drops quite a bit in this region. It should be noted that the minimum transmittance can be estimated from the refractive indices of the film and substrate if absorption is negligible [95]. The introduction of the Drude term is necessary to predict the broadband absorption, allowing the prediction to match the data at the transmittance minima at 4700, 6250, and 7800

Table 5.2 Parameters for the Lorentz oscillators. Note that the parameters that determine ε_∞ from the ellipsometric measurements are (A = 2.06, B = 0.025 μm^2 for amorphous Ta_2O_5; A = 2.10, B = 0.024 μm^2 for nanocrystalline Ta_2O_5).

	Amorphous			Nanocrystalline		
j	ω_j (cm^{-1})	$\omega_{p,j}$ (cm^{-1})	γ_j (cm^{-1})	ω_j (cm^{-1})	$\omega_{p,j}$ (cm^{-1})	γ_j (cm^{-1})
1	266	1040	188	91	260	74
2	500	573	112	214	844	61
3	609	634	88	324	391	73
4	672	408	43	530	1019	142
5	868	277	113	842	372	114
6	3020	373	652			

cm^{-1}. Note that the drop in transmittance close to 10000 cm^{-1} is caused by the absorption of the substrate associated with the indirect band gap of Si near 1.1 eV.

The transmittance for two of the annealed samples is shown in Fig. 5.6. There is no need to include the Drude term in the dielectric function model, since the samples were annealed in air: the reaction with oxygen during the annealing process apparently

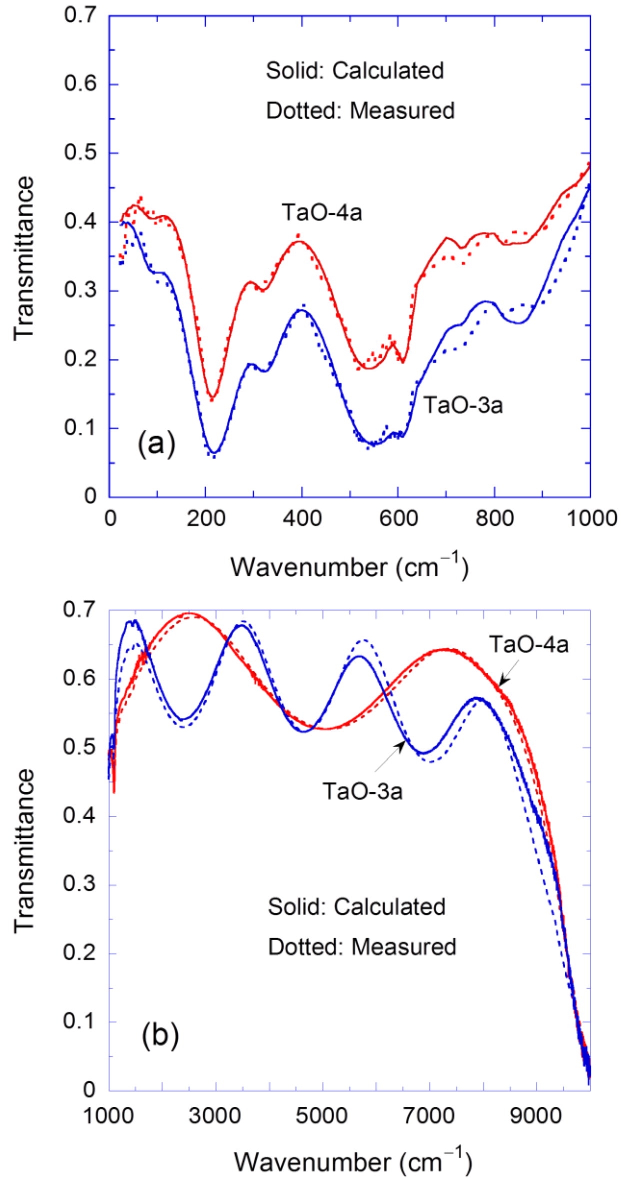

Figure 5.6 Transmittance of samples TaO-3a and TaO-4a: (a) far-IR region from 10 to 1000 cm^{-1}; (b) mid-IR region from 1000 to 10,000 cm^{-1}.

has improved the stoichiometry. The annealing has removed the absorbed moisture as well. After annealing, the low frequency phonon mode at 266 cm^{-1} shifts to the lower frequencies at 214 cm^{-1} and becomes narrow due to a reduction in the damping coefficient as shown in Table 5.2. This absorption band becomes much narrower and deeper as shown in Fig. 5.6(a). Another phonon mode is needed to model the small dip around 90 cm^{-1}. From Fig. 5.6(b), it is evident that there exists a gradual reduction in the transmittance from 3000 to 10,000 cm^{-1} and this reduction is attributed to light scattering due to cracks or grain boundaries inside of the films. The scattering factor S_f for samples TaO-3a and TaO-4a is determined to be 5.3 and 5.1 nm, respectively.

Only the two thicker samples require the addition of volume scattering into the modeling, since cracking was not as significant in the two thinner samples. As shown in Fig. 5.7, the transmittance calculated for TaO-5a and TaO-6a using the dielectric function model determined for the two thicker annealed samples agrees well with the measured

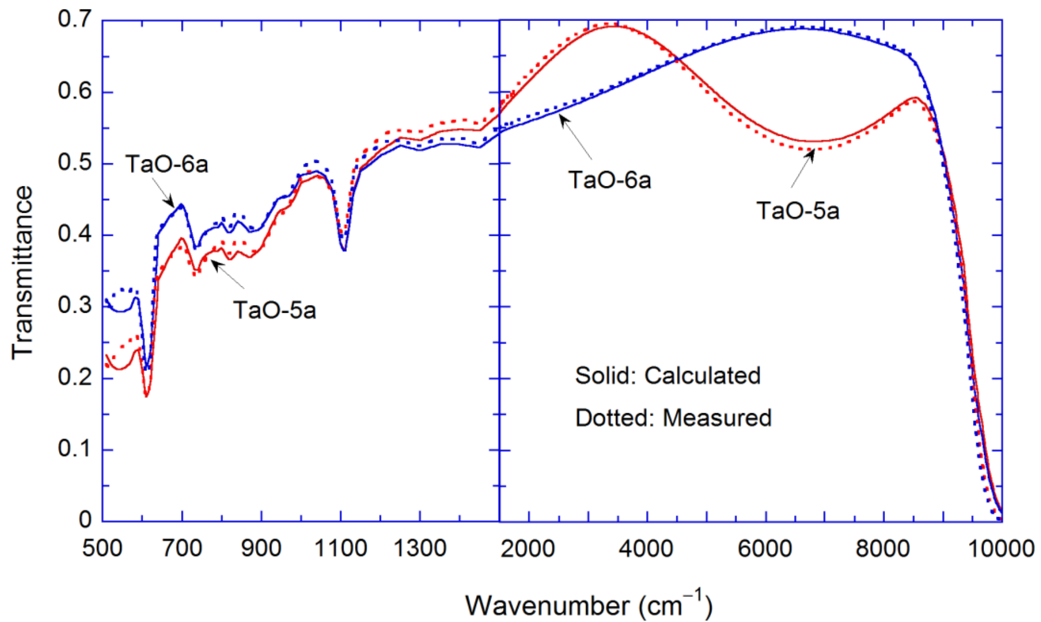

Figure 5.7 Transmittance of samples TaO-5a and TaO-6a. Note that the scale is zoomed from 500 to 1500 cm^{-1} to show features in the far-IR region more clearly.

spectra without introducing any volume scattering. The far-IR measurements were not performed on samples TaO-5a and TaO-6a. Strong absorption in the Si substrate near 1100 cm^{-1} can be clearly seen in Fig. 5.7.

Figure 5.8 compares the measured and calculated reflectance for TaO-3a for both film-side incidence and substrate-side incidence. There is a gradual attenuation in R_f as shown in Fig. 5.8(a), but not in R_s as shown in Fig. 8(b). The substrate-side reflectance

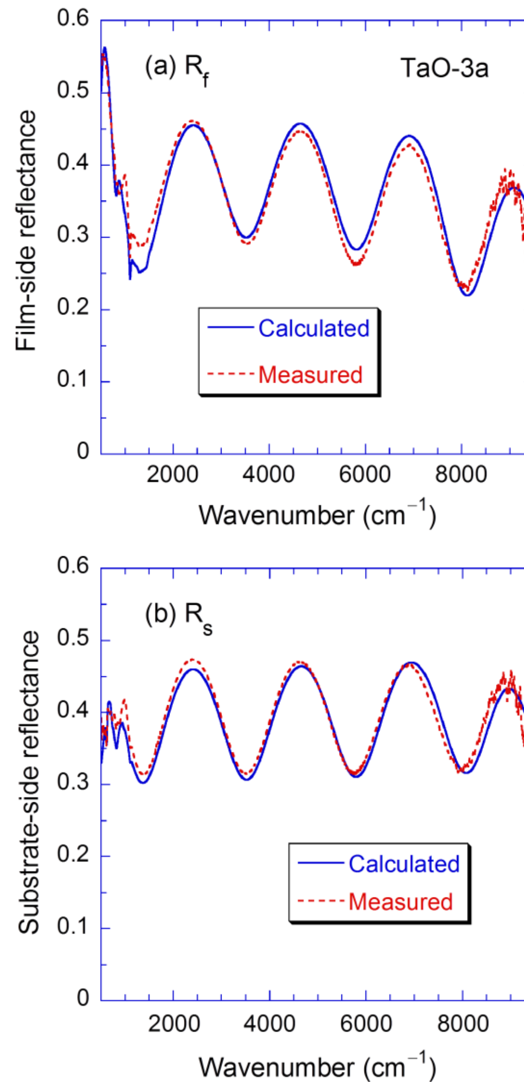

Figure 5.8 Reflectance of sample TaO-3a: (a) film-side; (b) substrate-side. Note that the film-side reflectance decreases toward shorter wavelengths due to scattering, while the substrate-side reflectance is unaffected.

does not show any decrease toward short wavelengths and this is not typical with surface roughness or absorption. The volumetric scattering model captures the phenomenon reasonably well, especially considering the simplicity in the model and its assumption of a spherical geometry and Rayleigh-type independent scattering. The model may break down in the short wavelength end of the spectrum, resulting in large disagreement in T and R_f as shown in Figs. 5.6(b) and 5.8.

It is worth noting that additional reflectance data was also collected but not used in the fitting. Since the reflectance data in the mid-IR region is less reliable than the transmittance data, including them in the fitting would increase the uncertainty. The largest SEE between the model and the experimental data for the transmittance of all the samples was 0.023 and the average was 0.014. The agreement between the reflectance data and the model prediction is good with an average SEE of 0.024.

5.3.3 Comparison with Available Constants

The dielectric function obtained for the amorphous Ta_2O_5 films is plotted in Fig 5.9 in comparison with that obtained from Franke et al [47]. The results are shown from 10 to 1500 cm^{-1} since there is little variation beyond 1500 cm^{-1}, although there are some features due to moisture and the oscillator near 3000 cm^{-1}. Note that the resulting dielectric function is the effective dielectric function expressed in Eq. (4.5). However, in the spectral region shown in the plots, the effect of 5% water content is negligible, i.e., $\varepsilon_{\text{eff}} \approx \varepsilon$. Toward large wavenumbers, the real part approaches A^2 and the imaginary part becomes very small. The residual ε'' is largely due to the free-electron contribution. The phonon features can be clearly seen from the peaks in the imaginary part [78,99]. The Drude term also increases the imaginary part of the dielectric function toward the smaller wavenumbers. The agreement in the dielectric function obtained from this work and from Ref. [47] is reasonable at wavenumbers exceeding 600 cm^{-1}. However, the phonon

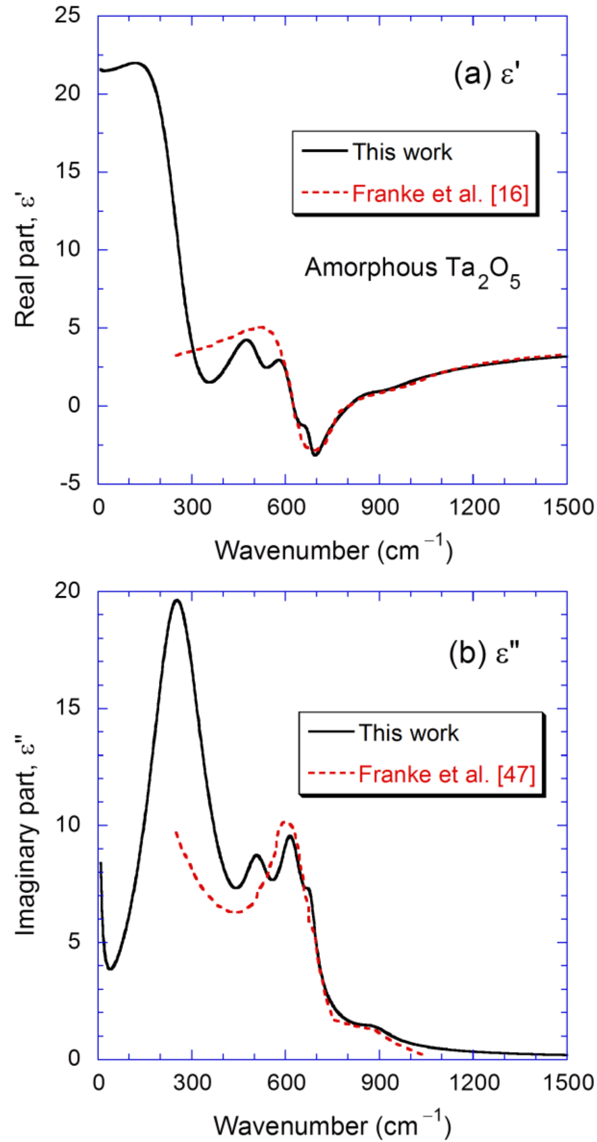

Figure 5.9 Fitted dielectric function of the amorphous Ta_2O_5, in comparison with the values from Ref. [47]: (a) Real part; (b) Imaginary part.

modes below 500 cm^{-1} were not resolved in Ref. [47], resulting in a large deviation at smaller wavenumbers.

Figure 5.10 shows the real and imaginary part of the dielectric function for the annealed samples, compared with those from Ref. [48]. A distinction from the amorphous Ta_2O_5 is the sharp peak at the phonon resonance of 214 cm^{-1} in the imaginary part. While

the oscillator strength defined as $S_j = \omega_{p,j}^2 / \omega_j^2$ is similar to the mode in the amorphous film at 266 cm^{-1}, the reduction in the damping coefficient γ_j gives rise to a narrow band in ε'' [99]. This results in the stronger absorption observed in the transmittance spectrum shown in Fig. 5.6(a). Without the Drude term, the imaginary part is negligible at wavenumbers exceeding 1000 cm^{-1}. Hence, the nanocrystalline Ta_2O_5 has negligible

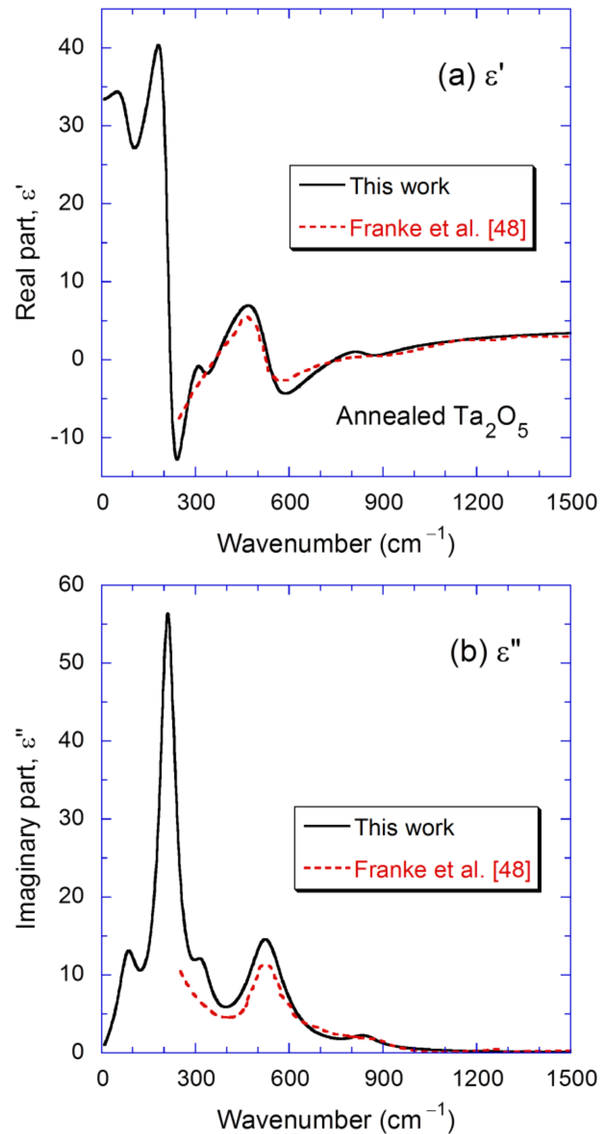

Figure 5.10 Fitted dielectric function of the annealed Ta_2O_5, in comparison with the values from Ref. [48]: (a) Real part; (b) Imaginary part.

absorption in the visible to about 10 μm wavelengths. Towards small wavenumbers, the imaginary part of the dielectric function drops quickly without free-electron absorption, as shown in Fig. 5.10(b). The real part approaches a dielectric constant of 33 for the annealed films and 23 for the amorphous films. These values are within the range reported for the low-frequency (1 MHz) dielectric constants [11,114].

CHAPTER 6

ANALYSIS OF A NEAR-FIELD THERMOPHOTOVOLTAIC WITH A BACKSIDE REFLECTOR

In this chapter the fluctuation dissipation theorem is used to determine the absorption of radiant energy inside of a TPV cell due to direct emission from a tungsten emitter. The gap spacing between the cell and emitter is close enough that near-field enhancement of the heat flux is significant. Once absorbed energy is known as a function of depth into the cell, the spatial photocurrent generation inside and the efficiency of the cell can be modeled using the minority carrier diffusion equations. The efficiency improvement effects of adding a backside mirror to reduce subbandgap radiation and improving the surface recombination rates are investigated.

6.1 Current Generation and Transport

The thermal radiation enhancement caused by the tunneling of electromagnetic waves across the vacuum gap from a hot thermal emitter can result in an enhancement of the energy throughput beyond the black body limit, and as long as the photon energy exceeds the band gap energy it will be absorbed and generates electron-hole pairs. Note that in solar cells the top layer of the cell is sometimes referred to as the emitter; however, for this work we refer to the emitter specifically as the high temperature source of thermal radiation, which is a semi-infinite tungsten half space. Because of the small penetration depth of near-field thermal radiation the majority of the radiation may be absorbed very non-uniformly throughout the depth of the cell [123]. It is thus important to model the minority carrier recombination as realistically as possible, such as in ref. [55]. In order to model current generation and recombination inside the cell, the cell structure is divided into N discrete layers as shown in Fig. 6.1. The same number of

layers is used for the Poynting vector and current generation calculations. Each layer is assumed to be homogenous, isotropic, and isothermal, and the governing equations of current transport are solved within the cell using a finite difference method. For the purposes of our calculations the entire cell is taken to be isothermal at 300 K. The governing equation for minority carrier transport, including the recombination, generation, and diffusion of minority carriers, is given by

$$D\frac{d^2\Delta n}{dz^2}-\frac{\Delta n}{\tau}+g\left(z,\lambda\right)=0 \tag{6.1}$$

where Δn is difference between the number of minority carriers and the equilibrium level, which is based on the temperature and doping concentration at each location; D is the diffusion coefficient based on the carrier mobility; g is the local photo-generation rate of

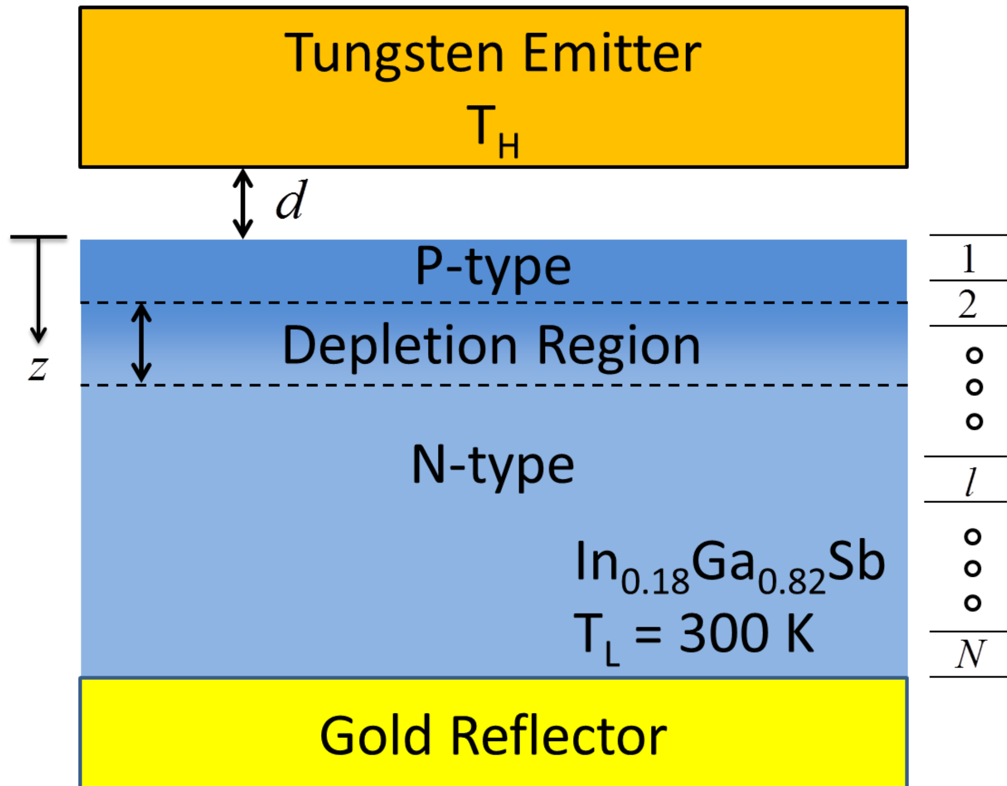

Figure 6.1 TPV schematic showing the p on n configuration of the TPV cell. The cell itself is divided into N discrete and the minority carrier diffusion model is solved with a finite difference method.

minority carriers; and τ is the minority carrier recombination rate. The minority carrier generation rate is the ratio of absorbed energy flux over the photon energy or thus the photon flux per unit volume for a discrete layer *l* is given by

$$g_l(\lambda) = \frac{Q_{\lambda,l}}{t_l E_\lambda} \tag{6.2}$$

where $Q_{\lambda,l}$ is the spectral heat flux absorbed in layer *l* that has photon energies above the bandgap, t_l is the thickness of the discrete layer *l*, and E_λ is the photon energy. The minority carrier equation can be solved along with Poisson's equations for the electrical potential in the TPV cell. Bulk recombination is simplified under a relaxation approximation using an effective relaxation time τ, and the surface recombination due to defect bands is combined into an effective recombination velocity represented by the following boundary condition.

$$D\left.\frac{d\Delta n}{dz}\right|_{\mathrm{surf}} = S\Delta n_{\mathrm{surf}} \tag{6.3}$$

where *S* is the surface recombination velocity. However, to simplify the calculation we apply the depletion region approximation to the Poisson's equations and assume an abrupt junction between the p and n layers of the TPV cell. Under this approximation the depletion region thickness is given by

$$W_{\mathrm{dp}} = \sqrt{\frac{2\varepsilon}{q}\left(\frac{N_{\mathrm{A}} + N_{\mathrm{D}}}{N_{\mathrm{A}} N_{\mathrm{D}}}\right) V_{\mathrm{bi}}} \tag{6.4}$$

where the built in voltage is given by

$$V_{\mathrm{bi}} = \frac{k_{\mathrm{B}} T}{q} \ln\left[\frac{N_{\mathrm{D}} N_{\mathrm{A}}}{n_{\mathrm{i}}^2}\right] \tag{6.5}$$

The new variables introduced in Eqs. (6.4) and (6.5) are the acceptor concentration N_{A}, donor concentration N_{D}, dielectric constant of the cell ε, and the intrinsic carrier

concentration n_i, and q is the fundamental charge of an electron. This study utilizes the same parameters used in ref. [55], where the p-layer is doped with a concentration of 10^{19} cm^{-3} and the n-layer has a doping concentration of 10^{17} cm^{-3}. All of the other properties of the $In_{0.18}Ga_{0.82}Sb$ ternary alloy are taken from Gonzalez-Cuevas et al. [124]. The values used in ref. [55] are taken as the reference parameters. The bandgap of the alloy of choice, $In_{0.18}Ga_{0.82}Sb$, is 0.56 eV (2.22 μm). Some of these parameters are varied to study their effect on the efficiency. The minority diffusion of electrons in p-region is described by the following parameters $D_{\mathrm{e}} = 125\ \mathrm{cm}^2\ \mathrm{s}^{-1}$, $\tau_{\mathrm{e}} = 9.75\ \mathrm{ns}$, $S_{\mathrm{e}} = 7.4 \times 10^4\ \mathrm{m\ s}^{-1}$ and has a width of $W_{\mathrm{p}} = 400\ \mathrm{nm}$. In the n-region, hole minority diffusion is described by the following parameters $D_{\mathrm{h}} = 31.3\ \mathrm{cm}^2\ \mathrm{s}^{-1}$, $\tau_{\mathrm{h}} = 30.8\ \mathrm{ns}$, $S_{\mathrm{h}} = 0\ \mathrm{m\ s}^{-1}$ and has a width of $W_{\mathrm{n}} = 10\ \mu\mathrm{m}$. Finally, the width of the depletion region is $W_{\mathrm{dp}} = 100\ \mathrm{nm}$. The emitter temperature reference value is $T_{\mathrm{H}} = 2000\ \mathrm{K}$ and the TPV cell is at $T_{\mathrm{L}} = 300\ \mathrm{K}$.

Under the depletion region approximation any minority carriers that reach the depletion region will be swept away by the built-in electric field generated in this narrow region. Thus in the depletion region, by neglecting recombination, the current density due to absorption in the depletion region is given by

$$J_{\mathrm{dp}} = \int_0^{\lambda_g} q g_{\mathrm{dp}} W_{\mathrm{dp}} d\lambda \tag{6.6}$$

Since under the depletion region approximation we have neglected the electric field in the quasi-neutral regions of the TPV cell the current in the n and p regions of the cell are given by the diffusion current density

$$J_{\lambda} = -qD \frac{d\Delta n}{dz} \tag{6.7}$$

The total photo-generation current density in the cell due to photogeneration in the n and p regions is given by integrating the photon flux over all wavelengths up to the wavelength at the bandgap, at the depletion region boundary.

$$J_{\text{p}} = \int_0^{\lambda_g} J_\lambda \left(z = W_{\text{p}} \right) d\lambda \text{ for p region} \tag{6.8}$$

$$J_{\text{n}} = \int_0^{\lambda_g} J_\lambda \left(z = W_{\text{p}} + W_{\text{dp}} \right) d\lambda \text{ for n region} \tag{6.9}$$

where the current density is determined from the minority carrier diffusion equations and thus accounts for the bulk and surface recombination. The total photocurrent generation is thus the sum of all three currents

$$J_{\text{ph}} = J_{\text{dp}} + J_{\text{n}} + J_{\text{p}} \tag{6.10}$$

In order to determine the maximal power output of the cell the dark current density of the cell must be taken into account, which for an ideal diode the saturation current is given by

$$J_0 = q \left(\frac{n_{\text{i}}^2 D_{\text{h}}}{N_{\text{D}} \sqrt{\tau_{\text{h}}}} + \frac{n_{\text{i}}^2 D_{\text{e}}}{N_{\text{A}} \sqrt{\tau_{\text{e}}}} \right) \tag{6.11}$$

where e and h refer to electron and hole minority carriers and indicate the properties of the p and n doped regions, respectively. Equation (6.11) implicitly assumes that the recombination velocity at the top of the cell does not affect the dark current or specifically that the diffusion length, $L = \sqrt{D\tau}$, is much larger than the width of the quasi-neutral region of the cells $L \gg W_{\text{p,n}}$. In general the surface recombination velocity may need to be considered in the dark saturation current calculation [125]. Furthermore, Laroche et al. [3] discussed the effect of carrier density on the relaxation time and showed that near-field effects can be neglected. In order to stay consistent with Park et al. [55], Eq. (6.11) was used and it was confirmed that the error in the maximal power output associated with Eq. (6.11) would be less than 5% for all the gap distances when compared to the maximal power with the exact solution for the dark current, even though the dark current itself may change significantly, it remains small compared to the generated photocurrent. Under a forward bias, the cell will generate a dark current when

it is not illuminated. The total current of the cell operating under a forward bias will be the photocurrent minus the detrimental dark current, the total current is therefore

$$J = J_{\text{ph}} - J_0\left[\exp\left(qV/k_{\text{B}}T\right) - 1\right] \tag{6.12}$$

where it is assumed the dark current generation due to recombination in the depletion region is negligible, and is calculated using the Shockley equation for an ideal diode [126]. The maximal output power can then be calculated from the current voltage characteristics of the cell by setting the derivative of the expression for power to zero, in the usual way resulting in an optimal power given by

$$P_{\text{E}} = J_{\text{ph}}V_{\text{oc}}\left[1 - \frac{1}{\ln\left(J_{\text{ph}}/J_0\right)}\right]\left\{1 - \frac{\ln\left[\ln\left(J_{\text{ph}}/J_0\right)\right]}{\ln\left(J_{\text{ph}}/J_0\right)}\right\} \tag{6.13}$$

The open circuit voltage is given by setting the current to zero and finding $V_{\text{oc}} = \left(k_{\text{B}}T/q\right)\ln\left(J_{\text{ph}}/J_0 + 1\right)$. Finally the efficiency of the TPV cell is defined as the ratio of the generated electric power to the radiative flux at the surface of the cell

$$\eta = \frac{P_{\text{E}}}{P_{\text{R}}\left(z = 0\right)} \tag{6.14}$$

which even for near-field, must still be governed by the second law of thermodynamics and will never exceed the Carnot efficiency which for our case of an emitter at 2000 K and TPV cell at 300 K is 85%. The described procedure is the same general calculation procedure following Ref. [55] and thus some of the less important details about the calculation are left out, but can found within that reference and those therein.

6.2 Results and Discussion

6.2.1 Minimizing Sub-Bandgap Radiation

Park et al. [55] mentioned that a large amount of sub-bandgap radiation is lost in their analysis because the cells are assumed to be semi-infinite. Because of the large

penetration depth of sub-bandgap radiation a large portion of this radiation can be reduced by simply adding a back side reflector. In order to realistically estimate the enhancement in the efficiency by reducing the sub-bandgap radiation, an Au layer is added to the backside of the $In_{0.18}Ga_{0.82}Sb$ cell (See "Gold Reflector" in Fig. 6.1). Au is chosen because of the high reflectivity in the IR region of the spectrum which is below the bandgap of the TPV cell. For modeling purposes, the optical constants of Au are taken from Palik [90]. For an emitter at 2000 K the change in the 100% quantum efficiency curve and the efficiency modeling carrier recombination is shown in Fig. 6.2. Because of the reduction in sub-bandgap wasted heat the 100% quantum efficiency is

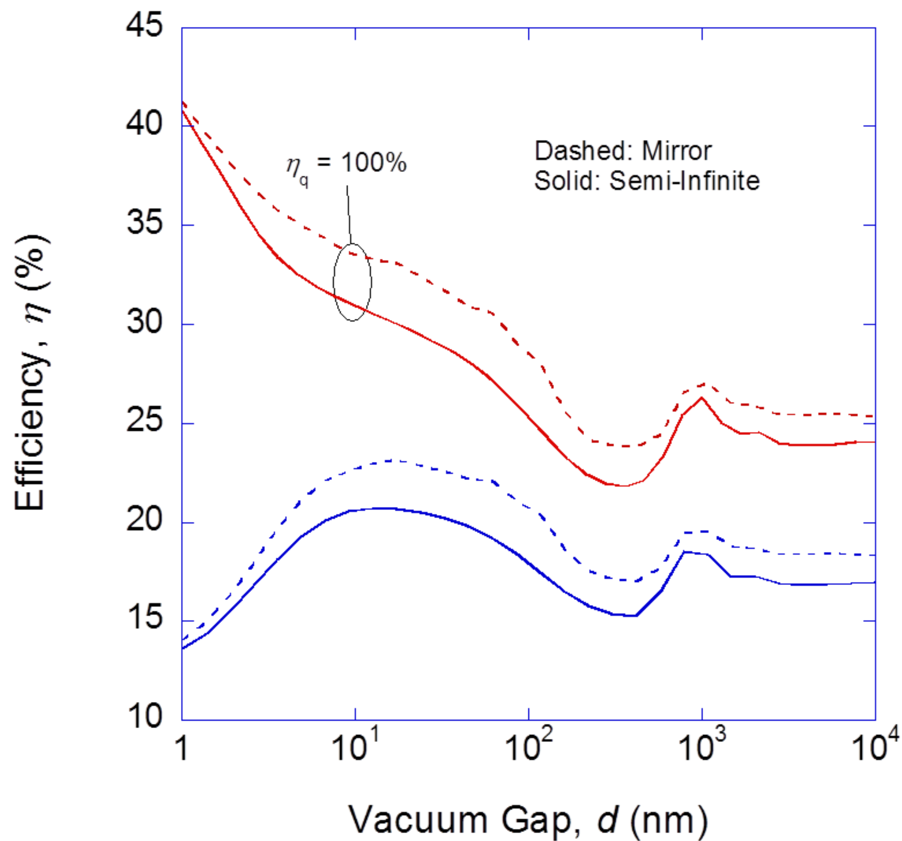

Figure 6.2 The efficiency of a TPV cell with a tungsten emitter at 2000 K with and without mirror on the backside to reduce sub-bandgap radiation. The mirror increases both the ideal and actual efficiency of the TPV based on the current generation calculated from the minority diffusion equation.

higher for the cell with the reflector. For similar reasons the efficiency in the cell with recombination is also higher, but the current cell still suffers from poor performance at small gap distances even with the mirror. The performance enhancement at 2000 K peaks around ~15% relative to the original efficiency. The efficiency curve is fairly smooth function of gap distance without a mirror except, at larger gap spacing where there are interference effects. The presence of a mirror causes the efficiency curve to be less smooth due to additional interference effects.

At lower temperatures, the characteristic wavelength of light is red-shifted and the importance of a reflector becomes increasingly important in relative terms. The temperature dependence of the efficiency enhancement is shown in Figs. 6.3(a) and (b). Figure 6.3(a) shows the absolute efficiency as a function of gap spacing for different emitter temperatures. In general the overall efficiency is worse at lower temperatures. The relative efficiency improvement by adding the mirror is calculated by taking the ratio of the difference in efficiency with and without the mirror over the efficiency without the mirror, $(\eta_{\mathrm{Au}} - \eta)/\eta$, and is displayed in Fig. 6.3(b). In Fig. 6.3(b) it is shown that at lower emitter temperatures, around 1250 K, the relative performance enhancement is much higher, peak around ~35%. Furthermore, because of the mirror interference effects are observed. The interference effect is the cause of the jaggedness of the curves in Fig. 6.3(b). Because of the red-shifting of the characteristic frequency a mirror or filter becomes an essential component of any high performance near-field TPV systems. Since 2000 K is on the high end for the temperature of the potential sources, mirrors and filters specially designed for near-field are extremely important for most available temperature sources. At extremely small gap (<10 nm) tunneling of high frequency radiation is more significant and the mirror is not as effective; however, such small gap spacings may not be realistic to construct with current technology.

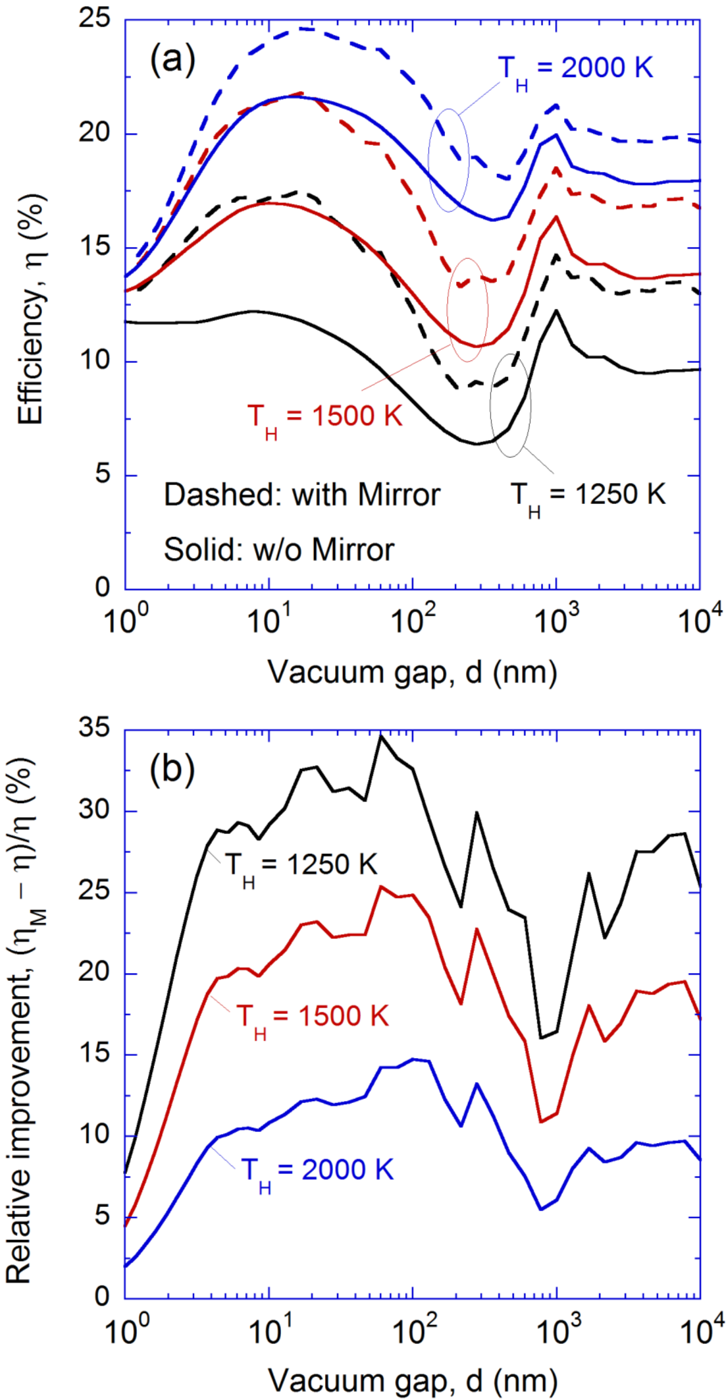

Figure 6.3 A study of the efficiency improvement of the mirror at different tungsten emitter temperatures: (a) the absolute efficiency with and without the mirror at various temperatures and (b) the relative improvement in efficiency.

The effect of the mirror on the heat flux is discussed next. Figure 6.4 shows the *z*-component Poynting vector as a function of wavelength and depth into the solar cells. The emitter temperature is set at 1500 K and the vacuum gap spacing is d = 10 nm. The results without the Au mirror are shown in Fig. 6.4(a) and that with mirror are in Fig. 6.4(b). From this figure one can deduce the peak wavelength as well as get a general idea of the penetration depth of near-field thermal radiation. The corresponding reduction in radiation can be seen in the sub-bandgap region where the penetration depth is clearly very high in Fig. 6.4(a) because the intensity does not change with depth by any significant amount. However, for frequencies below the bandgap energy the penetration depth is much smaller and most of the energy is absorbed in the vicinity of the surface. Figure 6.5 shows the overall Poynting vector at the surface of cell as a function of wavelength for T_H = 1500 K and d = 10 nm It can be seen that the heat flux is reduced at longer wavelengths when the mirror is present. A reduction to the right of the vertical line showing the band gap location is desired because this is wasted energy. The mirror also reduces some of the radiation with energy above the band gap which has a larger penetration depth, although undesirable this does not have a significant negative effect on the efficiency of the cell. Given the geometry of the cell and the small penetration depth of near-field radiation there are not many down sides to including a mirror directly attached to the backside of the cell, which can also be used as an electrical contact. Since the base of the cell is longer than the diffusion length, which is ~9 μm, the large surface recombination velocity associated with an Ohmic contact does not seem to be an issue to the overall efficiency of the cell. For small cells it may be desirable to consider the analysis with a back side field. Similar results can be achieved with filters, but the addition of a mirror is a much simpler solution.

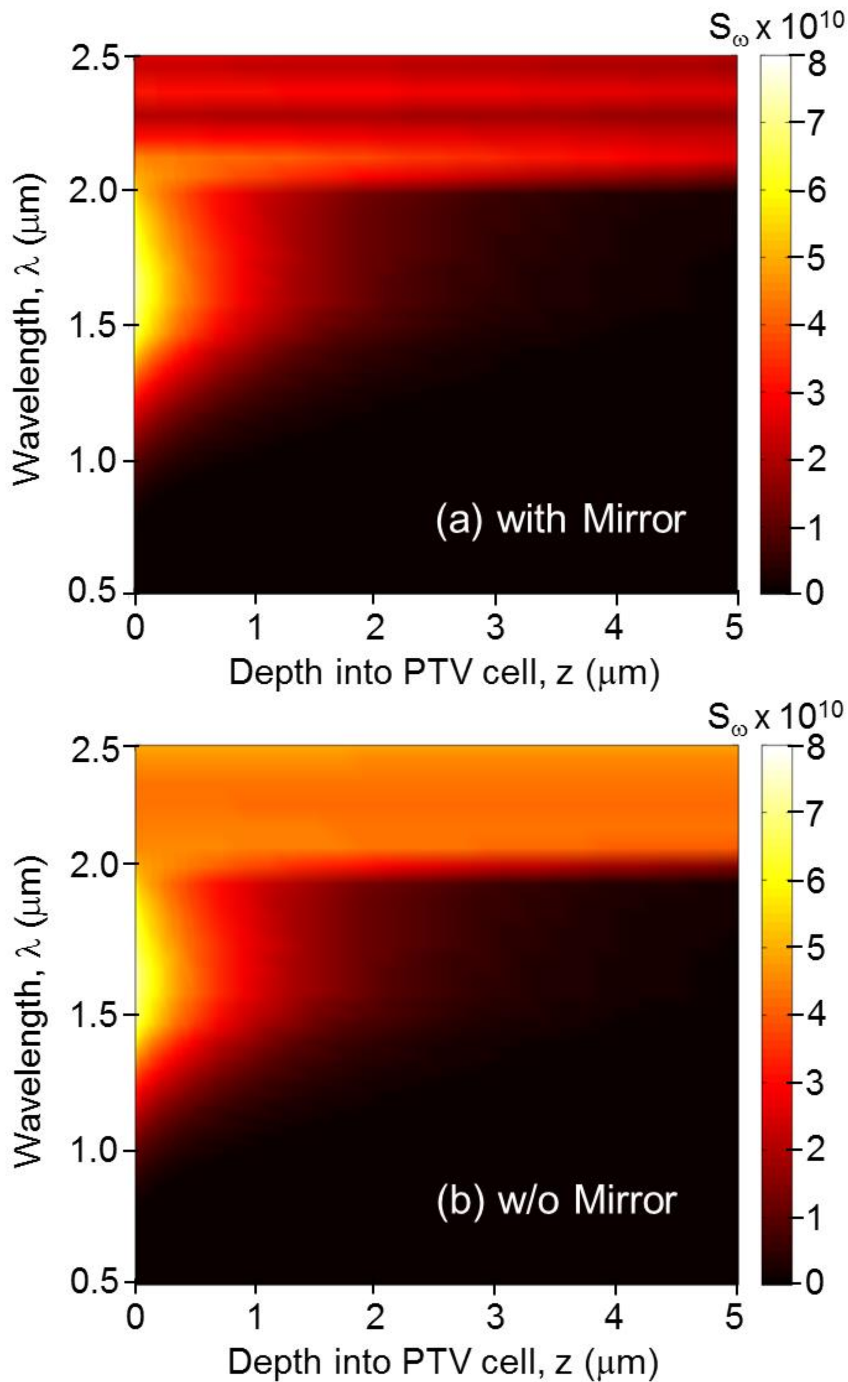

Figure 6.4 Contour plot showing the Poynting vector as a function of depth for various wavelengths with a 1500 K emitter and a gap spacing of 10 nm: (a) without a backside reflector and (b) with a backside reflector, showing the reduction in Poynting vector beyond the bandgap.

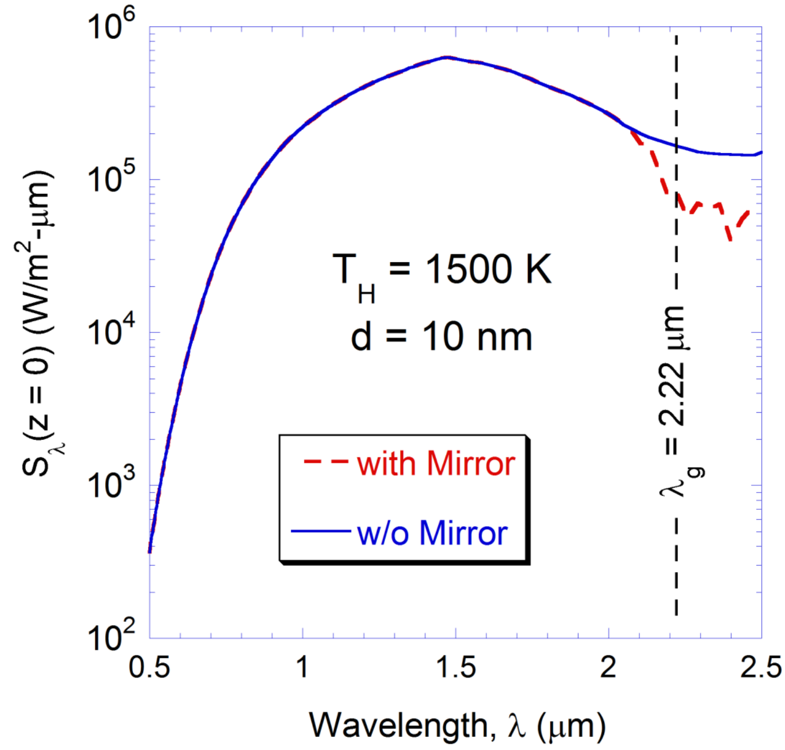

Figure 6.5 Poynting vector at the TPV surface at varying wavelength. Beyond the bandgap the reduction in the Poynting vector can be seen.

6.2.2 Minimizing Recombination Effects.

Because of the ultra-small penetration depth of near-field radiation the recombination effect near the surface is extremely important. By reducing the effective recombination velocity at the top surface and recombination with the cell, the efficiency of the cell will approach the quantum efficiency limit. The trend shown by Park et al. [55] was that the efficiency will decrease toward smaller gap spacing. This trend is primarily due to surface recombination effects since the penetration depth of evanescent waves is characteristically $\delta_{\mathrm{p}} \approx 1/(2k_x)$ [123]. Thus, at a smaller gap spacing the carrier concentration is higher at the surface, because radiation with a larger k_x and smaller penetration depth can tunnel across the gap causing the efficiency to become dominated by the surface recombination losses. The importance of the small penetration depth and

recombination velocity at the surface were pointed out by Park et al. [55], but the effect of reducing surface recombination was not analyzed in detail in that work. When not considering the recombination at surface contacts, the recombination velocity of S_e = 7×10^4 m/s used in that work may be on the high end for some III-V semiconductors, which can have notably lower surface recombination velocities than Si solar cells.

The effect of altering the recombination velocity at the top surface is shown in Figs. 6.6 (a) and (b). The calculation is based on the properties given in Section 2 at an emitter temperature of 2000 K where (a) has and (b) does not have the mirror. It appears from the figure that below a value of S_e of approximately 1,000 m/s the efficiency does not improve much with further reducing surface recombination velocity, this value of surface recombination velocity could be achieved with a passivated surface. When the recombination velocity becomes this low, the reduction below the 100% quantum line efficiency line is due to bulk diffusion recombination limitations. The difference between the mirror and no mirror configuration is an efficiency offset at larger gap spacings, but the two become the same at smaller gap spacings where the long wavelength radiation is relatively less significant.

Figure 6.7 (a) shows the carrier concentration at the surface of the cell, which is proportional to the surface recombination rate under our model. The surface recombination rate can be found from

$$R_{\text{surf}} = S_{\text{e}}\Delta n\left(z=0\right) \tag{6.15}$$

On the left vertical axis of the figure is the total bulk minority carrier recombination rate in the p-layer given by

$$R_{\text{bulk}} = \sum_{l=1}^{M} \frac{\Delta n_l}{\tau} t_l \tag{6.16}$$

where M is the number of layers in the p-region. Note that R_{bulk} represents the integration of the recombination rate per unit volume over the p-region. From Fig. 6.7(a)

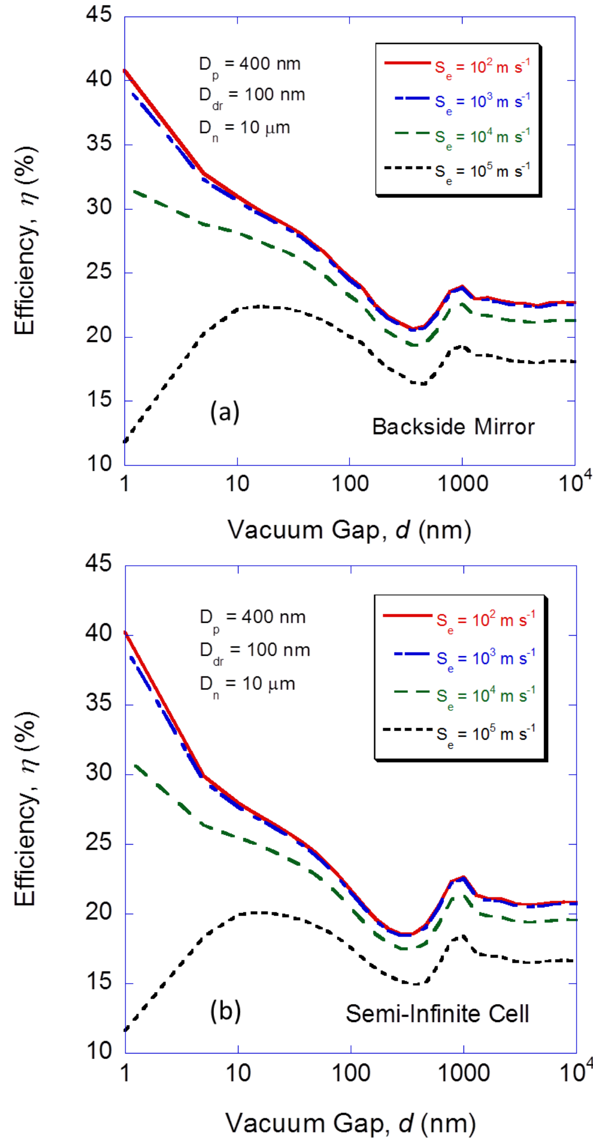

Figure 6.6 Efficiency improvement by reducing recombination at the top surface with an emitter of at 2000K: (a) with a mirror and (b) without a mirror. If a low enough recombination velocity can be achieved the trend of efficiency toward smaller gap spacing reverses.

i

t can be seen that for small recombination velocities bulk recombination is dominant and remains fairly constant as the recombination velocity increases until surface recombination takes over as the dominant mechanism. Eventually, the overall carrier concentration and bulk recombination rate drops with increasing surface recombination velocity, because of the large carrier losses at the surface. Figure 6.7(a) can be

understood in conjunction with Fig. 6.7(b), which shows the ratio of Eq. (6.16) to Eq. (6.15) at different surface recombination velocities with a gap spacing of 10 nm. In Fig. 6.7(b), the critical surface recombination velocity, $S_{e,c}$, is shown and is defined as when the ratio, R_{bulk}/R_{surf}, becomes equal to one. At lower surface recombination velocities this ratio will be larger than one and surface recombination will not be the dominant

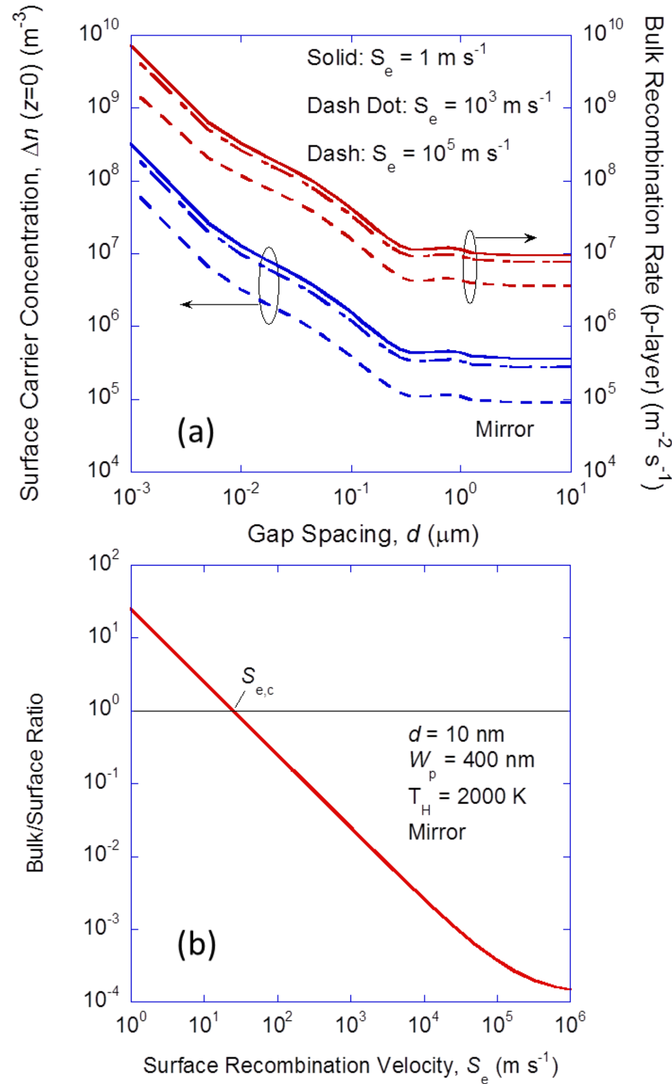

Figure 6.7 For an emitter at 2000 K and backside mirror: (a) Surface minority carrier concentration and bulk recombination rate at different S_e and (b) ratio of bulk recombination rate to surface recombination rate with the transition point between the dominant mechanism shown as the critical surface recombination velocity, $S_{e,c}$.

source of recombination losses. Below this recombination velocity the majority of recombination will be due to diffusion and will depend on the thickness of the top layer and the relaxation time of minority carriers.

It is obviously desirable to prepare the surface of the TPV cell, or choose materials, so that the effective recombination velocity is smaller than this number ($S_{e,c}$ approximately 40 m/s), such that the performance will not be drastically altered by the small penetration depth associated with near-field enhanced radiation. This gives an additional criterion that the surface preparation must meet for near-field TPV devices which will differ from traditional TPV cells because of the difference in the penetration depths associated with evanescent waves in the near-field and propagating waves in the far-field. Furthermore, the choice of contacts and preparation of the contacts on the front surface must be chosen so that the effective average surface recombination velocity, such as estimated in Ref. [125], is smaller than this critical value. Below this value enhancement of the cell will depend on other factors such as reducing bulk recombination or changing the spectral distribution of the source.

A thin window layer could potentially be used to reduce the surface recombination velocity but the tradeoff in heat flux must be considered. Fu and Tan [127] considered adding a thin layer of SiC to the top surface to one of two half-spaces and determined that there would be significant reduction of the near-field heat flux at small gap spacing for a 10 nm layer. It is expected that the effect would be similar for a suitable passivation layer, this reduction in heat flux is similar to the reduction in flux associated increasing the gap spacing and therefore if the layer is non-participating a high refractive index may be desirable.

A suitable layer would need the following characteristics: a higher bandgap energy, superior minority carrier mobility, low defect density, and a suitably higher conduction band potential in order to prevent minority carrier diffusion to the surface of the cell [125]. The layer would need to remain sufficiently thin, because a thin layer will

not have a less significant effect on the electric field generated by fluctuating currents in the emitter, to not adversely affect the heat flux. There is some flexibility with semiconductor material choice, as long as lattice matching condition is met. The critical thickness can be found from the lattice mismatch, $f = |a_\mathrm{f} - a_\mathrm{s}| / a_\mathrm{f}$, where a_f is the film (window) lattice constant and a_s is the substrate (TPV cell) lattice constant. The critical thickness of a film is approximately the lattice constant of the substrate divided by twice the mismatch, $a_\mathrm{s}/2f$. Conveniently for a thickness less than the critical thickness, the lattice will conform to the lattice structure to some extent meaning that there are a broader number of semiconductor materials that may work as layer that reduces the surface recombination velocity.

The combined effect of improved surface recombination and sub-wavelength reflection were illustrated in Figs. 6.6 (a) and (b). In addition to reducing the surface recombination we consider how altering the p-region thickness, W_p, affects the efficiency of the cell. Park et al. [55] and Francouer et al. [56] considered a thickness of 400 nm for the top (p-layer) region. High efficiency cells might have thinner layers than 400 nm, a smaller top layer thickness will improve the efficiency slightly by reducing the amount of diffusion losses in the top layer where most of the radiation is absorbed in the near-field case. The efficiency improvement with changing thickness of the top layer is shown in Figs. 6.8 (a) and (b), with and without the mirror, at an emitter temperature of 2000 K. Under the current model decreasing the top layer thickness has resulted in more photocurrent generation closer to the depletion region. This will lead to lower diffusion losses, but the performance will still suffer from the effects of the large surface recombination rate. Additionally for the thinner p-layer the effect from surfaces on the dark current may be more significant, it may also be more important to avoid some of the simplifications made in this study for small p-layers. One may also notice that for the small p-layer thickness of 100 nm, the efficiency trend appears different with and without

the mirror toward smaller gap spacings. This is because the mirror enhances at larger gap spacings but has no effect at smaller gap spacings where the two figures will have the same efficiency value in the limiting case of zero gap spacing. Thus the mirror efficiency

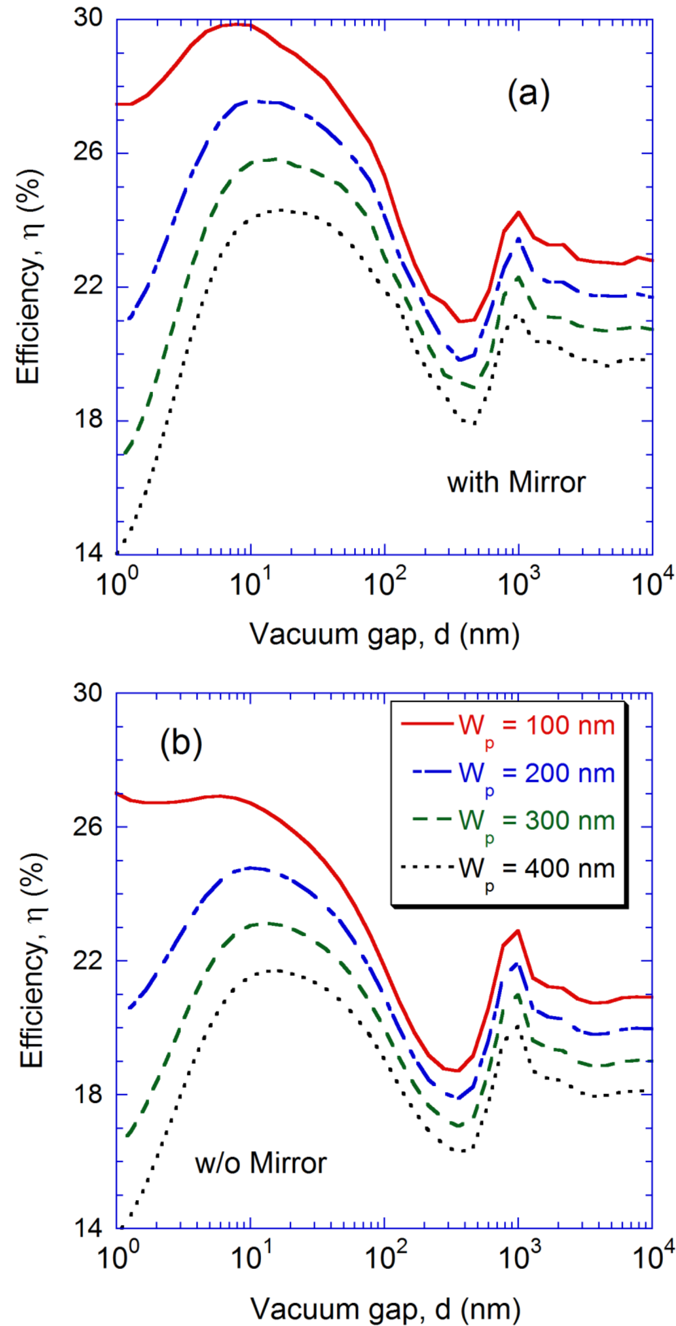

Figure 6.8 Efficiency improvement for varying thicknesses of the p-region with a 2000 K emitter: (a) with mirror and (b) without mirror. Improvement is due to reduction in bulk recombination.

curve appears to go down because the mirror is no longer helping improve efficiency toward 1 nm gap spacing.

CHAPTER 7

ENERGY STREAMLINES IN UNIAXIAL ANISOTROPIC HYPERBOLIC METAMATERIALS

In the present chapter the flow of energy through metallodielectric photonic crystals (MDPCs) is studied. MDPCs have the potential to image or guide evanescent waves [67,68], and offer unique possibilities for applications in near-field devices. Hyperbolic modes associated with uniaxial anisotropic materials, which are predicted by EMA in MDPCs, can result in further enhancement of the heat flux of near-field radiation. Section 7.1 introduces some fundamental equations that extend the Green's function method to uniaxial anisotropic media. In section 7.2 the lateral displacement of energy as it flows between two uniaxial anisotropic structures is determine from the energy streamline method. The Poynting vector inside the media and vacuum is calculated by applying the Green's function method and fluctuation dissipation theorem. Two anisotropic structures with hyperbolic modes in the infrared region of the spectrum are considered. One structure with alternating layers of doped Si and Ge and a second structure with alternating layers of SiC and Ge are investigated. The average lateral displacement, penetration depth, and heat transfer rate are determined. From the lateral displacement and penetration depth, characteristic dimensions of the structure necessary for the plane wave 1D semi-infinite media assumption to remain valid are estimated. Finally, in section 7.3 some observations about the agreement between energy streamlines calculated by EMA and by TMM in MDPCs made of Ag and a dielectric are made.

7.1 Green's Function for an Uniaxial Anisotropic Multilayer Structure

The Green's function for multilayer uniaxial anisotropic structures with an arbitrary number of layers is calculated following the same procedure as the isotropic multilayer structure in chapter 2, with some necessary modifications. The dielectric function for a uniaxial anisotropic media with a vertical optical axis (in the z-direction) becomes a tensor of the form

$$\overline{\overline{\varepsilon}} = \begin{bmatrix} \varepsilon_t & 0 & 0 \\ 0 & \varepsilon_t & 0 \\ 0 & 0 & \varepsilon_z \end{bmatrix} \tag{7.1}$$

The transverse dielectric function, ε_t, is the same in the x or y direction for a uniaxial medium with a vertical optical axis. Because the dielectric function is a tensor, the electric displacement and electric field may no longer be in the same direction. The primary and reflected Green's functions for a uniaxial anisotropic media become [128,129]

$$\overline{\overline{\mathbf{g}}}_{\mathrm{P},s}^{\succ/\prec}\left(\beta, z, z', \omega\right) = \frac{i}{2}\begin{bmatrix} \dfrac{1}{\gamma_{\mathrm{o},s}}\hat{\mathbf{o}}\hat{\mathbf{o}}e^{\pm i\gamma_{\mathrm{o},s}(z-z')} \\ +\dfrac{k_0^2\left(\varepsilon_{t,s}+\varepsilon_{z,s}\right)-\left(k_{\mathrm{e},s}\right)^2}{\gamma_{\mathrm{e},s}k_0^2\varepsilon_{z,s}}\hat{\mathbf{e}}_s^{\pm}\hat{\mathbf{e}}_s^{\pm}e^{\pm i\gamma_{\mathrm{e},s}(z-z')} \end{bmatrix} \tag{7.2}$$

$$\begin{aligned} &\overline{\overline{\mathbf{g}}}_{\mathrm{S},l}\left(\beta, z, z', \omega\right) \\ &= \frac{i}{2}\begin{bmatrix} \dfrac{1}{\gamma_{\mathrm{o,s}}}\left(A_{l,\mathrm{TE}}^{+}\hat{\mathbf{s}}_l^{+} + A_{l,\mathrm{TE}}^{-}\hat{\mathbf{s}}_l^{+} + B_{l,\mathrm{TE}}^{+}\hat{\mathbf{s}}_l^{-} + B_{l,\mathrm{TE}}^{-}\hat{\mathbf{s}}_l^{-}\right)\hat{\mathbf{o}} \\ -\dfrac{k_0^2\left(\varepsilon_{t,s}+\varepsilon_{z,s}\right)-\left(k_{\mathrm{e},s}\right)^2}{\gamma_{\mathrm{e},s}k_0^2\varepsilon_{z,s}} \\ \times\left(A_{l,\mathrm{TM}}^{+}\hat{\mathbf{e}}_l^{+}\hat{\mathbf{e}}_s^{+} + A_{l,\mathrm{TM}}^{-}\hat{\mathbf{e}}_l^{+}\hat{\mathbf{e}}_s^{-} + B_{l,\mathrm{TM}}^{+}\hat{\mathbf{e}}_l^{-}\hat{\mathbf{e}}_s^{+} + B_{l,\mathrm{TM}}^{-}\hat{\mathbf{e}}_s^{-}\hat{\mathbf{e}}_s^{-}\right) \end{bmatrix} \end{aligned} \tag{7.3}$$

where $k_{\mathrm{e},s}$ is the magnitude of the extraordinary wavevector in layer s, $\gamma_{\mathrm{e},s}$ and $\gamma_{\mathrm{o,s}}$ are the z-components of the wavevector for extraordinary and ordinary waves in layer s, and

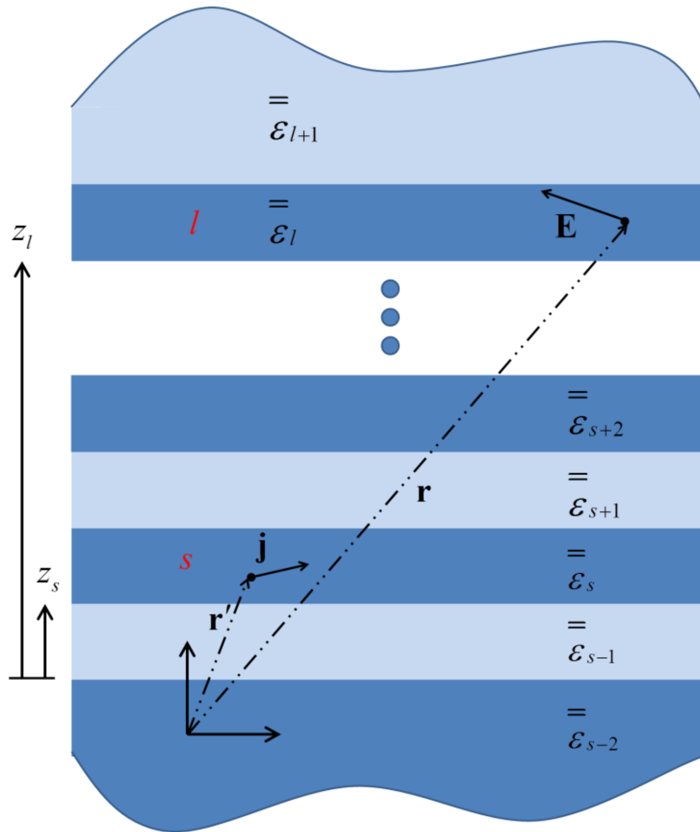

Figure 7.1 A multilayer structure which is composed of layers with a uniaxial anisotropic dielectric tensor. A source embedded in layer s located at the source location $\mathbf{r}'$ will generate an electric field in layer l at location $\mathbf{r}$.

k_0 is the vacuum wavevector magnitude. The symbols $\succ$ and $\prec$ indicate whether the qprimary wave is traveling forward or backwards, respectively. A forward primary wave means that the receiver location is at a larger z coordinate than the source located at z', a backward primary wave would be the reverse situation. This distinction between forward and backward waves should be carefully noted when performing the integration over the source volume when the receiver is located in the source layer, the appropriate integrand of the primary Green's function should be used depending on whether $z > z'$ or $z < z'$. The rest of the coefficients in Eq. (7.3) are discussed next, but first note that the ordinary component of the Green's function for a uniaxial media with a vertical optical axis is calculated using the same procedure as TE waves in an isotropic medium, given in

chapter 2. However, for extraordinary waves the calculation is different from isotropic TM waves. The extraordinary vector is now defined by

$$\hat{\mathbf{e}}_l^{\pm} = \frac{\mp\gamma_{\mathrm{ez},l}\varepsilon_{z,l}\hat{\mathbf{r}} + \beta\varepsilon_{t,l}\hat{\mathbf{z}}}{\sqrt{\left(\gamma_{\mathrm{ez},l}\varepsilon_{z,l}\right)^2 + \left(\beta\varepsilon_{t,l}\right)^2}} \tag{7.4}$$

For this type of medium the dispersion relations for the wavevector components are

$$\gamma_{\mathrm{o}l}^2 + \beta^2 = \varepsilon_{t,l}k_0^2 \tag{7.5}$$

$$\frac{\gamma_{\mathrm{e}l}^2}{\varepsilon_{t,l}} + \frac{\beta^2}{\varepsilon_{z,l}} = k_0^2 \tag{7.6}$$

While the coefficients for ordinary waves, A_l and B_l, remain unchanged from the isotropic TE wave amplitudes, for extraordinary waves the TM case needs a few modifications. The dynamical matrix used in the TMM in layer i is redefined as

$$\mathbf{D}_i = \begin{bmatrix} 1 & 1 \\ \gamma_{\mathrm{e}i}/\varepsilon_{t,i} & -\gamma_{\mathrm{e}i}/\varepsilon_{t,i} \end{bmatrix} \tag{7.7}$$

Applying this change will give the correct magnetic field amplitude in each layer when using the TMM. The magnetic field amplitudes for extraordinary waves are found by solving the following equations

$$\begin{bmatrix} A_{N,\mathrm{TM}}'^{+} \\ 0 \end{bmatrix} = \mathbf{M}_{s+1,N}\left\{\mathbf{M}_{0,s}\begin{bmatrix} 0 \\ B_{0,\mathrm{TM}}'^{+} \end{bmatrix} + \begin{bmatrix} e^{i\gamma_{\mathrm{es}}(z_{s+1}-z')} \\ 0 \end{bmatrix}\right\} \tag{7.8}$$

$$\begin{bmatrix} A_{N,\mathrm{TM}}'^{-} \\ 0 \end{bmatrix} = \mathbf{M}_{s+1,N}\left\{\mathbf{M}_{0,s}\begin{bmatrix} 0 \\ B_{0,\mathrm{TM}}'^{-} \end{bmatrix} + \begin{bmatrix} 0 \\ e^{i\gamma_{\mathrm{es}}(z'-z_s)} \end{bmatrix}\right\} \tag{7.9}$$

where $\mathbf{M}_{i,j}$ is the transfer matrix between layers i and j using the new dynamical matrices in Eq. (7.7). Once $B_{0,\mathrm{TM}}$ is solved the coefficient in any layer can be found from

$$\begin{bmatrix} A'^{+}_{l,\mathrm{TM}} e^{-i\gamma_{el}\left(z-z_{l-1}\right)} \\ B'^{+}_{l,\mathrm{TE}} e^{i\gamma_{el}\left(z-z_{l-1}\right)} \end{bmatrix} = \begin{cases} \mathbf{M}_{s+1,l}\left(\mathbf{M}_{0,s}\begin{bmatrix} 0 \\ B'^{+}_{0,\mathrm{TM}} \end{bmatrix} + \begin{bmatrix} e^{i\gamma_{es}\left(z_{s+1}-z'\right)} \\ 0 \end{bmatrix}\right), & z_l > z_s \\ \mathbf{M}_{0,l}\begin{bmatrix} 0 \\ B'^{+}_{0,\mathrm{TM}} \end{bmatrix}, & z_l < z_s \end{cases} \tag{7.10}$$

$$\begin{bmatrix} A'^{-}_{l,\mathrm{TM}} e^{-i\gamma_{el}\left(z-z_{l-1}\right)} \\ B'^{-}_{l,\mathrm{TM}} e^{i\gamma_{el}\left(z-z_{l-1}\right)} \end{bmatrix} = \begin{cases} \mathbf{M}_{s+1,l}\left(\mathbf{M}_{0,s}\begin{bmatrix} 0 \\ B'^{+}_{0,\mathrm{TM}} \end{bmatrix} + \begin{bmatrix} 0 \\ e^{i\gamma_{es}\left(z'-z_{s+1}\right)} \end{bmatrix}\right), & z_l > z_s \\ \mathbf{M}_{0,l}\begin{bmatrix} 0 \\ B'^{-}_{0,\mathrm{TM}} \end{bmatrix}, & z_l < z_s \end{cases} \tag{7.11}$$

Finding the amplitudes of the electric field from the magnetic field amplitudes for extraordinary waves is also different from the TM case for an isotropic media. For the extraordinary wave you must now multiply the primed coefficients, representing the magnetic field amplitudes, by $\sqrt{\left(\gamma_{\mathrm{el}}/\varepsilon_{t,l}\right)^2+\left(\beta/\varepsilon_{z,l}\right)^2}\Big/\sqrt{\left(\gamma_{\mathrm{es}}/\varepsilon_{t,s}\right)^2+\left(\beta/\varepsilon_{z,s}\right)^2}$, which accounts for the difference between the magnetic field and electric field amplitudes in layers l and s, to find the amplitude of the electric fields for use Eq. (7.3). From the electric Green's function, the magnetic Green's function can be evaluated from the curl of the electric Green's function in the usual way, i.e. $\overline{\overline{\boldsymbol{\Gamma}}} = \nabla\times\overline{\overline{\mathbf{G}}}$.

Finally, in the heat flux calculation the dielectric function must be treated as a tensor in the fluctuation dissipation theory. The Poynting vector equation should be modified as follows

$$S_{i\times j}\left(\omega,\mathbf{r}\right) = \frac{k_0^2\Theta\left(\omega,T\right)}{2\pi^2}\mathrm{Re}\left[i\varepsilon''_{ll}\left(\omega\right)\int_0^\infty \beta\int_{z_s}^{z_{s+1}}\left(g_{il}h^*_{lj} - g_{jl}h^*_{li}\right)dz'd\beta\right] \tag{7.12}$$

which now accounts for the fact that the dielectric function is a diagonal tensor and not a constant ,with the addition of the tensor index ll to the imaginary part.

In the vacuum gap between two uniaxial anisotropic media, as shown in Fig. 7.2, the heat flux is given by Eq. (2.59), but the uniaxial Fresnel coefficients must be used.

This equation can be re-expressed in terms of the power transmission coefficient, ξ_j, after integrating over the frequency the heat flux in the z-direction, and is given by

$$Q_z = \frac{1}{4\pi^2}\int_0^\infty \left(\Theta(\omega,T_0)-\Theta(\omega,T_2)\right)d\omega\int_0^\infty \beta \sum_{j=s,p} \xi_j(\omega,\beta)d\beta \qquad (7.13)$$

where the j indicates the power transmission coefficient for either s or p polarization. The power transmission coefficient between two identical media, is given by

$$\xi_j(\omega,\beta) = \begin{Bmatrix} (1-\left|r_j\right|^2)^2 \Big/ \left|1-r_j^2 e^{2i\gamma_0 d}\right|^2, & \beta < k_0 \\ 4\left(\mathrm{Im}\left(r_j\right)\right)^2 e^{2i\gamma_0 d} \Big/ \left|1-r_j^2 e^{2i\gamma_0 d}\right|^2, & \beta > k_0 \end{Bmatrix} \qquad (7.14)$$

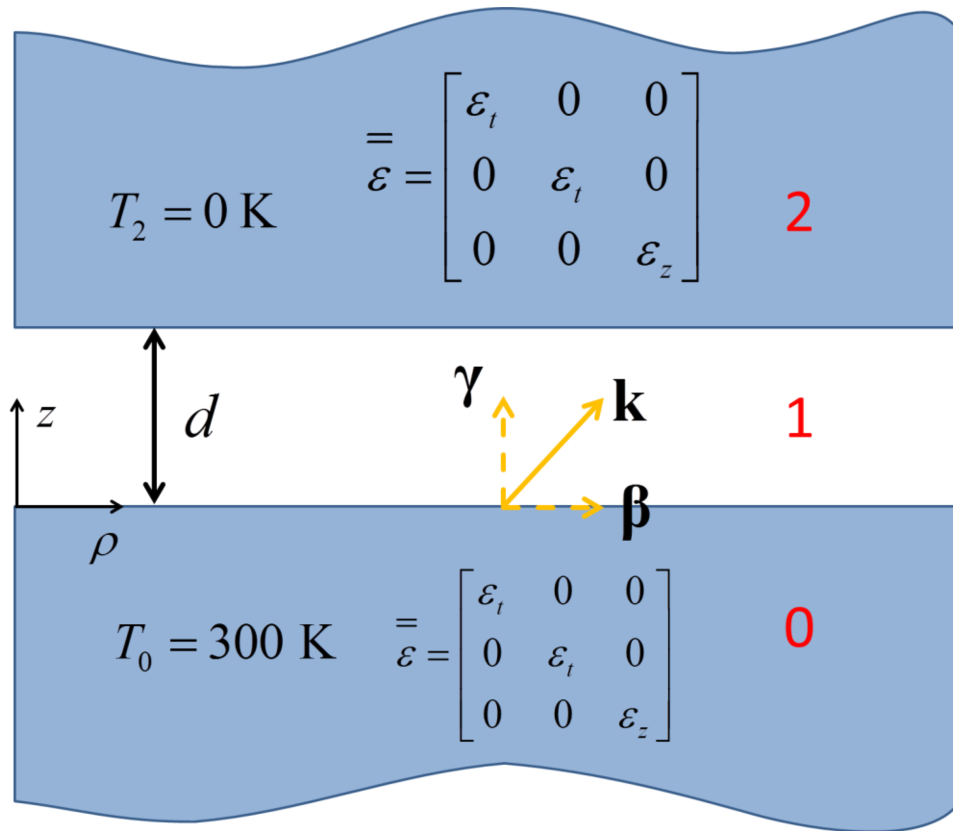

Figure 7.2 Geometry for two semi-infinite uniaxial anisotropic media used to represent two multilayer structures that are semi-infinite and can be represented by and effective medium with a dielectric tensor $\overline{\overline{\varepsilon}}$.

where r_j are the reflection coefficients for p and s polarization for the interface between the uniaxial media and the vacuum gap, using the anisotropic Fresnel coefficients from Eqs. (2.60)- (2.63). The z-component of the wavevector in vacuum is represented as γ_0 and is related to the radial component of the wavevector by $\gamma_0 = \sqrt{k_0^2 - \beta^2}$. When $\beta > k_0$ the waves become evanescent in the vacuum region, and only carry energy in the near-field. The power transmission coefficient of Eq. (7.14) has already been divided into the power transmission coefficient for propagating (top) and evanescent (bottom) waves in Eq. (7.14) .

7.2 Energy Streamlines in Near-Field Uniaxial Materials

Consider two semi-infinite multilayer structures consisting of alternating layers of "metal" and "dielectric" separated by a vacuum gap *d*, as shown in Fig. 7.3. It was mentioned in chapter 2 that the terms are interpreted rather loosely. In this case the "metal" layer will refer to either doped Si (D-Si) or SiC, which in fact has negative refraction due to phonon modes and not free electrons. The dielectric layer is Ge. For this section, the period of the layers is taken to be infinitely small but the ratio of the layers will remain fixed. Ultimately, if the period is infinitely small each slab can be represented as a homogenous effective medium with a uniaxial dielectric function as shown in Fig. 7.2. The temperature of each half space is indicated on the figure, one of the media is at 300 K and the other taken to be at 0 K, so that we are only concerned with the emission in one direction. We can determine the optical dispersion of the effective structure for TM (extraordinary waves) from the Eq. (2.36). We chose the metal volume filling fraction and materials such that there will be hyperbolic modes in the IR region.

The real part of the effective optical constants, determined from the EMT by Eqs. (2.33) and (2.34), for an effective medium of n-doped doped Si (D-Si) and Ge with a volume filling fraction of D-Si of 50%, is shown in Fig. 7.4 (a). The D-Si is taken to have

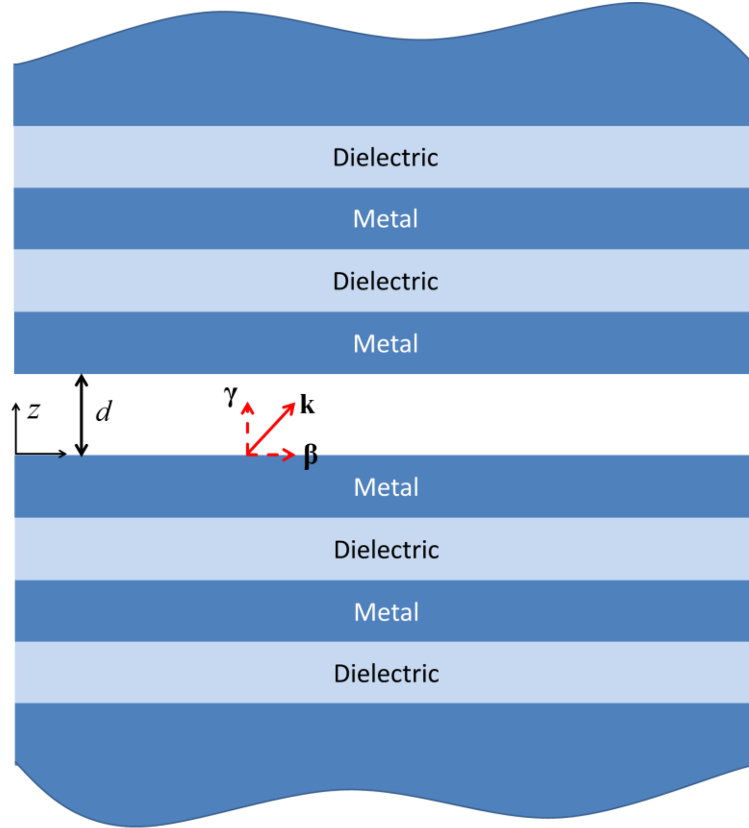

Figure 7.3 The structure under consideration consists of two infinitely repeating multilayer stacks of alternating "metal", either D-Si or SiC, which are not metal but exhibit negative refraction due to a free electron Drude term and a Restrahlen band, respectively. The "dielectric" layer is Ge which is approximated with a constant dielectric function.

doping concentration of $N = 10^{20}\ \text{cm}^{-1}$, and the optical constants of n-doped Si are calculated by the Drude model from the work by Basu on the optical properties of D-Si at room temperature [91]. Note that we used both slabs as having the room temperature properties, even though one of them is set to 0 K. Ge is taken to have a constant dielectric function in the region of interest, $\varepsilon_{\text{Ge}} = 16$. In Fig. 7.4 (b) the real part of the components of the dielectric tensor of an effective medium of SiC and Ge are shown, with a SiC volume filling fraction of 30%. The optical properties of SiC are the handbook values [90]. The inset of Fig. 7.4 shows two multilayer stacks, one of D-Si/Ge in (a) and SiC/Ge in (b), which are represented by the effective homogenized media. The two hyperbolic modes of the effective structure are indicated in blue (I) and red (II). Recall that type I

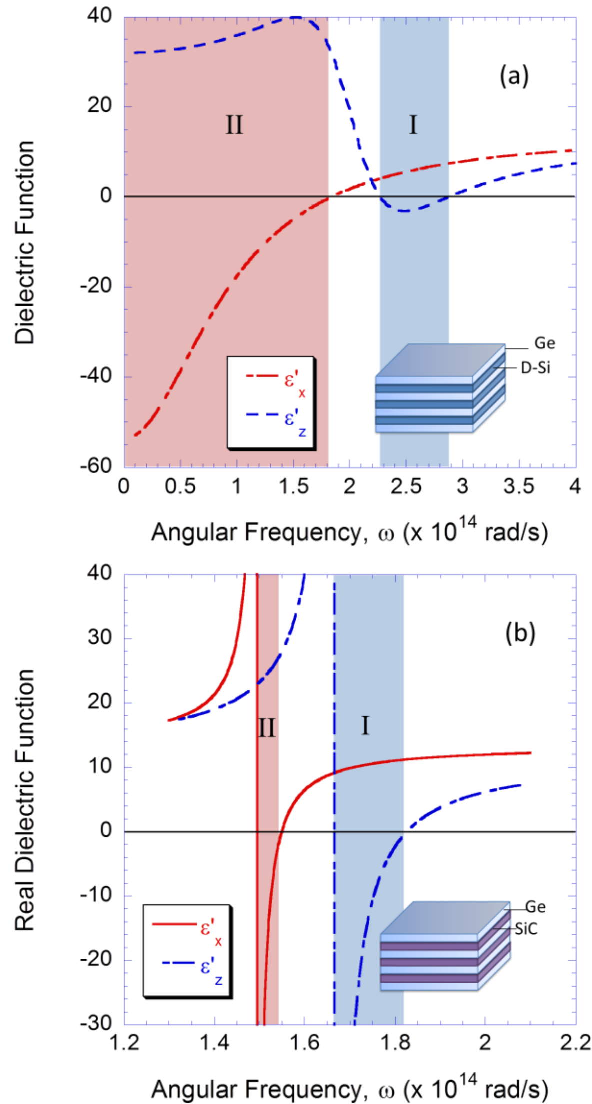

Figure 7.4 (a) Real part of the EMA dielectric function of doped Si and Ge with $f = 0.5$ (b) and for doped SiC and Ge with $f = 0.3$. The inset shows a schematic of the structure of interest.

exhibits negative refraction, or a bending backwards of the Poynting vector, whereas type II has a negative *z*-component of the wavevector inside of the medium. The hyperbolic bands in the D-Si are due to free electron absorption, and thus the type II band appears fairly broad because of the long wavelength free electron absorption in the D-Si. The hyperbolic modes of SiC are narrow by comparison, due to the fact that the hyperbolic modes are caused by a narrow phonon mode in the IR associated with the Restrahlen band of SiC [90].

Figure 7.5 shows the power transmittance of TM waves, ξ_{p}, as a function of wavevector and frequency for two semi-infinite D-Si/Ge (a) and two semi-infinite SiC/Ge (b) effective media, separated by a 10 nm vacuum gap. Note that the power transmission coefficient for the type II region, shown in Fig. 7.4 (a), is broad but is not nearly as high at large radial wavevectors like the peaks in SiC/Ge. Also note that D-Si/Ge only has a large power transmission in the type II region around the area where the z-component of the wavevector inside of the D-Si/Ge structure becomes zero. For smaller

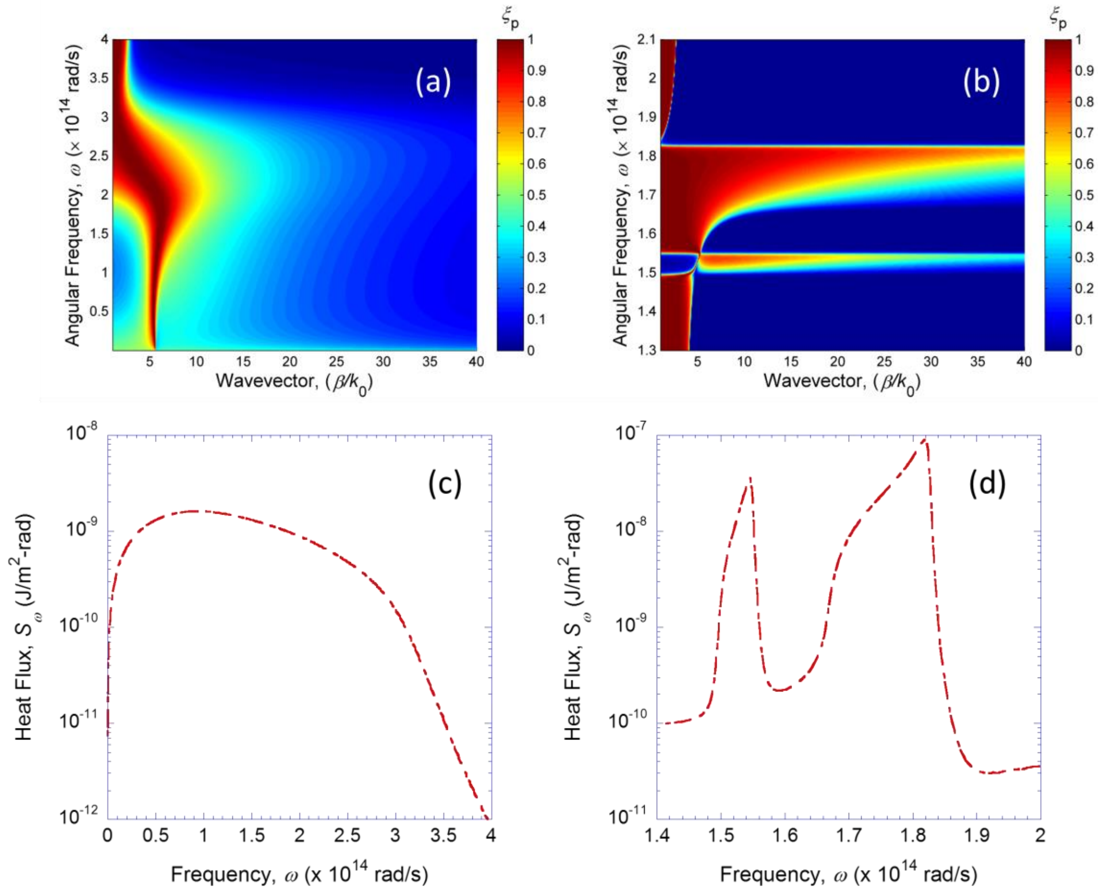

Figure 7.5 Power transmission coefficient between (a) two semi-infinite EMA structures of doped Si and Ge with $f = 0.5$ and a gap spacing of 10 nm, (b) between EMA structures of SiC and Ge with $f = 0.3$ and a gap spacing of 10 nm. (c) Spectral heat flux between two semi-infinite EMA structures of doped Si and Ge with $f = 0.5$ and a gap spacing of 10 nm, (d) two semi-infinite EMA structures of SiC and Ge with $f = 0.3$ and a gap spacing of 10 nm.

radial components of the wavevector around this location, the waves are forbidden by the band structure, and thus the power transmission coefficient is small. This same feature is observable in Fig. 7.5 (b) for SiC/Ge, the peaks are obviously sharper due to the sharpness of the phonon resonance that SiC has at $12\,\mu\text{m}$ [78]. Figures 7.5 (a) and (b) show the corresponding heat flux across the vacuum gap calculated from Eq. (7.13). In Fig. 7.5 (a) and (c) the broadness of the D-Si/Ge and the narrow feature of SiC/Ge are reinforced. The large peaks in SiC/Ge heat flux correspond the two hyperbolic bands.

In order to study the lateral displacement, several characteristic frequencies were selected in the region of interest 0.5×10^{14} - 3×10^{14} rad/s ($37 - 6$ μm). The chosen frequencies correspond to representative frequencies in the different dispersion regimes. For the D-Si/Ge structure two of the chosen frequencies are 0.5×10^{14} rad/s and 1×10^{14} rad/s, and fall in the type II hyperbolic region. The third frequency, 1.8×10^{14} rad/s, has an ε_x' that is near-zero. The fourth frequency of choice, 2.7×10^{14} rad/s, falls in the type I hyperbolic region and thus we expect this frequency to exhibit negative refraction. The fifth and final frequency for the D-Si/Ge effective medium is 2.9×10^{14} which has ε_z' that is near zero. These frequencies were chosen because they will have different and unique energy propagation characteristics. Figure 7.6 shows the heat flux evaluated as several of these frequencies as a function of the lateral component of the wavevector normalized by the vacuum wavevector magnitude for the D-Si/Ge structure. The normalized lateral wavevector is defined as

$$\beta^* = \frac{\beta}{k_0} \tag{7.15}$$

When the critical wavevector is larger than 1 the waves in the vacuum region will be purely evanescent. Some of the curves (type II hyperbolic modes) show a sharp peak in the curve at the critical wavevector, defined as

$$\beta_c = k_e \tag{7.16}$$

where the lateral component of the wavevector is equal to the extraordinary wavevector magnitude. At this critical wavevector there is a sharp decrease in the imaginary part of the z-component of the wavevector for some frequencies. The critical wavevector can be

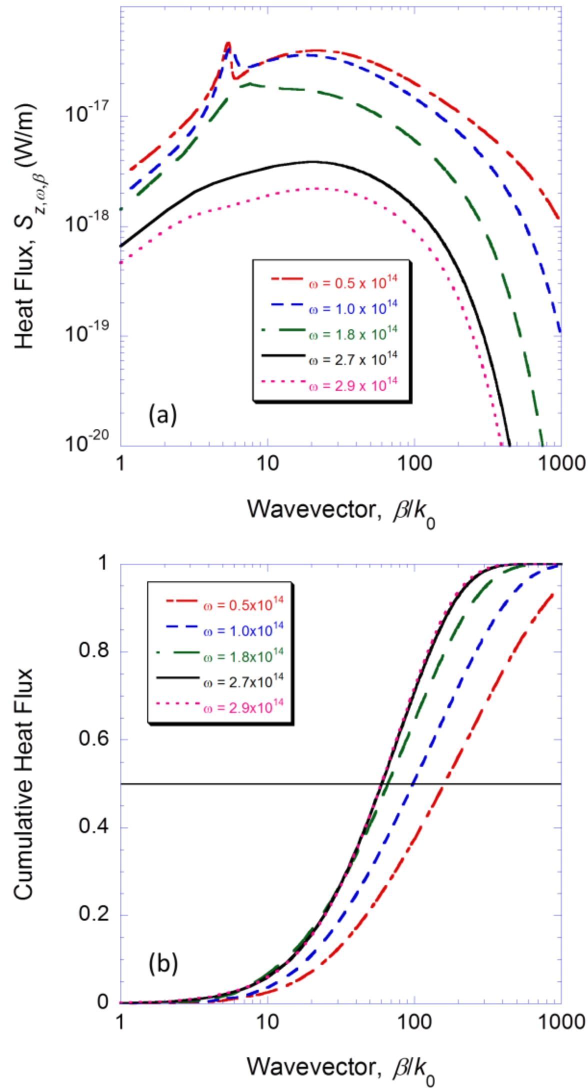

Figure 7.6 (a) Heat flux per unit frequency per unit wavevector versus the normalized wavevector at four select frequencies for D-Si/Ge multilayer $f = 0.5$. (b) Integration of the total heat flux over the wavevector space. The horizontal line shows where 50% of the heat flux falls above and below the median wavevector for each frequency.

seen clearly in Fig. 7.5 (a) from the contour plot around as the narrow red strip at the type II region. The power transmittance factor increases sharply because the lateral wavevector becomes large enough to satisfy the dispersion, i.e. when β becomes equal to the critical value. Comparison with the cumulative heat flux shows that there is only a small amount of energy contributed by smaller wavevectors. The median wavevector, the wavevector at which half of the energy is contribute by smaller, and half by larger wavevectors, is indicated by the crossing of the cumulative curve with the horizontal black 50% line.

The same diagram for the SiC/Ge effective medium is presented in Fig. 7.7 (a) and (b). The heat flux at several frequencies is shown in (a); the frequencies are listed in the legend of the figure. Only three typical frequencies are chosen since SiC has a much narrower spectral region where the heat flux is high, as was shown in Fig. 7.5 (d). Two of the frequencies, 1.82×10^{14} and 1.54×10^{14} rad/s, fall in the type I and II region, respectively. The third frequency, 1.59×10^{14} rad/s, is an elliptical mode that lies in between the two bands in a region where the spectral heat flux is much smaller. The sudden drop in heat flux at 1.59 [10^{-14} rad/s] corresponds to the lateral component of the wavevector moving beyond the dispersion ellipse, since there are no hyperbolic or surface modes supported at this frequency the heat flux drops significantly. At smaller lateral wavevectors the SiC/Ge structure is more optically dense than air and has some propagating modes at this frequency that fall within the dispersion ellipse when $\beta^* > 1$. For the type II modes there is always a forbidden band inside of the hyperbola, this is why the heat flux remains small below the critical wavevector, β_c. For the type I modes there is no forbidden band and the heat flux increases continuously beyond the critical wavevector β_c. The cumulative heat flux of Fig. 7.7 (b) is similar to the cumulative heat flux plot for D-Si/Ge, and again shows the 50% line to indicate the median wavevectors above and below which 50% of the heat is transferred. The most noticeable difference

from the D-Si/Ge curves is the shape of the cumulative heat flux for the elliptical mode, which still has a significant contribution from modes that are evanescent in the vacuum but propagating in the SiC/Ge structure because it is more optical dense than the vacuum region. About 15% of the radiation at this frequency is still attributed to non-propagating

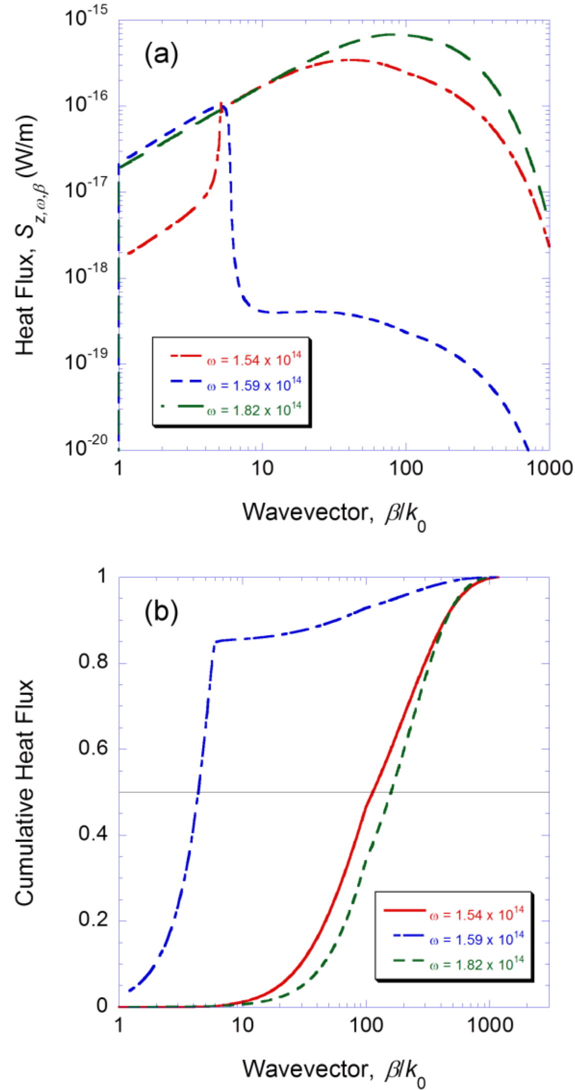

Figure 7.7 Heat flux per unit frequency per unit wavevector versus the normalized wavevector at four select frequencies for SiC/Ge multilayer $f = 0.3$. (b) Integration of the total heat flux over the wavevector space. The horizontal line shows where 50% of the heat flux falls above and below the median wavevector for each frequency.

modes, and it is more spread out over a larger range of wavevectors. This explains the strange and sudden decrease in the slope of the cumulative curve for this frequency.

The penetration depth of each of the chosen frequencies for the D-Si/Ge structure is shown in Fig. 7.8. The penetration depth is found from the z-component of the wavevector, e.g. extraordinary waves according to

$$\delta_{\mathrm{p}} = \frac{1}{2\gamma_e''} \tag{7.17}$$

A sharp peak in some of the curves corresponds to the same critical wavevector mentioned earlier, where the imaginary part of the z-component of the wavevector becomes small so that the penetration depth becomes relatively large at that particular wavevector. For large lateral wavevector components the distance that energy might travel in the medium may be very large because the slab acts as a waveguide, but since the medium is not without losses a large lateral displacement in the medium will result in a smaller penetration depth in the z-direction into the medium. In order to get characteristic z-dimension of the D-Si/Ge structure we define an average penetration depth according to the equation

$$\delta_{\omega,j} = \frac{\int_0^\infty \beta\xi_j\delta_j d\beta}{\int_0^\infty \beta\xi_j d\beta} \tag{7.18}$$

where j is either s or p polarization. The average penetration depth as a function of wavelength is plotted in Fig. 7.8 (b). In Fig. 7.8 (a), it is clear that the power penetration depth remains small for the type II modes below the critical wavevector ($\beta < \beta_{\mathrm{c}}$), where there are no supported modes. The penetration depth increases sharply at the critical value. It will eventually decrease linearly for all modes, since at large β the power penetration depth is $\delta_{\mathrm{e}} = |\varepsilon_z| \Big/ \left(2\beta \,\mathrm{Re}\left[\sqrt{\varepsilon_x \varepsilon_z^*}\right]\right)$. This penetration depth for uniaxial media is different from the isotropic penetration depth, which is given by $\delta = 1/(2\beta)$

[75]. In theory, the penetration depth could be infinite for a hyperbolic media because of the opposite sign of the dielectric functions associated hyperbolic modes, but this is only if the dielectric functions were purely real. However, for real materials a small amount of loss will result in a small penetration depth for the very large β associated with small gap spacings. For type I modes there exists no critical wavevector, because the mode has no forbidden band, and the penetration depth simply decreases at

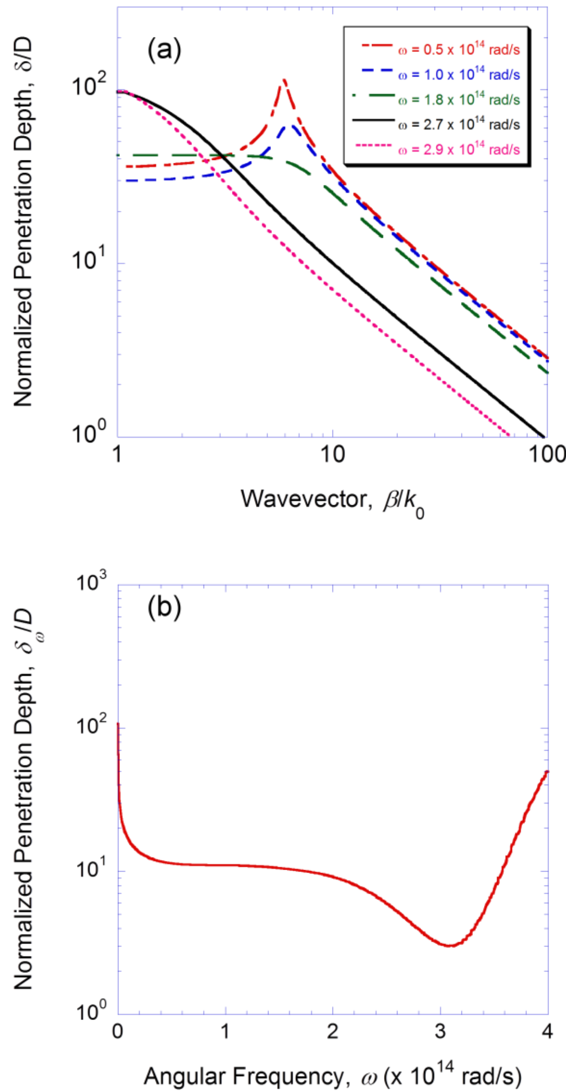

Figure 7.8 (a) Normalized penetration depth of D-Si/Ge multilayer $f = 0.5$ with a gap spacing of 10 nm at select frequencies. (b) Normalized average penetration depth of Si/Ge multilayer $f = 0.5$ with a gap spacing of 10 nm.

higher β. The ENZ mode has a nearly constant penetration depth at smaller β, but decreases at larger values. Finding the median β from Fig. 7.6 (b), and comparing the average penetration depth integrated over all wavevectors with the penetration depths from Fig. 7.8 (a) at this wavevector, one may note that the values are very similar in magnitude.

The penetration depth diagram presented in Fig. 7.9 is for the SiC/Ge structure. The penetration depth curves are consistent with those of D-Si/Ge since for the type II mode (1.54×10^{14} rad/s) is forbidden below the critical wavevector, and then spikes at the critical wavevector. The type I mode (1.82×10^{14} rad/s) has a penetration depth that decays continuously. Finally, for the elliptical mode (1.54×10^{14} rad/s), there are some propagating modes when $1 < \beta^* < \beta_c$. Since the SiC/Ge is optically denser than vacuum these modes are still propagating inside of the medium, but they are evanescent in the vacuum. However, a β beyond the critical value falls outside the dispersion ellipse, where there are no propagating modes, and the penetration depth falls significantly at larger wavevectors. Recall that at large β all the curves decrease linearly as in Fig. 7.8, since $\gamma''_e \approx \mathrm{Re}\left[\sqrt{\varepsilon_z \varepsilon_t}\right]\beta / |\varepsilon_z|$ [75]. The two hyperbolic modes have been chosen to correspond to the peak spectral heat fluxes in each region. At these frequencies more energy is carried by large lateral wavevectors, and the average penetration depth drops sharply at these locations, as shown in Fig. 7.9 (b). The penetration depth is still relatively large in parts of the hyperbolic medium as high as 10-100$\times$ the vacuum gap size of 10 nm.

Observing the energy streamlines for these characteristic frequencies at the median wavevector, we can estimate how large the lateral shift of energy is. This is an estimate of the other characteristic dimension of the structure, the lateral dimension, which is important for the validity of the 1D approximation of the Green's function. Using Eq. (7.12) to find the components of the time average Poynting vector in the *z*-

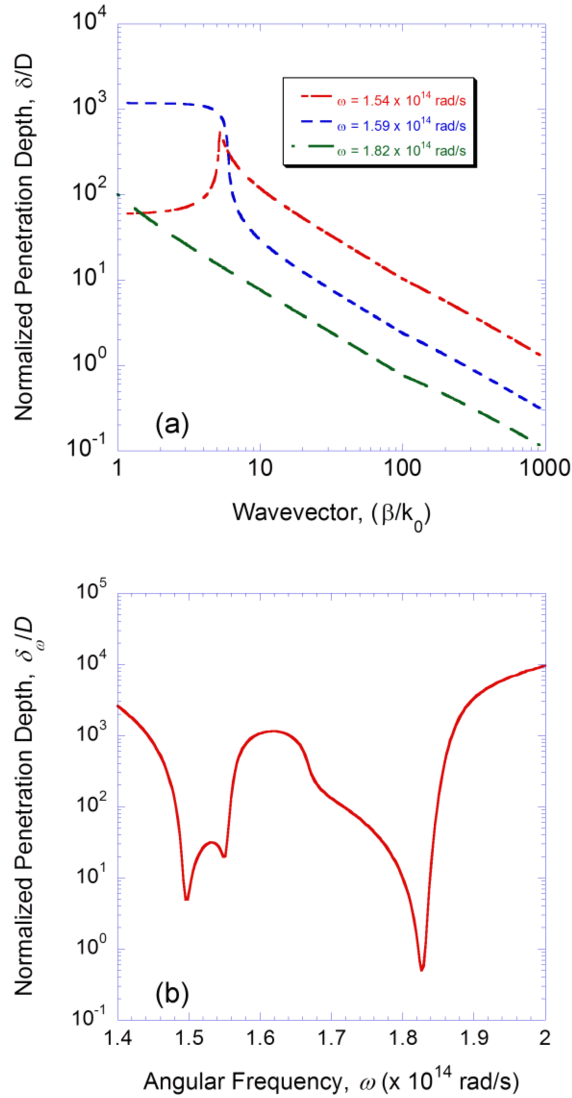

Figure 7.9 (a) Normalized penetration depth of SiC/Ge multilayer $f = 0.3$ with a gap spacing of 10 nm at select frequencies. (b) Normalized average penetration depth of SiC/Ge multilayer $f = 0.3$ with a gap spacing of 10 nm.

direction and in the radial direction, $\langle \mathbf{S}_z \rangle$ and $\langle \mathbf{S}_r \rangle$, the net heat flux in the normal and lateral directions can be determined. The energy streamlines are evaluated by tracing the slope from Eq. (2.67). The energy streamlines are shown at several different frequencies for D-Si/Ge in Fig. 7.10. From Fig. 7.10 (a) we can observe the streamlines of first three frequencies, which are listed in the legend, along with the chosen (median) wavevector of the streamline. The lateral displacement for each of these streamlines at two penetration

depths inside of the source medium (bottom) are 194, 23, and 3.72 times the vacuum gap distance for the frequencies 1.8, 2.7 and 2.9 [10^{-14} rad/s], respectively. The last frequency is an ENZ mode and thus has a small lateral displacement. Note that the first and second frequencies are not plotted all the way to two penetration depths in the figure. The type I mode (2.9 [10^{-14} rad/s]) undergoes a negative refraction (the wavevector points left which is negative), which can be seen clearly from the figure. In order to facilitate heat transfer from these modes the lateral dimensions of the structure must be much larger than the

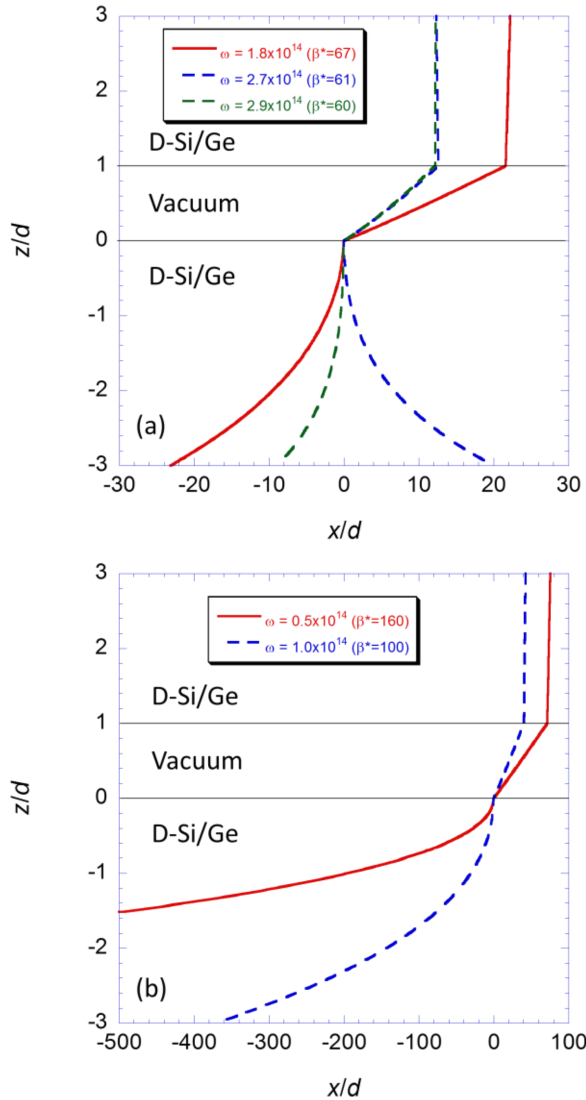

Figure 7.10 (a) and (b) energy streamlines for median normalized wavevector at different select frequencies in D-Si/Ge multilayer structure with $f = 0.5$ at 10 nm gap spacing

combined lateral displacement in the source layer and vacuum. Usually, the lateral displacement will be largest inside of the source layer, but this will not always be the case, especially for an ENZ mode. Figure 7.10 (b) shows the energy streamlines at two other frequencies as indicated in the figure legend, the total lateral displacement inside of the source layer at two times the penetration depth are 3728 and 1604 times the vacuum gap for the frequencies 0.5 and 1 [10^{-14} rad/s], respectively. This indicates that inside of these medium the lateral displacements can be extremely large when compared to the penetration depths of Figs. 7.8 and 7.9.

Similar results are shown for the energy streamlines of the SiC/Ge structure in Fig. 7.11(a) and (b). In (a) the energy streamlines have an overall lateral displacement of 321 and 99 times the vacuum gap at two penetration depths inside of the medium for 1.54 and 1.82 [10^{-14} rad/s], respectively. The penetration depth of the 1.54 [10^{-14} rad/s] frequency is large compared to the others, so it appears to have a relatively small curvature until the depth inside of the medium gets very large, where it does eventually curve significantly (not shown in the figure). The 1.82 [10^{-14} rad/s] frequency streamline shows the negative refraction in the type I hyperbolic mode, as the direction of lateral displacement is in the opposite direction of the lateral wavevector (which when positive points right in the figure). Fig 7.11 (b) shows the 1.59 [10^{-14} rad/s] energy streamline. The overall lateral displacement at two penetration depths inside of the medium is 4001 times the vacuum gap spacing. However, this frequency does not carry as much energy as the other two, and is therefore less important.

The choice of using two penetration depths to represent the lateral displacement is because beyond two penetration depths only approximately 14% of the energy flux remains in the z-direction. Energy streamlines will begin to show a larger curvature as the z-component of the heat flux becomes zero. For this reason we do not care about the large lateral displacements when the z-component of the heat flux has become negligible since the energy streamlines are not carrying as much forward energy. Should the streamlines

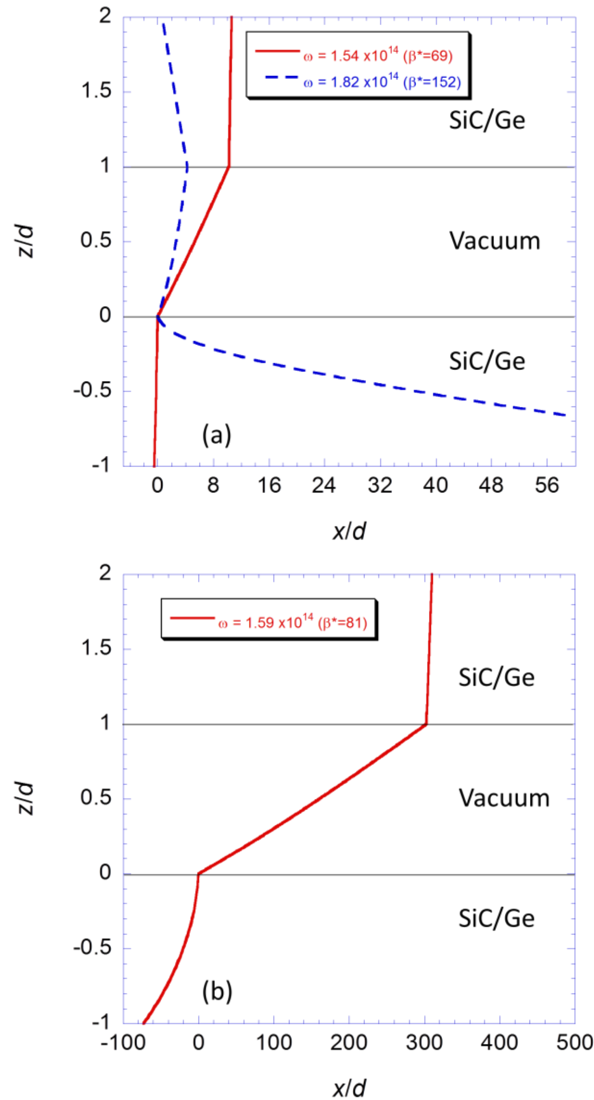

Figure 7.11 (a) and (b) energy streamlines for median normalized wavevector at different select frequencies in SiC/Ge multilayer structure with $f = 0.3$ at 10 nm gap spacing.

become truncated by the finite structure of a real MDPC at a larger depth the energy reduction would not be as significant, (e.g. at 3 penetration depths very little energy is being carried in the z-direction). It is the z-component of heat flux that is important for engineering applications, thus the energy averages of the variables are computed with a weight based on this component. For most variables of interest, the average and median value are usually similar in magnitude (as observed with the penetration depth). It is therefore expected that the values reported for the lateral displacement inside of the

source layer from the streamline of the median β will be a good representation of the average lateral displacement in the source layer.

The energy average lateral displacement inside of the vacuum gap can be calculated from the energy streamlines. At each lateral wavevector component the lateral displacement for polarization j is defined as

$$\Delta_j = r(0) - r(d) \tag{7.19}$$

where $r(0)$ is the radial location the streamline has at the first interface between the emitter and the vacuum gap, which is defined to be the origin, and $r(d)$ is the lateral dimension it has at the second interface between the vacuum gap and the receiver. The energy average lateral displacement across the vacuum gap is then calculated from

$$\Delta_{\omega,j} = \frac{\int_0^\infty \beta \xi_j \Delta_j d\beta}{\int_0^\infty \beta \xi_j d\beta} \tag{7.20}$$

This gives the characteristic lateral shift in energy across the vacuum gap.

The energy averaged lateral displacement across the vacuum gap is plotted in Fig. 7.12 (a) for the D-Si/Ge structure. The lateral displacement in the vacuum gap is lower when the power transmission coefficient is large. The majority of the heat flux at 10 nm in the vacuum layer is purely evanescent. While the electric field is reflected and refracted according to complex Snell's law [78], the energy streamlines are refracted according to different rules [73,130], and the direction of energy propagation is not simply coincident with the wavevector. If the transmission is large there is a large $\langle \mathbf{S}_z \rangle$ relative to $\langle \mathbf{S}_r \rangle$ and the vacuum lateral displacement is actually lower, as in the hyperbolic region where the power transmission coefficient is clearly much larger despite the large lateral component of the wavevector. However, the vacuum lateral displacement may still remain 10 times larger, or more, than the gap separation distance. Figure 7.12

(b) shows the lateral displacement for the SiC/Ge structure, where the large transmission coefficient regions are actually dips in the lateral displacement across the vacuum gap. For the most important spectral regions, it is likely that the critical lateral dimensions of the structure are determined by the lateral displacement of the streamlines in the source layer rather than inside of the vacuum gap.

In general, the large lateral displacement inside of the media can be hundreds, or even thousands of times the vacuum gap at 10 nm. For any near-field MDPC structure to

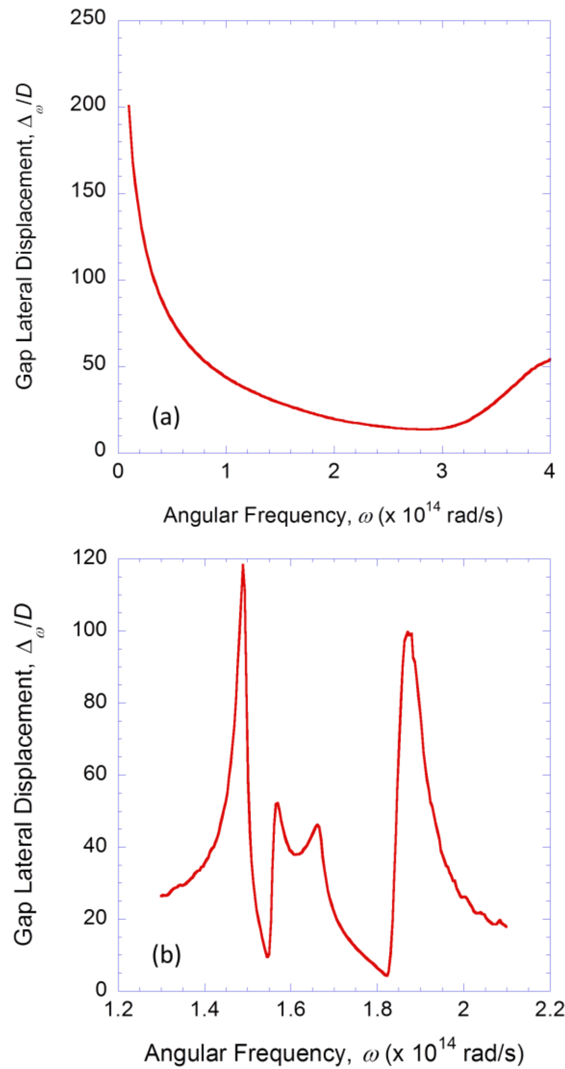

Figure 7.12 Average lateral gap displacement for (a) D-Si/Ge structure with $f = 0.5$ at 10 nm gap spacing and (b) for SiC/Ge with $f = 0.3$ at 10 nm gap spacing.

be considered one dimensional, the structure should be at least one or more orders magnitude larger than the typical characteristic lateral dimension calculated from the energy streamlines. A very conservative estimate, based on the lateral displacements of some of the typical streamlines in this work, would be that the lateral of the structures of interest should be larger than 100 μm with a 10 nm gap. It may become important to consider 3D effects for smaller lateral structures and the validity of the 1D model should be confirmed first. Under these conditions, a 1D model may provide an incorrect estimate of the energy flux. This characteristic lateral dimension will vary from structure to structure, and will be smaller with a larger gap spacing, but the reported lateral dimension is probably reasonable for most cases involving MDPCs with hyperbolic modes at 10 nm gap spacing.

In the following section the validity of the energy streamlines when the period is not infinitely small is briefly considered in a far-field MDPC structure. It is shown that the energy streamlines may vary significantly even when the period is much smaller than the projected wavelength.

7.3 Validity of EMA Energy Streamlines in Far-Field Uniaxial Anisotropic Materials

In order to compare the energy streamlines in an effective medium and the true multilayer structure, the ESLs of a steady plane wave of light in structures with 30 layers of 20 nm thickness, 300 layers of 2 nm thickness, and a 600 nm thick EMA slab are shown in Fig. 7.13. The layers are an alternating dielectric with a constant dielectric function of $\varepsilon = 16$ and Ag approximated as a Drude model with $\omega_{p,0} = 1.39\times10^{-6}$ rad/s and $\gamma_0 = 2.7 \times 10^{13}$ rad/s. The incidence angle in the Fig. 7.13 (a)-(b) is 60 degrees from the surface normal and the selected wavelengths of light are 400 nm, 593.7 nm, and 800 nm. The x and y axis are normalized by the thickness of the entire structure, D, which is 600 nm.

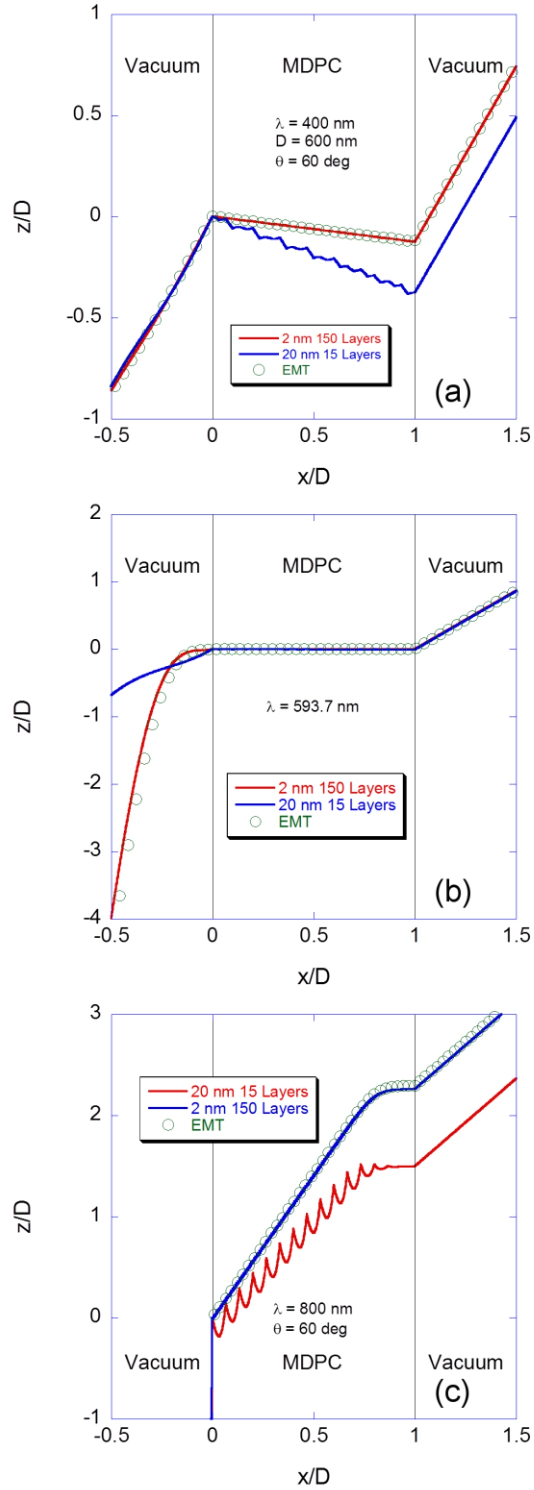

Figure 7.13 ESLs for positive refraction at an incidence angle of 60° for the uniaxial effective medium and multilayer structures with 300 and 30 layers of the same total thickness, *d* in (a) Negative refraction (type I) regime, (b) Epsilon near zero regime, and (c) Positive refraction regime.

Negative refraction of the ESLs can be seen in Fig. 7.13 (a). For the case of the EMA slab and the 300 layer structure the ESLs are shown to be almost exactly the same, while the transmittance of the EMA model and 300 layered structure is 0.89 for both, the relative difference being less than 1%. While for the case of the 30 layer structure the ESLs have extra lateral displacement for the TMM solution. The transmittance, however, agrees quite well still with a 4% difference (0.89 vs. 0.85). This means that in terms of the optical properties EMA still works well, but the focusing properties of the media will be affected significantly, since the net flow of energy will be diffracted differently in the 30 layer structure within the individual layers. The overall result is still negative refraction, but the negative bending in the metallic layers and the positive refraction in the dielectric layers is obvious. The 30 layer structure with 20 nm is beginning to show cavity effects in the streamlines, while the 300 layer structure is a waveguide with very little diffraction [131]. This is confirmed in the agreement between the ESLs, because of the lack of diffraction within the slab it is reasonable to expect that the ESL can be used to calculate a pseudo-image that would be useful for determining the lensing properties of the structure. However, if the transmission is low the reflection at the front surface must be considered, as it distorts the ESLs by adding in some additional lateral displacement. Fortunately a lens with a low transmittance is usually not a good lens, and therefore it is expected that a good lenses will have nice smooth energy streamlines that reflect the true image of a source. Complications begin to arise when the layers are thick, as illustrated by the energy streamlines; a calculation of a Gaussian beam or point source image should be used to confirm the agreement. When the energy streamlines in the actual structure do not match the streamlines for the EMA, the EMA should not be used for the image calculation.

The second case, shown in Fig. 7.13(b), is a nearly zero refraction of the incident light, which is similar to super-guiding [132]. In this case, however, the transmitted energy is quite low and the reflectance is quite high. In the EMA and 300 layer structure

the resulting streamlines are similar. In the 30 layer structure the negative refraction and positive refraction in individual layers is noticeable, but the ESLs balance each other in their lateral displacement so that the net effect is almost no lateral displacement. For reference, the reflectance of the structures is 0.98 for all three cases (less than 1% difference in all conditions). The agreement in lateral displacement is also good since all structures result in near zero displacement, but the structure is less useful in imaging application because the transmittance is small.

The third case, shown in Fig. 7.13 (c), is normal refraction. The transmittance is again low, 0.016 for the EMA, 0.018 for the 300 layer structure, and 0.009 for the 30 layer structure, as expected outside of the propagation band of the MDPC structure. However, the EMA and 300 layer structure have close reflectance values of 0.71 and 0.70, respectively. For the 300 layer case, the choice of first or last layer will not matter, because the structure will be in the EMA regime. However, for the 30 layer structure the choice to make the first layer metallic or dielectric will cause disparity in the optical properties, because a dielectric first layer can have an anti-reflection effect. Since at this wavelength we do not fall in the wave-guiding regime, it means more light can be absorbed, and the reflectance may be lower than what is predicted by EMA. In our case the reflectance is only 0.26 for the 30 layer structure, and a significant amount of energy is lost.

The limitations of EMA in predicting the properties of multilayer structures have been discussed in Refs. [82,83], when considered large lateral wavevectors or structures with larger periods one must also considered whether or not the energy streamlines will actually agree between the EMA and the exact TMM. In many cases where the heat flux or transmission and reflection are accurately predicted, the lateral displacement and foci of the energy streamline may still have significant differences.

CHAPTER 8

CONCLUSIONS AND RECOMMENDATIONS

This dissertation is divided into three main contributions. Firstly, it has conducted an experimental investigation of the optical constants of two dielectric film materials Ta_2O_5 and HfO_2 in from the FIR to the NIR region of the spectrum. It is intended that these material properties will provide useful for modeling infrared devices for use in near-field applications such as thermophotovoltaic cells. The second part is a parametric study of an $In_{0.18}Ga_{0.82}Sb$ near-field TPV cell. Finally, the third part is a study of energy flow in MDPC structures. The three parts of this study will facilitate the use of MDPC structures in TPV and other near-field applications as well as the use of the high temperature dielectric materials Ta_2O_5 and HfO_2 in near-field devices and MDPCs.

In part one of this dissertation Hafnia, films of thicknesses from about 180 to 500 nm were deposited using magnetron sputtering onto Si substrates and analyzed with XRD, AFM, SE, and FTIR spectrometry. The results indicate that the films are polycrystalline as deposited. Their annealing at 800 ^{o}C has little effect on the crystallinity and optical properties. A Cauchy dispersion was developed based on the SE data for 370 nm $\leq \lambda \leq$ 1000 nm and a single-oscillator model was developed for 1.25 μm $< \lambda <$ 20 μm based on NIR/MIR spectrometry data. The film thicknesses obtained from the two methods are in good agreement. Furthermore, the roughness obtained from fitting SE data is about twice the RMS roughness obtained from AFM. In general, thicker films possess rougher surfaces but the RMS roughness from AFM is no more than 7.2 nm. The FIR spectra are analyzed to elucidate phonon absorption. The combination of the Cauchy formula with the multiple Lorentz oscillators allowed development of a dielectric function of HfO_2 for the wavelength region from 370 nm to 500 μm. The results from this study help gain a better understanding of the optical and radiative properties of HfO_2

films for a number of optical and infrared device applications, from thermal control to energy harvesting.

The dielectric functions are then obtained for amorphous and nanocrystalline thin film samples of Ta_2O_5 deposited by magnetron sputtering. These sputtered films are smooth and of good structural quality and uniform thickness. Samples are amorphous as deposited at the substrate temperature used during deposition. Upon annealing at 800 °C, the samples become nanocrystalline with an orthorhombic phase being dominant. This induces a drastic change in the far-IR optical properties of the film. The low-frequency phonon modes become much sharper in the nanocrystalline samples. The frequencies of the effective phonon modes are determined by a line-shape analysis to quantitatively show the optical phonons in sputtered Ta_2O_5 films. Thermal stresses in the thicker samples after annealing were significant enough to cause cracking and the effect contributes to volume scattering in the sample thus affecting the near-IR transmittance. A simple model is introduced to account for the volumetric scattering in the thin film samples.

The second part investigates the performance of a TPV cell with a backside reflector (mirror) and under different surface preparation conditions. Based on the parametric study of $In_{0.18}Ga_{0.82}Sb$ cells, it is shown that a mirror or filter to reduce sub-bandgap radiation is an essential component with efficiency improvements as high as 35% at a lower emitter temperature of 1250 K. Furthermore, reducing the surface recombination velocity below a certain critical value changes the efficiency trend such that the efficiency would increase with decreasing gap spacing. This finding should make near-field TPV systems more appealing. Furthermore, decreasing the top p-layer thickness can improve performance by reducing diffusion losses. Because of the small penetration depth, it is important to investigate methods of surface passivation that are compatible with near-field heat transfer and that will not adversely affect the heat transfer rates associated with the near-field enhancement. This work has conducted a quantitative

study of the important parameters limiting the performance of a simple near-field TPV cell, which would facilitate the realization of near-field TPV systems for practical applications.

Finally, in the third part of this dissertation the lateral displacement of energy and penetration depth of MDPCs was studied for two potential IR device MDPCs made of alternating layers of doped Si and Ge and another of alternating layers SiC and Ge. The MDPCs are treated as a homogenized medium using the effective medium theory. It is shown that the lateral displacement can be 100's or 1000's of times the gap spacing in the near-field using a gap spacing of 10 nm. To be sure that a structure will behave as a one dimensional structure it is recommended that lateral dimensions of at least 100 μm be used to ensure that the heat flux will be close to the 1D limit. Should smaller lateral dimensions be required some 3D modeling may be necessary to confirm that the limited geometry does not limit the heat transfer between structures. Additionally, it was shown that despite the layer thickness and period being smaller than the wavelength of incident light energy streamlines in an effective medium and the actual medium may not agree perfectly, even when the properties of the medium such as transmission and reflection may agree quite well. Further study of the difference between energy propagation in homogenized and structures with finite periods by the energy streamline method may be of interest in area of near-field imaging.

This dissertation has enhanced the understanding of near-field heat transfer in anisotropic structures and the performance of near-field TPV cells. It is hoped that the material properties of HfO_2 and Ta_2O_5 will be used in the future to model MDPC devices for high temperature applications. These MDPCs may then be included in studies on the efficiency enhancement by acting as emitters/filters with tunable hyperbolic bands that can be used to simultaneously enhance near-field heat transfer and further improve the efficiency of near-field devices. It has been shown that once the surface recombination issue has been suitably addressed, the potential for near-field TPVs coupled with MDPCs

and other novel structures will be more promising than ever. Additionally, it is hoped that the concept of near-field energy streamlines in MDPCs will provide useful information for design of near-field devices as well as imaging systems.

APPENDIX A

XPS DATA AND ANALYSIS

The XPS data has been corrected for the presence of SiO_2 by isolating the Ta_2O_5 and SiO_2 contributions to the O 1s peak, shown in Fig. A.1. Only the Tantalum oxide portion is used in the ratio calculation. The ratio of O:Ta for the unannealed samples is 3.5 with the stage at room temperature, and 3.0 when the XPS stage has been held at 200 °C for 1 hr. For the annealed samples, the ratio is 3.2 and 2.9 for the sample stage at room

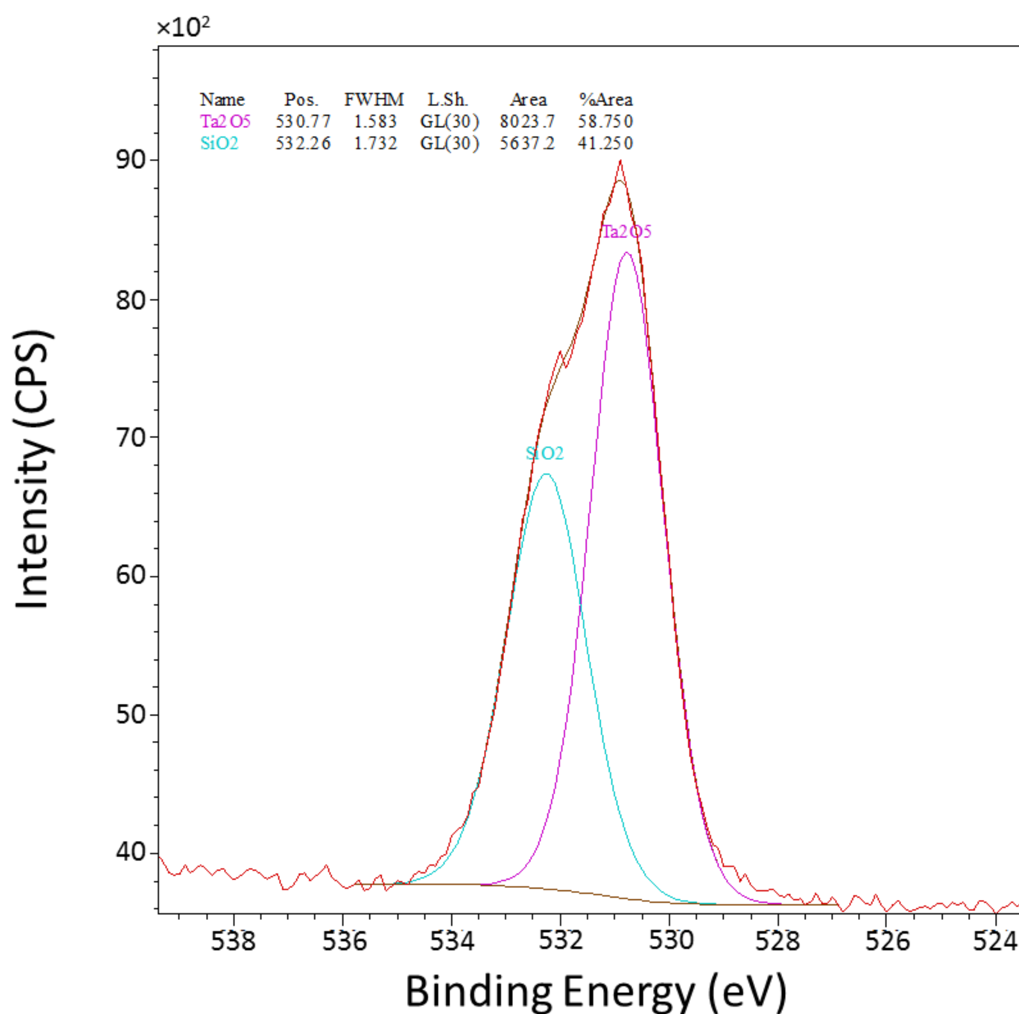

Figure A.1 XPS curves for an unannealed sample showing the O 1s peak. The SiO_2 peak is used to correct the Ta:O ratio.

temperature and after the sample stage is held at 200 °C for 1 hr, respectively. The O:Ta atom ratios are much closer to what is expected for Ta_2O_5. It is unlikely that there is any chemical composition with more oxygen than the stoichiometric ratio of 2:5, the remaining O is likely due to O that accompanies adventitious carbon contamination. It is possible to sputter away the carbon contamination layer in the XPS system, however for compounds such as Ta_2O_5, this approach often gives erroneous results as the oxygen

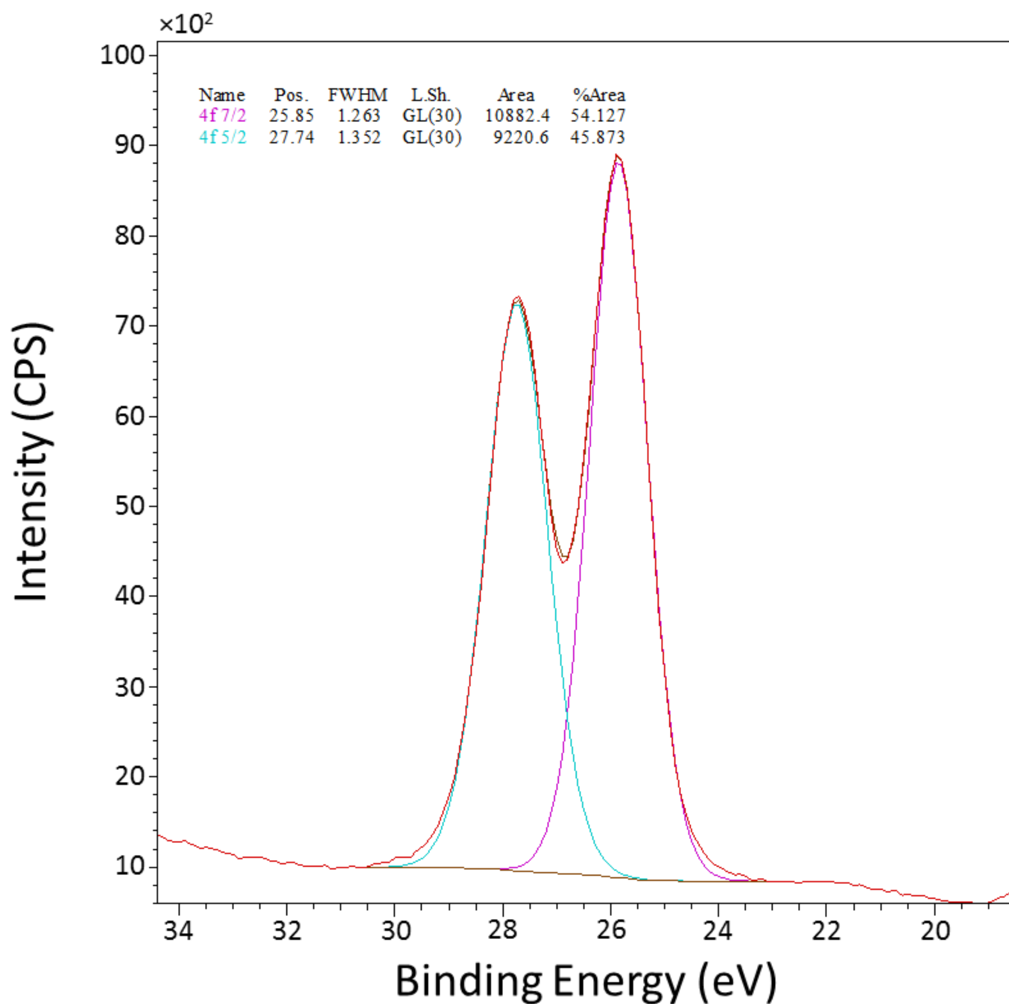

Figure A.2 XPS curves for an annealed Ta_2O_5 sample showing the Ta 4f peak. Note the peak location of 25.85 is consistent with the peak location from literature (26-27 ev).

sputters at a higher rate than the tantalum, suggesting a reduced oxygen content. A better approach is to examine the Ta peak positions, which are correlated to the oxidation state.

According to the NIST XPS database [133], for Ta metal the Ta 4f 7/3 peak would be around 22 eV, while for Ta_2O_5 the peak should fall between 26 and 27 eV. The Ta 4f 7/3 peak position observed in Figs. A.2 and A.3, for annealed and unannealed samples respectively, is as expected for nearly stoichiometric Ta_2O_5.

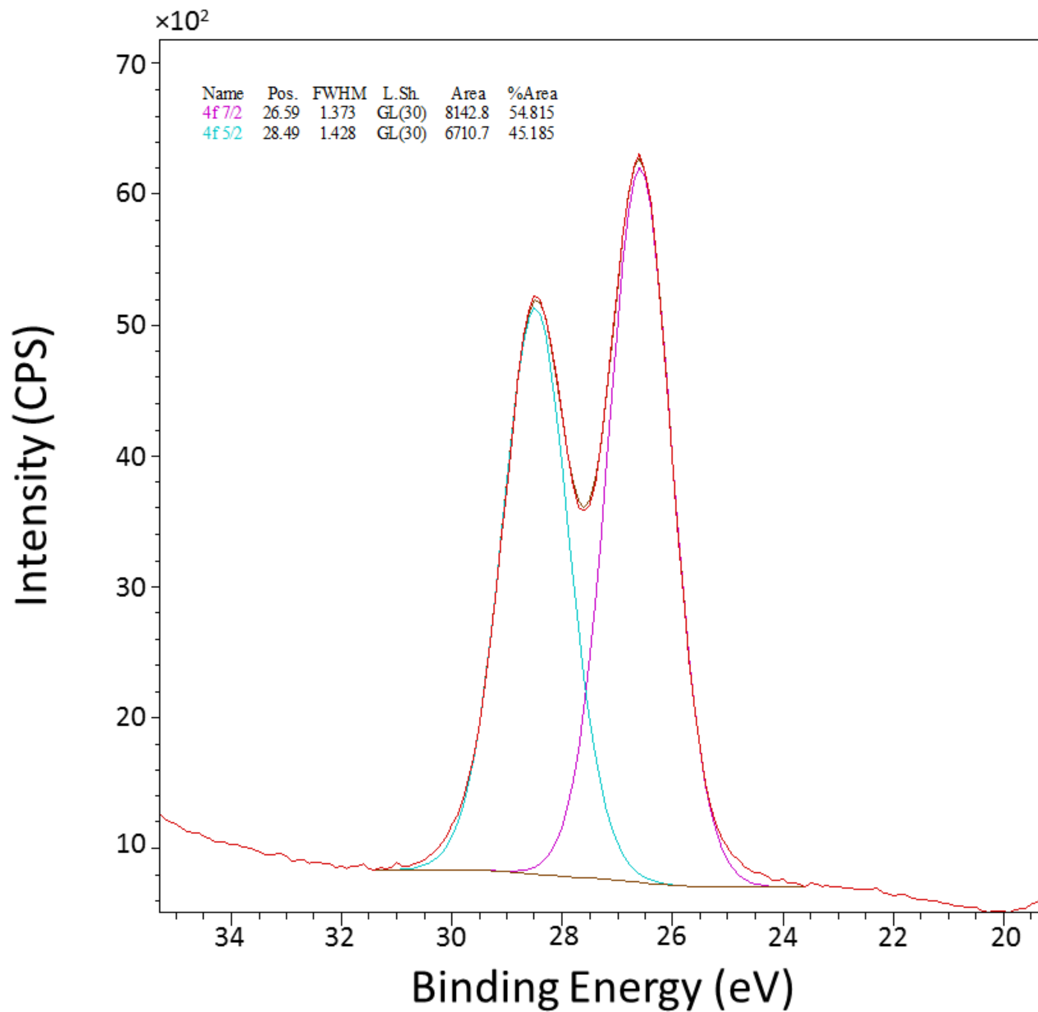

Figure A.3 XPS curves for Ta 4f from the unannealed samples. Note the peak location of 25.85 is consistent with the peak location from literature (26-27 ev).

REFERENCES

[1] "International Energy Outlook 2011," U.S. Energy Information Administration, DOE/EIA-0484(2011), 2011.

[2] "Annual Energy Review 2011," U.S. Energy Information Administration, DOE/EIA-0384(2011), 2011.

[3] Laroche, M., Carminati, R., and Greffet, J.-J., 2006, "Near-Field Thermophotovoltaic Energy Conversion," J. Appl. Phys., **100**, p. 063704.

[4] Hu, L., Narayanaswamy, A., Chen, X., and Chen, G., 2008, "Near-Field Thermal Radiation Between Two Closely Spaced Glass Plates Exceeding Planck's Blackbody Radiation Law," Appl. Phys. Lett., **92**, p. 133106.

[5] Fadel, M., Azim M., O. A., Omer, O. A., and Basily, R. R., 1998, "A Study of Some Optical Properties of Hafnium Dioxide (HfO_2) Thin Films and Their Applications," Appl. Phys. A Mater. Sci. Process., **66**, pp. 335–343.

[6] Waldorf, A. J., Dobrowolski, J. A., Sullivan, B. T., and Plante, L. M., 1993, "Optical Coatings Deposited by Reactive Ion Plating," Appl. Opt., **32**, pp. 5583–5593.

[7] Pervak, V., Krausz, F., and Apolonski, A., 2007, "Hafnium Oxide Thin Films Deposited by Reactive Middle-Frequency Dual-Magnetron Sputtering," Thin Solid Films, **515**, pp. 7984–7989.

[8] Torchio, P., Gatto, A., Alvisi, M., Albrand, G., Kaiser, N., and Amra, C., 2002, "High-Reflectivity HfO_2/SiO_2 Ultraviolet Mirrors," Appl. Opt., **41**, pp. 3256–61.

[9] Al-Kuhaili, M. F., 2004, "Optical Properties of Hafnium Oxide Thin Films and Their Application in Energy-Efficient Windows," Opt. Mater., **27**, pp. 383–387.

[10] Cho, S. D. and Paik, K. W., 1999, "Study on the Amorphous Ta2O5 Thin Film Capacitors Deposited by DC Magnetron Reactive Sputtering for Multichip Module Applications," Mater. Sci. Eng. B Solid-State Mater. Adv. Technol., **67**, pp. 108–112.

[11] Chaneliere, C., Autran, J. L., Devine, R. A. B., and Balland, B., 1998, "Tantalum Pentoxide (Ta_2O_5) Thin Films for Advanced Dielectric Applications," Mater. Sci. Eng. R Reports, **22**, pp. 269–322.

[12] Rubio, F., Denis, J., Albella, J. M., and Martinez-Duart, J. M., 1982, "Sputtered Ta_2O_5 Antireflection Coatings for Silicon Solar Cells," Thin Solid Films, **90**, pp. 405–408.

[13] Toki, K., Kusakabe, K., Odani, T., Kobuna, S., and Shimizu, Y., 1996, "Deposition of SiO_2 and Ta_2O_5 Films by Electron-Beam-Excited Plasma Ion Plating," Thin Solid Films, **281**–**282**, pp. 401–403.

[14] Franke, E. B., Trimble, C. L., Schubert, M., Woollam, J. A., and Hale, J. S., 2000, "All-Solid-State Electrochromic Reflectance Device for Emittance Modulation in the Far-Infrared Spectral Region," Appl. Phys. Lett., **77**, pp. 930–932.

[15] Curtis, C., 2006, "Some Properties of Hafnium Oxide, Hafnium Silicate, Calcium Hafnate, and Hafnium Carbide," J. Am. Ceram. Soc., **37**, pp. 458–465.

[16] Matsumoto, K., Itoh, Y., and Kameda, T., 2003, "EB-PVD Process and Thermal Properties of Hafnia-Based Thermal Barrier Coating," Sci. Technol. Adv. Mater., **4**, pp. 153–158.

[17] Singh, J., Wolfe, D. E., Miller, R. A., Eldridge, J. I., and Zhu, D.-M., 2004, "Tailored Microstructure of Zirconia and Hafnia-Based Thermal Barrier Coatings with Low Thermal Conductivity and High Hemispherical Reflectance by EB-PVD," J. Mater. Sci., **39**, pp. 1975–1985.

[18] Lehan, J., Mao, Y., Bovard, B., and Macleod, H., 1991, "Optical and Microstructural Properties of Hafnium Dioxide Thin Films," Thin Solid Films, **203**, pp. 227–250.

[19] Edlou, S. M., Smajkiewicz, A., and Al-Jumaily, G. A., 1993, "Optical Properties and Environmental Stability of Oxide Coatings Deposited by Reactive Sputtering," Appl. Opt., **32**, p. 5601.

[20] Sancho-Parramon, J., Modreanu, M., Bosch, S., and Stchakovsky, M., 2008, "Optical Characterization of HfO2 by Spectroscopic Ellipsometry: Dispersion Models and Direct Data Inversion," Thin Solid Films, **516**, pp. 7990–7995.

[21] Liu, X. and Li, D., 2006, "Influence of Charged Particle Bombardment and Sputtering Parameters on the Properties of HfO_2 Films Prepared by DC Reactive Magnetron Sputtering," Appl. Surf. Sci., **253**, pp. 2143–2147.

[22] Aygun, G., Cantas, A., Simsek, Y., and Turan, R., 2010, "Effects of Physical Growth Conditions on the Structural and Optical Properties of Sputtered Grown Thin HfO_2 Films," Thin Solid Films, **519**, pp. 5820–5825.

[23] Toledano-Luque, M., San Andrés, E., del Prado, A., Mártil, I., Lucía, M. L., González-Díaz, G., Martínez, F. L., Bohne, W., Röhrich, J., and Strub, E., 2007, "High-Pressure Reactively Sputtered HfO_2: Composition, Morphology, and Optical Properties," J. Appl. Phys., **102**, p. 044106.

[24] Tang, W. T., Ying, Z. F., Hu, Z. G., Li, W. W., Sun, J., Xu, N., and Wu, J. D., 2010, "Synthesis and Characterization of HfO_2 and ZrO_2 Thin Films Deposited by Plasma Assisted Reactive Pulsed Laser Deposition at Low Temperature," Thin Solid Films, **518**, pp. 5442–5446.

[25] Balog, M., Schieber, M., Michman, M., and Patai, S., 1977, "Chemical Vapor Deposition and Characterization of HfO_2 Films from Organo-Hafnium Compounds," Thin Solid Films, **41**, pp. 247–259.

[26] Chen, S. C., Lou, J. C., Chien, C. H., Liu, P. T., and Chang, T. C., 2005, "An Interfacial Investigation of High-Dielectric Constant Material Hafnium Oxide on Si Substrate," Thin Solid Films, **488**, pp. 167–172.

[27] Aarik, J., Aidla, A., Kiisler, A., Uustare, T., and Sammelselg, V., 1999, "Influence of Substrate Temperature on Atomic Layer Growth and Properties of HfO_2 Thin Films," Thin Solid Films, **340**, pp. 110–116.

[28] Puthenkovilakam, R., Lin, Y.-S., Choi, J., Lu, J., Blom, H.-O., Pianetta, P., Devine, D., Sendler, M., and Chang, J. P., 2005, "Effects of Post–deposition Annealing on the Material Characteristics of Ultrathin HfO_2 Films on Silicon," J. Appl. Phys., **97**, p. 023704.

[29] Hackley, J. C. and Gougousi, T., 2009, "Properties of Atomic Layer Deposited HfO_2 Thin Films," Thin Solid Films, **517**, pp. 6576–6583.

[30] Neumayer, D. A. and Cartier, E., 2001, "Materials Characterization of ZrO_2–SiO_2 and HfO_2–SiO_2 Binary Oxides Deposited by Chemical Solution Deposition," J. Appl. Phys., **90**, p. 1801.

[31] Lopez, C. M. and Irene, E. A., 2006, "A Study of HfO Film Interfaces with Si and SiO," J. Appl. Phys., **99**, p. 024101.

[32] Jerman, M., Qiao, Z., and Mergel, D., 2005, "Refractive Index of Thin Films of SiO_2, ZrO_2, and HfO_2 as a Function of the Films' Mass Density," Appl. Opt., **44**, pp. 3006–3012.

[33] Rammula, R., Aarik, J., Mändar, H., Ritslaid, P., and Sammelselg, V., 2010, "Atomic Layer Deposition of HfO_2: Effect of Structure Development on Growth Rate, Morphology and Optical Properties of Thin Films," Appl. Surf. Sci., **257**, pp. 1043–1052.

[34] Traylor Kruschwitz, J. D. and Pawlewicz, W. T., 1997, “Optical and Durability Properties of Infrared Transmitting Thin Films.,” Appl. Opt., **36**, pp. 2157–2159.

[35] Modreanu, M., Sancho-Parramon, J., Durand, O., Servet, B., Stchakovsky, M., Eypert, C., Naudin, C., Knowles, A., Bridou, F., and Ravet, M.-F., 2006, “Investigation of Thermal Annealing Effects on Microstructural and Optical Properties of HfO_2 Thin Films,” Appl. Surf. Sci., **253**, pp. 328–334.

[36] Jayaraman, A., Wang, S. Y., Sharma, S. K., and Ming, L. C., 1993, “Pressure-Induced Phase Transformations in HfO_2 to 50 GPa Studied by Raman Spectroscopy,” Phys. Rev. B, **48**, pp. 9205–9211.

[37] Zhao, X. and Vanderbilt, D., 2002, “First-Principles Study of Structural, Vibrational, and Lattice Dielectric Properties of Hafnium Oxide,” Phys. Rev. B, **65**, pp. 13–16.

[38] Rignanese, G.-M., Gonze, X., Jun, G., Cho, K., and Pasquarello, A., 2004, “First-Principles Investigation of High-κ Dielectrics: Comparison Between the Silicates and Oxides of Hafnium and Zirconium,” Phys. Rev. B, **69**, pp. 1–10.

[39] González, J., Ruiz, M. C., Rivarola, J. B., and Pasquevich, D., 1998, “Effects of Heating in Air and Chlorine Atmosphere on the Crystalline Structure of Pure Ta_2O_5 or Mixed with Carbon,” J. Mater. Sci., **3**, pp. 4173–4180.

[40] Chaneliere, C., Four, S., Autran, J. L., and Devine, R. A. B., 1999, “Comparison Between the Properties of Amorphous and Crystalline Ta_2O_5 Thin Films Deposited on Si,” Microelectron. Reliab., **39**, pp. 261–268.

[41] Khawaja, E. and Tomlin, S., 1975, “The Optical Properties of Thin Films of Tantalum Pentoxide and Zirconium Dioxide,” Thin Solid Films, **30**, pp. 361–369.

[42] Rubio, F., Albella, J., Denis, J., and Martinez-Duart, J., 1982, “Optical Properties of Reactively Sputtered Ta_2O_5 Films,” J. Vac. Sci. Technol. A Vacuum, Surfaces, Film., **21**, pp. 1043–1045.

[43] Al-Jumaily, G. A. and Edlou, S. M., 1992, “Optical Properties of Tantalum Pentoxide Coatings Deposited Using Ion Beam Processes,” Thin Solid Films, **209**, pp. 223–229.

[44] Atanassova, E., Aygun, G., Turan, R., and Babeva, T., 2006, “Structural and Optical Characteristics of Tantalum Oxide Grown by Pulsed Nd:YAG Laser Oxidation,” J. Vac. Sci. Technol. A Vacuum, Surfaces, Film., **24**, pp. 206–211.

[45] Zhou, J., Luo, D., Li, Y., and Liu, Z., 2009, “Properties of Ta_2O_5 Thin Films Deposited by DC Reactive Magnetron Sputtering,” Int. J. Mod. Phys. B, **23**, pp. 5275–5282.

[46] Chandrasekharan, R., Prakash, S., Shannon, M. A., and Masel, R. I., 2007, "Change in Radiative Optical Properties of Ta_2O_5 Thin Films Due to High-Temperature Heat Treatment," J. Heat Transfer, **129**, pp. 27–36.

[47] Franke, E., Trimble, C. L., DeVries, M. J., Woollam, J. A., Schubert, M., and Frost, F., 2000, "Dielectric Function of Amorphous Tantalum Oxide from the Far Infrared to the Deep Ultraviolet Spectral Region Measured by Spectroscopic Ellipsometry," J. Appl. Phys., **88**, pp. 5166–5174.

[48] Franke, E., Schubert, M., Trimble, C. L., DeVries, M. J., and Woollam, J. A., 2001, "Optical Properties of Amorphous and Polycrystalline Tantalum Oxide Thin Films Measured by Spectroscopic Ellipsometry from 0.03 to 8.5 eV," Thin Solid Films, **388**, pp. 283–289.

[49] Ono, H., Hosokawa, Y., and Shinoda, K., 2001, "Ta–O Phonon Peaks in Tantalum Oxide Films on Si," Thin Solid Films, **381**, pp. 57–61.

[50] Basu, S., Chen, Y. B., and Zhang, Z. M., 2007, "Microscale Radiation in Thermophotovoltaic devices—A Review," Int. J. Energy Res., **31**, pp. 689–716.

[51] Basu, S., Zhang, Z. M., and Fu, C. J., 2009, "Review of Near-Field Thermal Radiation and Its Application to Energy Conversion," Int. J. Energy Res., **33**, pp. 1203–1232.

[52] Pan, J. L., Choy, H. K. H., and Fonstad, C. G., 2000, "Very Large Radiative Transfer over Small Distances from a Black Body for Thermophotovoltaic Applications," IEEE Trans. Electron Devices, **47**, pp. 241–249.

[53] Narayanaswamy, A. and Chen, G., 2003, "Surface Modes for Near Field Thermophotovoltaics," Appl. Phys. Lett., **82**, pp. 3544–3546.

[54] Whale, M. D. and Cravalho, E. G., 2002, "Modeling and Performance of Microscale Thermophotovoltaic Energy Conversion Devices," IEEE Trans. Energy Convers., **17**, pp. 130–142.

[55] Park, K., Basu, S., King, W. P., and Zhang, Z. M., 2008, "Performance Analysis of Near-Field Thermophotovoltaic Devices Considering Absorption Distribution," J. Quant. Spectrosc. Radiat. Transf., **109**, pp. 305–316.

[56] Francoeur, M., Vaillon, R., and Mengüç, M. P., 2011, "Thermal Impacts on the Performance of Nanoscale-Gap Thermophotovoltaic Power Generators," IEEE Trans. Energy Convers., **26**, pp. 686–698.

[57] Ottens, R. S., Quetschke, V., Wise, S., Alemi, A. A., Lundock, R., Mueller, G., Reitze, D. H., Tanner, D. B., and Whiting, B. F., 2011, "Near-Field Radiative Heat Transfer Between Macroscopic Planar Surfaces," Phys. Rev. Lett., **107**, pp. 1–4.

[58] Hanamura, K., Fukai, H., Srinivasan, E., Asano, M., and Masuhara, T., "Photovoltaic Generation of Electricity Using Near-Field Radiation," in *Proc. ASME/JSME 2011 8th Therm. Eng. Jt. Conf.*, 2011, **1**, pp. 1–5.

[59] DiMatteo, R. S., Greiff, P., Finberg, S. L., Young-Waithe, K. a., Choy, H. K. H., Masaki, M. M., and Fonstad, C. G., 2001, "Enhanced Photogeneration of Carriers in a Semiconductor via Coupling Across a Nonisothermal Nanoscale Vacuum Gap," Appl. Phys. Lett., **79**, pp. 1894–1896.

[60] Whale, M., 2001, "The Influence of Interference and Heterojunctions on the Performance of Microscale Thermophotovoltaic Devices," Microscale Thermophys. Eng., **5**, pp. 37–41.

[61] Fraas, L. M. and Partain, L. D., *Solar Cells and Their Applications*. Wiley, 2010.

[62] Schilling, J., 2006, "Uniaxial Metallo-Dielectric Metamaterials with Scalar Positive Permeability," Phys. Rev. E, **74**, p. 046618.

[63] Noginov, M. A., Barnakov, Y. A., Zhu, G., Tumkur, T., and Li, H., 2009, "Bulk Photonic Metamaterial with Hyperbolic Dispersion," Appl. Phys. Lett., **94**, p. 151105.

[64] Tserkezis, C., Stefanou, N., and Papanikolaou, N., 2010, "Extraordinary Refractive Properties of Photonic Crystals of Metallic Nanorods," J. Opt. Soc. Am. B, **27**, pp. 2620–2626.

[65] Yao, J., Liu, Z., Liu, Y., Wang, Y., Sun, C., Bartal, G., Stacy, A. M., and Zhang, X., 2008, "Optical Negative Refraction in Bulk Metamaterials of Nanowires," Science, **321**, p. 930.

[66] Orlov, A., Iorsh, I., Belov, P., and Kivshar, Y., 2013, "Complex Band Structure of Nanostructured Metal-Dielectric Metamaterials," **21**, pp. 1593–1598.

[67] Ramakrishna, S. A., Pendry, J. B., Wiltshire, M. C. K., and Steward, W. J., 2003, "Imaging the Near Field," J. Mod. Opt., **50**, pp. 37–41.

[68] Belov, P. A. and Hao, Y., 2006, "Subwavelength Imaging at Optical Frequencies Using a Transmission Device Formed by a Periodic Layered Metal-Dielectric Structure Operating in the Canalization Regime," Phys. Rev. B, **73**, p. 113110.

[69] Guo, Y. and Jacob, Z., 2013, "Thermal Hyperbolic Metamaterials," Opt. Express, **21**, pp. 15014–15019.

[70] Guo, Y., Cortes, C. L., Molesky, S., and Jacob, Z., 2012, "Broadband Super-Planckian Thermal Emission from Hyperbolic Metamaterials," Appl. Phys. Lett., **101**, p. 131106.

[71] Biehs, S.-A., Ben-Abdallah, P., Rosa, F. S. S., Joulain, K., and Greffet, J.-J., 2011, "Nanoscale Heat Flux Between Anisotropic Uniaxial Media," arXiv:1103.2361, pp. 1–10.

[72] Biehs, S.-A., Ben-Abdallah, P., Rosa, F. S. S., Joulain, K., and Greffet, J.-J., 2011, "Nanoscale Heat Flux Between Nanoporous Materials," Opt. Express, **19**, pp. A1088–103.

[73] Chapman, D. M. F., 2008, "Using Streamlines to Visualize Acoustic Energy Flow Across Boundaries.," J. Acoust. Soc. Am., **124**, pp. 48–56.

[74] Zhang, Z. M. and Lee, B. J., 2006, "Lateral Shift in Photon Tunneling Studied by the Energy Streamline Method," Opt. Express, **14**, pp. 9963–9970.

[75] Basu, S., Wang, L. P., and Zhang, Z. M., 2011, "Direct Calculation of Energy Streamlines in Near-Field Thermal Radiation," J. Quant. Spectrosc. Radiat. Transf., **112**, pp. 1149–1155.

[76] Lee, B. J. and Zhang, Z. M., 2008, "Lateral Shifts in Near-Field Thermal Radiation with Surface Phonon Polaritons," Nanoscale Microscale Thermophys. Eng., **12**, pp. 238–250.

[77] Griffiths, D. J., *Introduction to Electrodynamics*. Pearson Education, Limited, 2012.

[78] Zhang, Z. M., *Nano/Microscale Heat Transfer*. New York: McGraw-Hill Professional, 2007.

[79] Poelman, D. and Smet, P. F., 2003, "Methods for the Determination of the Optical Constants of Thin Films from Single Transmission Measurements: a Critical Review," J. Phys. D. Appl. Phys., **36**, pp. 1850–1857.

[80] Aspnes, D. E., 1982, "Local-Field Effects and Effective-Medium Theory: A Microscopic Perspective," Am. J. Phys., **50**, pp. 704–709.

[81] Pendry, J. B., 2000, "Negative Refraction Makes a Perfect Lens," Phys. Rev. Lett., **85**, pp. 3966–3969.

[82] Tschikin, M., Biehs, S.-A., Messina, R., and Ben-Abdallah, P., 2013, "On the Limits of the Effective Description of Hyperbolic Materials in the Presence of Surface Waves," J. Opt., **15**, p. 105101.

[83] Kidwai, O., Zhukovsky, S. V., and Sipe, J. E., 2012, "Effective-Medium Approach to Planar Multilayer Hyperbolic Metamaterials: Strengths and Limitations," Phys. Rev. A, **85**, p. 053842.

[84] Francoeur, M. and Mengüç, M. P., 2008, "Role of Fluctuational Electrodynamics in Near-Field Radiative Heat Transfer," J. Quant. Spectrosc. Radiat. Transf., **26**, pp. 686–698.

[85] Rytov, S. M., Kravtsov, Y. A., Kravt͡sov, I. U. A., and Tatarskii, V. I., *Principles of Statistical Radiophysics: Correlation Theory of Random Processes*. Springer, 1988.

[86] Sipe, J. E., 1987, "New Green-Function Formalism for Surface Optics," J. Opt. Soc. Am. B, **4**, pp. 481–489.

[87] Francoeur, M., Pinar Mengüç, M., and Vaillon, R., 2009, "Solution of Near-Field Thermal Radiation in One-Dimensional Layered Media Using Dyadic Green's Functions and the Scattering Matrix Method," J. Quant. Spectrosc. Radiat. Transf., **110**, pp. 2002–2018.

[88] Zhang, Z. M., Fu, C. J., and Zhu, Q. Z., 2003, "Optical and Thermal Radiative Properties of Semiconductors Related to Micro/nanotechnology," Adv. Heat Transf., **37**, pp. 179–296.

[89] Lee, B. J., Zhang, Z. M., Early, E. A., DeWitt, D. P., and Tsai, B. K., 2005, "Modeling Radiative Properties of Silicon with Coatings and Comparison with Reflectance Measurements," J. Thermophys. heat Transf., **19**, pp. 558–565.

[90] Palik, E. D., *Handbook of Optical Constants of Solids*. San Diego: Academic Press, 1998.

[91] Basu, S., Lee, B. J., and Zhang, Z. M., 2010, "Infrared Radiative Properties of Heavily Doped Silicon at Room Temperature," J. Heat Transfer, **132**, p. 023301.

[92] Wang, L. P., Lee, B. J., Wang, X. J., and Zhang, Z. M., 2009, "Spatial and Temporal Coherence of Thermal Radiation in Asymmetric Fabry–Perot Resonance Cavities," Int. J. Heat Mass Transf., **52**, pp. 3024–3031.

[93] Lee, B. J., Khuu, V. P., and Zhang, Z. M., 2005, "Partially Coherent Spectral Transmittance of Dielectric Thin Films with Rough Surfaces," J. Thermophys. Heat Transf., **19**, pp. 360–366.

[94] Fu, C. J. and Zhang, Z. M., 2006, "Nanoscale Radiation Heat Transfer for Silicon at Different Doping Levels," Int. J. Heat Mass Transf., **49**, pp. 1703–1718.

[95] Bright, T. J., Watjen, J. I., Zhang, Z. M., Muratore, C., and Voevodin, A. A., 2012, "Optical Properties of HfO_2 Thin Films Deposited by Magnetron Sputtering: From the Visible to the Far-Infrared," Thin Solid Films, **520**, pp. 6793–6802.

[96] "Powder Diffraction File," Internation Centre for Diffraction Data, PDF-4+, Newton Square, PA, 2011.

[97] Kumar, A. R., Zhang, Z. M., Boychev, V. A., Tanner, D. B., Vale, L. R., and Rudman, D. A., 1999, "Far-Infrared Transmittance and Reflectance of $YBa_2Cu_3O_{7-\delta}$ Films on Si Substrates," J. Heat Transfer, **121**, pp. 844–851.

[98] Swanepoel, R., 1983, "Determination of Thickness and Optical Constants of Amorphous Silicon," J. Phys. E., **16**, pp. 1214–1222.

[99] Zhang, Z. M., Choi, B. I., and Flik, M. I., 1994, "Infrared Refractive Indices of $LaAlO_3$, $LaGaO_3$, and $NdGaO_3$," J. Opt. Soc. Am. B, **11**, pp. 2252–2257.

[100] Press, W. H., *Numerical Recipes: The Art of Scientific Computing*. Cambridge University Press, 2007.

[101] Bohren, C. F. and Huffman, D. R., *Absorption and Scattering of Light by Small Particle*. New York: , 1983.

[102] Palmer, K. F. and Williams, D., 1974, "Optical Properties of Water in the Near Infrared," J. Opt. Soc. Am., **64**, pp. 1107–1110.

[103] Downing, H. D. and Williams, D., 1975, "Optical Constants of Water in the Infrared," J. Geophys. Res., **80**, pp. 1656–1661.

[104] Tompkins, H. G. and McGahan, W. A., *Spectroscopic Ellipsometry and Reflectometry: a User's Guide*. Wiley, 1999.

[105] Jellison Jr., G. E., 1991, "Use of the Biased Estimator in the Interpretation of Spectroscopic Ellipsometry Data," Appl. Opt., **30**, pp. 3354–3360.

[106] Koh, J., Lu, Y., Wronski, C. R., Kuang, Y., Collins, R. W., Tsong, T. T., and Strausser, Y. E., 1996, "Correlation of Real Time Spectroellipsometry and Atomic Force Microscopy Measurements of Surface Roughness on Amorphous Semiconductor Thin Films," Appl. Phys. Lett., **69**, pp. 1297–1299.

[107] Wilk, G. D., Wallace, R. M., and Anthony, J. M., 2001, "High-κ Gate Dielectrics: Current Status and Materials Properties Considerations," J. Appl. Phys., **89**, pp. 5243–5275.

[108] Vol'pyan, O. D. and Yakovlev, P. P., 2002, "The Effect of Heat Treatment on the Optical Properties of Ta_2O_5 Films," J. Opt. Technol., **69**, pp. 29–31.

[109] Atanassova, E., Dimitrova, T., and Koprinarova, J., 1995, "AES and XPS Study of Thin RF-Sputtered Ta_2O_5 Layers," Appl. Surf. Sci., **84**, pp. 193–202.

[110] Jagadeesh Chandra, S. V, Uthanna, S., and Mohan Rao, G., 2008, "Effect of Substrate Temperature on the Structural, Optical and Electrical Properties of DC Magnetron Sputtered Tantalum Oxide Films," Appl. Surf. Sci., **254**, pp. 1953–1960.

[111] Chen, K., Nielsen, M., Yang, G. R., Rymaszewski, E. J., and Lu, T.-M., 1997, "Study of Amorphous Ta_2O_5 Thin Films by DC Magnetron Reactive Sputtering," J. Electron. Mater., **26**, pp. 397–401.

[112] Guoping, C., Lingzhen, L., Suixin, Z., and Haokang, Z., 1990, "Structures and Properties of a Ta_2O_5 Thin Film Deposited by DC Magnetron Reactive Sputtering in a Pure O_2 Atmosphere," Vacuum, **41**, pp. 1204–1206.

[113] Ngaruiya, J. M., Venkataraj, S., Drese, R., Kappertz, O., Leervad Pedersen, T. P., and Wuttig, M., 2003, "Preparation and Characterization of Tantalum Oxide Films Produced by Reactive DC Magnetron Sputtering," Phys. Status Solidi A Appl. Mater. Sci., **198**, pp. 99–110.

[114] Joshi, P. C. and Cole, M. W., 1999, "Influence of Postdeposition Annealing on the Enhanced Structural and Electrical Properties of Amorphous and Crystalline Ta_2O_5 Thin Films for Dynamic Random Access Memory Applications," J. Appl. Phys., **86**, p. 871.

[115] Dimitrova, T., Arshak, K., and Atanassova, E., 2001, "Crystallization Effects in Oxygen Annealed Ta_2O_5 Thin Films on Si," Thin Solid Films, **381**, pp. 31–38.

[116] Patterson, A. L., 1939, "The Scherrer Formula for X-Ray Particle Size Determination," Phys. Rev., **56**, pp. 978–982.

[117] Yoon, S. G., Kim, Y. T., Kim, H. K., Kim, M. J., Lee, H. M., and Yoon, D. H., 2005, "Comparision of Residual Stress and Optical Properties in Ta_2O_5 Thin Films Deposited by Single and Dual Ion Beam Sputtering," Mater. Sci. Eng. B, **118**, pp. 234–237.

[118] Clauws, P., Broeckx, J., and Vennik, J., 1985, "Lattice Vibrations of V2O5. Calculation of Normal Vibrations in a Urey-Bradley Force Field," Phys. Status Solidi, **459**.

[119] Carr, G. L., Perkowitz, S., and Tanner, D. B., "Far-Infrared Properties of Inhomogenous Materials," in *Infrared and Millimeter Waves*, Button, W. J., Ed. Orlando: Academic Press, 1985, pp. 171–263.

[120] Siegel, R. and Howell, J. R., *Thermal Radiation Heat Transfer*, 4th ed. New York: Taylor & Francis, 2002.

[121] Zhu, Q. Z. and Zhang, Z. M., "Radiative Properties of Micro/Nanoscale Particles in Dispersions for Photothermal Energy Conversion," in *Nanoparticle Heat Transfer and Fluid Flow*, Minkowycz, W. J., Sparrow, E. M., and Abrahamn, J., Eds. CRC Press/Taylor & Francis Group, 2012, pp. 143–174.

[122] Kulisch, W., Gilliland, D., Ceccone, G., Sirghi, L., Rauscher, H., Gibson, P. N., Zürn, M., Bretagnol, F., and Rossi, F., 2009, "Ion Beam Sputtering of Ta_2O_5 Films on Thermoplast Substrates as Waveguides for Biosensors," J. Vac. Sci. Technol. B Microelectron. Nanom. Struct., **27**, pp. 1180–1190.

[123] Basu, S. and Zhang, Z. M., 2009, "Ultrasmall Penetration Depth in Nanoscale Thermal Radiation," Appl. Phys. Lett., **95**, p. 133104.

[124] Gozalez-Cuevas, J. A., Refaat, T. F., Abedin, M. N., and Elsayed-Ali, H. E., 2006, "Modeling of the Temperature-Dependent Spectral Response of $In_{(1-x)}Ga_{(x)}Sb$ Infrared Photodetectors," Opt. Eng., **45**, p. 044001.

[125] Luque, A. and Hegedus, S., *Handbook of Photovoltaic Science and Engineering*. Wiley, 2011.

[126] Sze, S. M. and Ng, K. K., *Physics of Semiconductor Devices*. Wiley, 2006.

[127] Fu, C. J. and Tan, W. C., 2009, "Near-Field Radiative Heat Transfer Between Two Plane Surfaces with One Having a Dielectric Coating," J. Quant. Spectrosc. Radiat. Transf., **110**, pp. 1027–1036.

[128] Eroglu, A., Lee, Y. H., and Lee, J. K., 2011, "Dyadic Green's Functions for Multi-Layered Uniaxially Anisotropic Media with Arbitrarily Oriented Optic Axes," IET Microwaves, Antennas Propag., **5**, pp. 1779–1788.

[129] Lee, J. and Kong, J., 1983, "Dyadic Green's Functions for Layered Anisotropic Medium," Electromagnetics, **02139**, pp. 111–130.

[130] Godin, O. A., 2009, "Wave Refraction at an Interface: Snell's Law Versus Chapman's Law," J. Acoust. Soc. Am., **125**, pp. EL117–EL122.

[131] Scalora, M., D'Aguanno, G., Mattiucci, N., Bloemer, M. J., de Ceglia, D., Centini, M., Mandatori, A., Sibilia, C., Akozbek, N., Cappeddu, M. G., Fowler, M., and Haus, J. W., 2007, "Negative Refraction and Sub-Wavelength Focusing in the Visible Range Using Transparent Metallo-Dielectric Stacks," Opt. Express, **15**, pp. 508–523.

[132] De Ceglia, D., Vincenti, M., Cappeddu, M., Centini, M., Akozbek, N., D'Orazio, a., Haus, J., Bloemer, M., and Scalora, M., 2008, "Tailoring Metallodielectric Structures for Superresolution and Superguiding Applications in the Visible and Near-Ir Ranges," Phys. Rev. A, **77**, p. 033848.

[133] "NIST X-Ray Photoelectron Spectroscopy Database, Version 4.1 (National Institute of Standards and Technology, Gaithersburg, 2012); Http://srdata.nist.gov/xps/."